Study of Functional Carbon Materials for Energy Applications

Zhong, Shan

(Degree)
博士（工学）

(Date of Degree)
2020-03-25

(Date of Publication)
2022-03-25

(Resource Type)
doctoral thesis

(Report Number)
甲第7775号

(URL)
https://hdl.handle.net/20.500.14094/D1007775

博 士 論 文

Study of Functional Carbon Materials for Energy Applications

機能性炭素材料の合成とエネルギー応用に関する研究

January, 2020

Graduate School of Engineering

Kobe University

ZHONG SHAN

（鐘 珊）

Acknowledgements

This dissertation is dedicated to those people who have ever supported and helped me.

The research work depicted in the current doctoral dissertation has been carried out in the Cooperative Division (located at Kansai Center, National Institute of Advanced Industrial Science and Technology (AIST)), Department of Chemical Science and Engineering, Graduate School of Engineering, Kobe University in a period of October, 2016 ~ March, 2020.

I would like to represent my deepest thanks to Professor Qiang Xu for his meaningful suggestions, strong guidance, precious discussions, and friendly consideration, as well as his careful checking and reading of this dissertation.

I greatly appreciate Professor Minoru Mizuhata, Professor Satoru Nishiyama, Professor Masaki Matsui, and Professor Tsutomu Ioroi for their helpful advice and critical review of this dissertation.

I am grateful to Ms. Naoko Yamawaki, Ms. Hitomi Fuji, and other members in our group for the kind helps and suggestions.

I sincerely thank for financial supports from MEXT, AIST, and Kobe University.

At last, I truly appreciate my families for the emotional supports and constant encouragements, which allow me keep moving on.

ZHONG SHAN

（鐘 珊）

January, 2020

Osaka, Japan

Abstract

As the fast development of global economy and industry, it is imperative to develop high performance and environmentally friendly devices to satisfy the demand for energy of human beings. In this doctor dissertation, we concern on the syntheses of functional carbon-based materials and their energy-related applications, including the electrode materials for supercapacitors and potential supports for metal nanoparticles (NPs) as heterogenous catalysts. In the introduction, we mainly described the merits of functional carbon materials used as 1) electrodes for electrochemical energy storage and 2) supports for NPs for hydrogen evolution from liquid chemical hydrides. We also introduced the concerning research progresses. In the first work, the hierarchically porous carbons with high ratios of meso-/macropore volume to micropore volume and high surface areas derived from metal-organic framework (MOF)/chitosan composites were prepared, displaying excellent capacitive behaviors. In our second work, boron-oxygen-functionalized carbon nanospheres successfully immobilized palladium (Pd) NPs towards efficient hydrogen generation from formic acid. In the third work, active Pd NPs immobilized on Fe_3C/Fe- and N-functionalized porous carbon were synthesized for fast hydrogen generation from formic acid. The related outcomes of this dissertation are concluded below.

(i) Hierarchically Porous Carbons Derived from Metal-Organic Framework/Chitosan Composites for High-Performance Supercapacitors

We present the synthesis of hierarchically porous carbons through the calcination of MOF/chitosan composites. The effects of chitosan (CS) addictive on the pore structures of resultant carbons were discussed. The MOF/chitosan precursors could be converted

into hierarchically porous carbons (NPC-*V*, *V* = 1, 2, 4, and 6) with much higher ratios of meso-/macropore volume to micropore volume ($V_{meso\text{-}macro}/V_{micro}$). The derived carbon NPC-2 with the high ratio of $V_{meso\text{-}macro}/V_{micro}$ = 1.47 demonstrates a high specific surface area of 2375 $m^2\ g^{-1}$, and a high pore volume of 2.49 $cm^3\ g^{-1}$, as well as a high graphitization degree, comparison with its counterpart (NPC) without chitosan addition. These excellent features are favorable of rapid ion diffusion/transport, endowing NPC-2 with enhanced electrochemical behaviors as supercapacitor electrodes, corresponding to a high specific capacitance of 199.9 F g^{-1} and good rate capability. The good cycling stability is also observed after 10 000 cycles.

(ii) Immobilizing Palladium Nanoparticles on Boron-Oxygen-Functionalized Carbon Nanospheres towards Efficient Hydrogen Generation from Formic Acid

Carbon nanospheres (XC-72R) were functionalized by boron-oxygen (B-O) through coannealing with boric acid, to which highly dispersed Pd NPs (~ 1.7 nm) were immobilized by a wet chemical reduction for the first time. The Pd/OB-C catalyst exhibits significantly improved activity for the dehydrogenation from FA, compared to pristine XC-72R supported Pd NPs (Pd/C). Impressively, by adding melamine precursor, the B-O and nitrogen (N)-functionalized product OB-C-N displays an extremely high B content, ca. 34 times higher than OB-C. The Pd/OB-C-N catalyst with an ultrafine Pd particle size of ~ 1.4 nm shows a superb activity, with a turnover frequency (TOF) as high as 5354 h^{-1} at 323 K, owing to the uniform ultrafine Pd NPs and the effect from B-O and N functionalities.

(iii) Immobilizing Ultrafine Palladium Nanoparticles on Fe_3C/Fe- and N-functionalized Porous Carbon towards Fast Hydrogen Generation from Formic Acid

A Fe_3C/Fe- and N-functionalized porous carbon with a micro-/mesoporous porosity was synthesized. This distinct carbon (Fe_3C-Fe@NC) was used as a support to immobilize palladium nanoparticles (Pd NPs) (~ 1.4 nm) using a wet chemical reduction method. The Pd/Fe_3C-Fe@NC catalyst exhibits a superb activity for formic acid (FA) dehydrogenation, providing a rather high turnover frequency (TOF) of 7361 h^{-1} at 323 K, attributed to the ultrafine Pd NPs and the effects from Fe_3C/Fe and N in the support.

In summary, this dissertation mainly concentrates on the preparation of functional carbon materials for energy-related applications, like supercapacitor electrodes and supports for NPs in hydrogen release from formic acid. We hope that the functionalization strategies of carbon materials described in this dissertation could encourage more researchers to explore more potential candidates in the practical applications of energy storage and catalysis.

Content

Chapter 1

Introduction

As the quick development of global economy and the popularity of industries, the energy shortages of fossil fuels and corresponding pollutions have become big challenges for human beings. Thus, the investigation on efficient energy storage and conversion devices, such as lithium ion batteries, supercapacitors, and fuel cells is of vital significance in modern society.[1] In comparison with the traditional batteries, supercapacitors are famous for these properties, such as high power density, environmental friendly, and superb cyclic performance (> 100 000 cycles).[2] It has proven that supercapacitors are one of the most effective electrochemical energy-storage devices for practical applications, especially in areas that requires high power densities. Notably, functional carbons are recognized as promising electrodes for supercapacitor, owing to the available modifications or functionalizations to tailor the electronic structures through various synthesis and activation strategies. The mechanism of supercapacitor is based on two kinds of behaviors. One is based on the ion accumulation procedure in the electrolyte/electrodes interface, called double-layered capacitor (EDLC). The other is ascribed to the redox reaction, in which *pseudo*-capacitance process occurs. [2c]

On the other hand, to prevent the global energy crisis, it is imperative to develop effective, renewable and clean energy carriers. Hydrogen is considered as a promising energy carrier for future, owing to its high energy capability, non-pollution and renewable nature. Because of the increasing energy consumption and growing

population on earth, clean and diversified energy sources are urgently needed nowadays. Among available energy-related strategies, hydrogen fuel cells received considerable attention, because of its clean production of power with zero or low emissions in a high efficiency. Accordingly, appropriate hydrogen storage materials are required to store and generate hydrogen in a safe and controllable way for fuel cells. As we all know, hydrogen owns the high energy density of 120 MJ kg^{-1} for lower heating value (LHV), 2.7 times than that of petroleum (45 MJ kg^{-1} for LHV).[3] Physically hydrogen adsorption on traditional zeolites, carbons, and other porous materials usually reveals low adsorption capacity of hydrogen in moderate conditions.[4] Additionally, metal hydrides often require high temperatures to release hydrogen which largely increases the cost.[5] To achieve the hydrogen-powered society, liquid chemical hydrides have been received extensive attention for rapidly and efficiently generating hydrogen even under the mild conditions.[6] The chemical hydrogen storage materials not only own sufficient hydrogen capacity but also have acceptable costs, making them promising hydrogen carriers for hydrogen fuel cell vehicles. Liquid chemical hydrides, such as formic acid, are easy to prepare, save and transport, which is presented as ideal hydrogen carrier for practical use.

1.1 Electrochemical capacitor

1.1.1 Metal-organic framework-derived carbons as electrodes

The first electrochemical capacitors were used in practice by General Electric in 1957 for electrical charge storage.[7] Since then, supercapacitors have attracted much attention in a variety of areas, including electric vehicles and power systems, because of impressive power density and outstanding cycle performance as well as rapid

charge/discharge.[8] A variety of materials have been studied and used as supercapacitor electrodes, including carbon-based materials, conducting polymers, and metal oxides.[9] Due to the intriguing properties, functional carbon materials have been widely used for energy application (Figure 1.1). The recently emerging metal-organic frameworks (MOFs) constructed from metal salt and organic ligands have captivated a lot of interesting and become one of the hot issues at electrochemical energy storage, because of the good thermal stability, high ordered channels, three-dimensional pore structures and tunable pore size.[10] These interesting properties make MOFs outstanding precursors or sacrificial templates to synthesize the functional carbons (bearing features of hierarchical porosity or surface modification) for energy storage and conversion applications, especially for supercapacitors, lithium ion batteries and so on.[11]

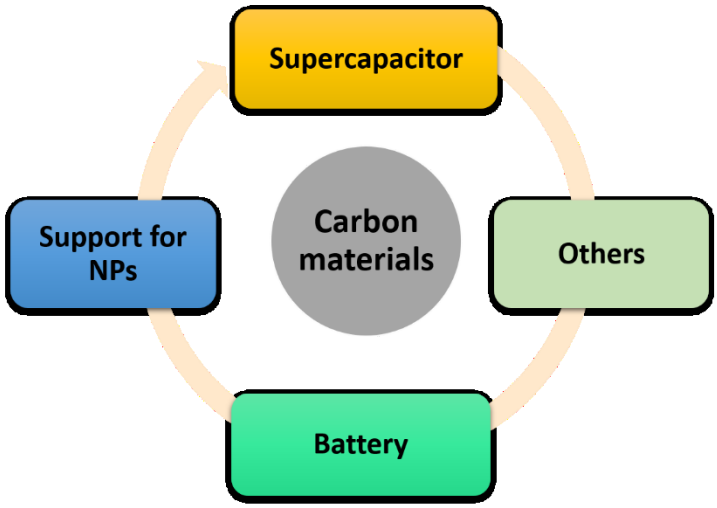

Figure 1.1 Functional carbon materials for energy applications.

In recent years, MOF-derived porous carbons are considerably employed as supercapacitor electrodes, benefiting from the well-defined pore structures and high

surface areas. On the other hand, there are many strategies to synthesize MOF-derived porous carbons, such as template carbonization, and chemical vapor deposition (CVD) coupled with physical or chemical activation.[12] Normally, during the pyrolysis of MOFs, MOFs play a role of self-sacrificial template. As a result, it is difficult to retain the original morphologies and structures of the parent MOFs in the consequent porous carbon products. Until now, porous carbons derived from MOF series, such as material institut lavoisier (MILs), isoreticular metal-organic frameworks (IRMOFs), and zeolitic imidazolate frameworks (ZIFs), have demonstrated superior characters in energy storage. In particular, ZIF-8 and MOF-5 have been presented as prospective self-sacrificial templates to fabricate functionally porous carbon materials with novel properties.

1.1.2 Pore tailoring

Lately, the research on tailoring porosity of porous carbon materials have attracted much interest, especially the hierarchical pore structures ranging from micropore to macropore level and even the voids between particles.[13] It has been indicated that the micropores serve as the ion traps in which the charge storage occurs, while the mesopores or/and macropores are utilized as the ion diffusion reservoirs to decrease the transport paths for ions to the micropores.[14] To synthesize hierarchically porous carbons derived from MOFs, researchers have been dedicating to the architectural designs and studying the influence factors of hierarchical porosity by many kinds of synthetic methods.[15] For example, Zhan *et al* reported three dimensional hierarchically porous carbon derived from MOF and glucose as EDLC electrode materials.[16] Interestingly, glucose was infiltrated into the surface or internal pores of MOF, and then polymerized

and consequently carbonized to form hierarchically porous carbons. Afterwards, in 2014, Xu *et al* proposed a new strategy to effectively control hierarchical pore structures through a double-template approach and they successfully introduced large nanopores on basis of retaining the original micropores.[17] Besides, Xu *et al* also used the ultrasonication way to prepare assembled ZIF-8 nanoparticles and successfully induced mesopores and macropores as additional second-order structures.[18]

In consideration of the pore structures which are closely related to the high-performance devices, it is of significance to construct the hierarchical porosity of MOFs and MOF-derived porous carbons. In a word, MOF-derived porous carbon materials not only possess excellent properties like what MOFs precursors do in some aspects, but also reveal their potential applications in energy storage. Hierarchical porosity in porous carbons can promote the ion or mass transportation and result in the capability enhancement of supercapacitors. MOF-derived porous carbons with hierarchical characters could have a chance to create a brand-new outlook for MOFs family in future.

1.2 Liquid chemical hydrides

1.2.1 Formic acid

Formic acid (FA, HCOOH) is a liquid under the ambient conditions with a high hydrogen content of 4.4 wt%. Formic acid, as a product from biomass processing, has the advantages of non-toxicity, good stability, and easy storage and transport, making it available as a liquid hydrogen carrier for fuel cells. It has been revealed that the catalytic decomposition of FA has two pathways as shown in Equations (1.1) and (1.2). However, the pathway (1.2) is undesirable for hydrogen generation, because CO impurity is toxic for catalysts in fuel cells and thus should be avoided.[19] In pathway

(1.1), FA releases only two gases, hydrogen and carbon dioxide, in the presence of a suitable catalyst. Besides hydrogen, the other product CO_2 can afford a carbon-neutral cycle (Figure 1.2).[20] Hence, preparation of the catalysts with excellent hydrogen selectivity and fast kinetic property is of vital significance for CO-free decomposition in FA-based hydrogen storage. Furthermore, noble metals have been widely investigated with excellent catalytic activity compared to non-noble metals which are easily eroded by the acidic FA.

$$HCOOH \rightarrow H_2\,(g) + CO_2\,(g) \qquad (1.1)$$

$$HCOOH \rightarrow H_2O + CO\,(g) \qquad (1.2)$$

To data, a large number of articles have reported various methods to fabricate and optimize the metal NP catalysts, demonstrating wonderful catalytic properties for hydrogen release of FA.[21] In contrast to homogeneous catalysts, heterogeneous catalysts receive more attention, because that the latter are more probable to use in practice, considering the easy separation from the reaction mixture, excellent recycling and appropriate reaction temperature.[22]

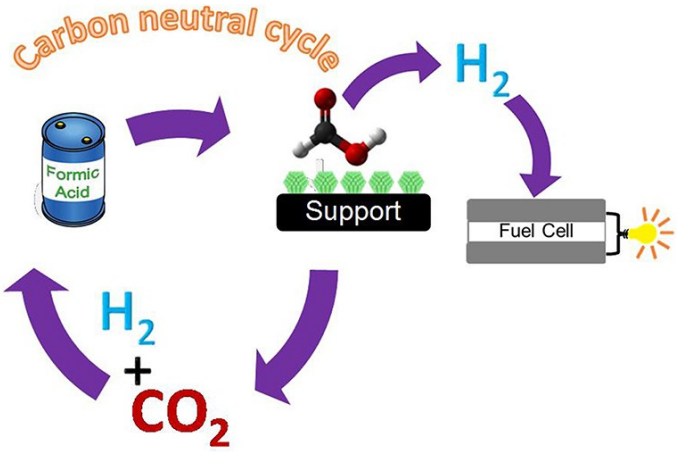

Figure 1.2 Hydrogen generation from formic acid for carbon-neutral energy storage over supported metal NP catalysts.[20c]

1.2.2 Metal nanoparticles for dehydrogenation

It is found that the corresponding catalytic activity largely depends on the metal NPs and the support as well as the interaction between them. The high surface energies of ultrasmall NPs may result in the thermodynamical instability and agglomeration, causing the degradation of catalytic property. Thus, stabilization of NP catalysts with uniform dispersion is very important. On one hand, the well-constructed support can achieve the stabilization of NPs without aggregation, on account of strong interaction between the metal NPs and the support. Regarding this, massive efforts from researchers have been made to use appropriate supports for immobilizing the NPs, like activated carbon, graphene, MOFs, MOF-derived nanomaterials, and porous organic cages (POCs).[23] On the other hand, heterometallic NPs, especially bimetallic NPs have enhanced catalytic efficiencies compared to their monometallic counterparts, because of the strong synergy between the components.[24]

It is found that some metal NP catalysts (noble metals and their composites) exhibit the outstanding catalytic properties for dehydrogenation from liquid chemical

hydrides.[25] Besides, among the investigated catalysts, it has been found that Pd NP are promising catalysts towards FA dehydrogenation. One reason is that metal Pd NPs are more tolerant to carbon monoxide than other metals. Furthermore, Pd NPs have high selectivity for the reaction of hydrogen release from FA.[20c] Therefore, many researchers have made great efforts to design the unique Pd-based NPs in aspects of sizes, structures, and compositions, together with the metal-support interactions and so on .

1.2.2.1 Monometallic catalysts

In recent years, a variety of excellent metal NP catalysts (Au, Pd, and Ag) synthesized by unique synthetic strategies for FA decomposition in an aqueous FA/SF (sodium formate) solution have been published in large numbers.[26] The catalytic activities could be effectively improved by tailoring several aspects, including the sizes and compositions of NPs, heteroatom modifications, electronic features and interactions between NPs and supports.[27]

Xu *et al* synthesized the amine-functionalized Au NPs encapsulated into the silica nanospheres through the reduction of $HAuCl_4$ using $NaBH_4$ in the reversed micelle system, completely converting FA to the gases (H_2 and CO_2) at 90 ^oC in 360 min, indicating 100% hydrogen selectivity (n_{Au}/n_{FA} = 0.002, n_{FA}/n_{SF} = 3).[28] In contrast, in the absence of amine functionalization, the resultant catalyst showed no activity for FA dehydrogenation. This could be ascribed to the strong metal-molecular support interaction (SMMSI), which is effective to enhance the activity for hydrogen generation from aqueous FA. Afterwards, they prepared the effectively-alkalized rGO (PDA-rGO) supported Pd NPs applied for FA dehydrogenation, in which Pd NPs were robustly anchored on graphene surface.[29] The Pd NPs exhibited uniform dispersity with small

particle sizes of less than 1.5 nm. Without the usage of PDA, the resultant Pd NPs were observed with aggregations in large particle sizes of 10 nm, demonstrating that the diamine groups effectively control the growth and size of NPs on diamine-alkalized rGO. For FA decomposition over the Pd/PDA-rGO catalyst, the FA decomposition reaction was completed within 1.05 min, providing a TOF value of 3810 h^{-1} at 50 ^{o}C (n_{Pd}/n_{FA} = 0.015, n_{FA}/n_{SF} = 1:1). As for the mechanism, the alkaline group is used as a proton scavenger and favorable for O-H cleavage in formic acid molecule, offering a Pd-formate intermediate and -$[H_2NH]^+$ in the first step. Then, the Pd-formate occurs β-hydride elimination, releasing CO_2 and the [H-Pd] species. Finally, the - $[H_2NH]^+$ and the [H-Pd] species react to evolve H_2.

1.2.2.2 Bimetallic catalysts

According to the many research works, bimetallic NPs often display higher catalytic activity than that of their monometallic counterparts, owing to the powerful synergetic effects between the components.[30] Researches has indicated that Pd-based bimetallic catalysts with Au or Ag additive could effectively improve the activity towards FA dehydrogenation.[31] The AgPd NPs immobilized on rGO through a novel non-noble-metal sacrificial approach (NNMSA) has been successfully synthesized, in which $Co_3(BO_3)_2$ material was subsequently removed by the acid. The as-prepared (Co_6) $Ag_{0.1}Pd_{0.9}$/rGO catalyst revealed the highest activity for the complete hydrogen release from FA within 1.1 min, with a TOF value of 2739 h^{-1} at 50 ^{o}C (n_{AgPd}/n_{FA} = 0.02, n_{FA}/n_{SF} = 1:2.5).[32] Without employing NNMSA, much aggregation of metal particles were obviously detected on the $Ag_{0.1}Pd_{0.9}$/rGO catalyst, showing that this kind of sacrificial approach could result in the uniform dispersion of AgPd NPs without

aggregation. Very recently, Xu *et al* reported highly active AuPd NPs immobilized on N-modified porous carbon by using a novel phosphate-mediation strategy, which demonstrates an outstanding catalytic performance for FA decomposition at room temperature.[22] The corresponding turnover frequency (TOF) is as high as 5400 h^{-1} at 30 ^{o}C.

1.2.3 Support materials

Until now, a large amount of materials has been synthesized to support or immobilize the metal NPs for enhancing the catalytic performance in FA decomposition. These supports include silicon, metal oxide, MOF-derived porous carbons, active carbons, graphene-based materials and so on.[33] Besides, carbon supports have been widely investigated by researchers, because of their advantages, like large surface area, heteroatom doping or hierarchical porosity.

Maxsorb MSC-30 carbon with a large surface area was utilized as the support to well disperse the Pd NPs, leading to the complete generation of hydrogen even at a low temperature of 25 ^{o}C.[34] Outstandingly, this NaOH-assisted reduction method could control the resultant Pd NP size (~2.3 nm) in the period of the synthesis, which is smaller than that of Pd NPs without NaOH addition (~3.6 nm). Pd/MSC-30 in the presence of NaOH completely released the gases within 2.33 min and no CO contamination was detected, affording a TOF value of 2623 h^{-1} at 50 ^{o}C (n_{Pd}/n_{FA} = 0.01, n_{FA}/n_{SF} = 1:1). What's more, this catalyst also demonstrated superb stability with negligible loss after 5 cycles for FA dehydrogenation.

Later, nitrogen-doped hierarchically porous carbon derived from Al-MIL-101-NH_2 was fabricated, displaying the existence of micro- and mesoporosity.[35] Then, this carbon

was employed as support to immobilize Pd NPs, which not only revealed an ultranfine Pd particle size of ~ 1.1 nm, but also demonstraed an outstanding catalytic activity. The corresponding TOF was as high as 14 400 h^{-1} at 60 ^{o}C (n_{Pd}/n_{FA} = 0.017, n_{FA}/n_{SF} = 1:3). The abundant porosity could promote the mass transport during the reaction. Besides, the ultrafine NPs and the nitrogen species in the carbon support are also responsible for the superb catalytic property.

The effective strategy to stabilize the NPs on the surface is to modify the supports with various heteroatoms, such as nitrogen, phosphorus, oxygen, sulphur, and boron.[36] These could result in a lot of active sites and alter the electronic properties of supports. Combined with the intrinsic characters of carbon materials (such as excellent thermal stability and electrical conductivity), doping carbons with heteroatoms or even other nonnoble metal-based materials are favorable to optimize the structure or electronic property of carbon framework, thus leading to the strong interactions between metal NPs and the support, together with the ultrafine metal particle sizes. Until now, few researches about immobilizing Pd NPs on boron- or other nonnoble metal-doped carbons for FA dehydrogenation have been reported.

1.3 Scope of the present work

This work concentrates on the preparation of functional carbon materials applied as 1) electrodes for supercapacitors and 2) supports to immobilize metal NPs for fast hydrogen generation from formic acid.

(i) Hierarchically Porous Carbons Derived from Metal-Organic Framework/Chitosan Composites for High-Performance Supercapacitors

The facile synthesis of hierarchically porous carbons through the calcination of meta-organic framework (MOF)/chitosan composites is reported. The effects of chitosan (CS) addictive on the pore structures of resultant carbons are discussed. The corresponding MOF/chitosan precursors could be readily converted into hierarchically porous carbons (NPC-*V*, *V* = 1, 2, 4, and 6) with much higher ratios of meso-/macropore volume to micropore volume ($V_{meso\text{-}macro}/V_{micro}$). The derived carbon NPC-2 with the high ratio of $V_{meso\text{-}macro}/V_{micro}$ = 1.47 demonstrates a high specific surface area of 2375 m^2 g^{-1}, and a high pore volume of 2.49 cm^3 g^{-1}, as well as a high graphitization degree, comparison with its counterpart (NPC) without chitosan addition. These excellent features are favorable of rapid ion diffusion/transport, endowing NPC-2 with enhanced electrochemical behaviors as supercapacitor electrodes in a symmetric-electrode system, corresponding to a high specific capacitance of 199.9 F g^{-1} in the aqueous electrolyte and good rate capability. Good cycling stability is also observed after 10 000 cycles. This part was described in Chapter 2.

(ii) Immobilizing Palladium Nanoparticles on Boron-Oxygen-Functionalized Carbon Nanospheres towards Efficient Hydrogen Generation from Formic Acid

Carbon nanospheres (XC-72R) were functionalized by boron-oxygen (B-O) through coannealing with boric acid, to which highly dispersed palladium nanoparticles (Pd NPs) (~ 1.7 nm) were immobilized by a wet chemical reduction for the first time. The resultant Pd/OB-C catalyst exhibits significantly improved activity for the dehydrogenation from formic acid (FA) compared to pristine XC-72R supported Pd NPs (Pd/C). Impressively, by adding melamine precursor, the B-O and nitrogen (N)-functionalized product OB-C-N displays an extremely high B content, ca. 34 times higher than OB-C. The Pd/OB-C-N catalyst with an ultrafine Pd particle size of ~ 1.4

nm shows a superb activity, with a turnover frequency (TOF) as high as 5354 h^{-1} at 323 K, owing to the uniform ultrafine Pd NPs and the effect from B-O and N functionalities. This part was described in Chapter 3.

(iii) Immobilizing Ultrafine Palladium Nanoparticles on Fe_3C/Fe- and N-functionalized Porous Carbon towards Fast Hydrogen Generation from Formic Acid

A Fe_3C/Fe- and N-functionalized porous carbon with a micro-/mesoporous porostiy was synthesized. This distinct carbon (Fe_3C-Fe@NC) was used as a support to immobilize palladium nanoparticles (Pd NPs) (~ 1.4 nm) using a wet chemical reduction method. The Pd/Fe_3C-Fe@NC catalyst exhibits a superb activity for formic acid (FA) dehydrogenation, providing a rather high turnover frequency (TOF) of 7361 h^{-1} at 323 K, attributed to the ultrafine Pd NPs and the effects from Fe_3C/Fe and N in the support. This part was described in Chapter 4.

References

[1] a) J. P. Paraknowitsch, A. Thomas, *Energy Environ. Sci*. **2013**, *6*, 2839-2855; b) J. K. Sun, Q. Xu, *Energy Environ. Sci*. **2014**, *7*, 2071-2100; c) A. G. Pandolfo, A. F. Hollenkamp, *J. Power Sources* **2006**, *157*, 11-27; d) M. Winter, R. J. Brodd, *Chem. Rev*. **2004**, *104*, 4245-4270; e) D. Sheberla, J. C. Bachman, J. S. Elias, C. J. Sun, Y. Shao-Horn, M. Dincă, *Nat. Mater*. **2017**, *16*, 220-224; f) S. Sundriyal, H. Kaur, S. K. Bhardwaj, S. Mishra, K. Kim, A. Deep, *Coord. Chem. Rev*. **2018**, *369*, 15-38; g) A. F. Ambrose, A. Q. Al-Amin, R. Rasiah, R. Saidur, N. Amin, *Int. J. Hydrogen Energy* **2017**, *42*, 9125-9134.

[2] a) D. W. Wang, F. Li, Z. G. Chen, G. Q. Lu, H. M. Cheng, *Chem. Mater*. **2008**, *20*,

7195-7200; b) E. Frackowiak, F. Beguin, *Carbon* **2001**, *39*, 937-950; c) L. L. Zhang, X. S. Zhao, *Chem. Soc. Rev*. **2009**, *38*, 2520-2531; d) H. Q. Li, R. L. Liu, D. Y. Zhao, Y. Y. Xia, *Carbon* **2007**, *45*, 2628-2635; e) Y. Pan, Y. X. Zhao, S. J. Mu, Y. Wang, C. M. Jiang, Q. Z. Liu, Q. R. Fang, M. Xue, S. L. Qiu, *J. Mater. Chem. A* **2017**, *5*, 9544-9552.

[3] a) Q. L. Zhu, Q. Xu, *Energy Environ. Sci*. **2015**, *8*, 478-512; b) I. P. Jain, *Int. J. Hydrogen Energy* **2009**, *34*, 7368-7378; c) P. Zegers, *J. Power Sources* **2006**, *154*, 497-502; d) L. Schlapbach, *Nature* **2009**, *460*, 809-811; e) P. Rohani, S. Kim, M. T. Swihart, *Adv. Energy Mater*. **2016**, *6*, 1502550.

[4] a) V. Meregalli, M. Parrinello, *Appl. Phys. A* **2001**, *72*, 143-146; b) F. L. Darkrim, P. Malbrunot, G. P. Tartaglia, *Int. J. Hydrogen Energy* **2002**, *27*, 193-202; c) J. Sculley, D. Yuan, H. C. Zhou, *Energy Environ. Sci*. **2011**, *4*, 2721-2735.

[5] a) D. Pukazhselvan, V. Kumar, S. K. Singh, *Nano Energy* **2012**, *1*, 566-589; b) W. Grochala, P. P. Edwards, *Chem. Rev.* **2004**, *104*, 1283-1316.

[6] a) M. Yadav, Q. Xu, *Energy Environ. Sci.* **2012**, *5*, 9698-9725; b) X. C. Yang, Q. Xu, *Chinese J. Catal.* **2016**, *37*, 1594-1599; c) H. L. Jiang, Q. Xu, *Catal. Today* **2011**, *170*, 56-63.

[7] R. Kotz, M. Carlen, *Electrochim. Acta* **2000**, *45*, 2483-2498.

[8] a) J. R. Miller, P. Simon, *Science* **2008**, *321*, 651-652; b) M. D. Stoller, S. Park, Y. W. Zhu, J. An, R. S. Ruoff, *Nano Lett*. **2008**, *8*, 3498-3502; c) Y. Wang, Z. Q. Shi, Y. Huang, Y. F. Ma, C. Y. Wang, M. M. Chen, Y. S. Chen, *J. Phys. Chem. C* **2009**, *113*, 13103-13107.

[9] a) J. Chmiola, G. Yushin, Y. Gogotsi, C. Portet, P. Simon, P. L. Taberna, *Science*

2006, *313*, 1760-1763; b) Y. W. Zhu, S. Murali, M. D. Stoller, K. J. Ganesh, W. W. Cai, P. J. Ferreira, A. Pirkle, R. M. Wallace, K. A. Cychosz, M. Thommes, D. Su, E. A. Stach, R. S. Ruoff, *Science*, **2011**, *332*, 1537-1541; c) Y. Pan, Y. X. Zhao, S. J. Mu, Y. Wang, C. M. Jiang, Q. Z. Liu, Q. R. Fang, M. Xue, S. L. Qiu, *J. Mater. Chem. A* **2017**, *5*, 9544-9552; d) J. Zhi, O. Reiser, F. Q. Huang, *ACS Appl. Mater. Interfaces* **2016**, *8*, 8452-8459; e) X. H. Cao, B. Zheng, W. H. Shi, J. Yang, Z. X. Fan, Z. M. Luo, X. H. Rui, B. Chen, Q. Y. Yan, H. Zhang, *Adv. Mater.* **2015**, *27*, 4695-4701; f) V. D. Nithya, N. S. Arul, *J. Mater. Chem. A* **2016**, *4*, 10767-10778; g) G. A. Snook, P. Kao, A. S. Best, *J. Power Sources* **2011**, *196*, 1-12.

[10] W. Xia, A. Mahmood, R. Q. Zou, Q. Xu, *Energy Environ. Sci.* **2015**, *8*, 1837-1866.

[11] a) H. L. Wang, Q. L. Zhu, R. Q. Zou, Q. Xu, *Chem* **2017**, *2*, 52-80; b) K. Shen, X. D. Chen, J. Y. Chen, Y. W. Li, *ACS Catal*. **2016**, *6*, 5887-5903.

[12] a) B. Liu, H. Shioyama, T. Akita, Q. Xu, *J. Am. Chem. Soc.* **2008**, *130*, 5390-5391; b) H. L. Jiang, B. Liu, Y. Q. Lan, K. Kuratani, T. Akita, H. Shioyama, F. Q. Zong, Q. Xu, *J. Am. Chem. Soc.* **2011**, *133*, 11854-11857; c) S. Zhong, C. X. Zhan, D. P. Cao, *Carbon* **2015**, *85*, 51-59; d) P. Zhang, F. Sun, Z. H. Xiang, Z. G. Shen, J. Yun, D. P. Cao, *Energy Environ. Sci.* **2014**, *7*, 442-450; e) Q. L. Zhu, P. Pachfule, P. Strubel, Z. P. Li, R. Q. Zou, Z. Liu, S. Kaskel, Q. Xu, *Energy Stor. Mater*. **2018**, *13*, 72-79.

[13] a) G. Srinivas, V. Krungleviciute, Z. X. Guo, T. Yildirim, *Energy Environ. Sci.* **2014**, *7*, 335-342; b) S. J. Yang, T. Kim, K. Lee, Y. S. Kim, J. Yoon, C. R. Park, *Carbon* **2014**, *71*, 294-302; c) M. J. Zhi, F. Yang, F. Meng, M. Q. Li, A. Manivannan, N. Q. Wu, *ACS Sustainable Chem. Eng*. **2014**, *2*, 1592-1598.

[14] a) B. Liu, H. Shioyama, H. L. Jiang, X. B. Zhang, Q. Xu, *Carbon* **2010**, *48*, 456-463; b) P. Simon, Y. Gogotsi, *Nat. Mater*. **2008**, *7*, 845-854; c) C. Liu, F. Li, L. P. Ma, H. M. Cheng, *Adv. Mater*. **2010**, *22*, 28-62; d) M. J. Zhi, C. C. Xiang, J. T. Li, M. Li, N. Q. Wu, *Nanoscale* **2013**, *5*, 72-88.

[15] a) P. Zhang, F. Sun, Z. G. Shen, D. P. Cao, *J. Mater. Chem. A* **2014**, *2*, 12873-12880; b) Y. B. Huang, P. Pachfule, J. K. Sun, Q. Xu, *J. Mater. Chem. A* **2016**, *4*, 4273-4279; c) P. Pachfule, D. Shinde, M. Majumder, Q. Xu, *Nat. Chem*. **2016**, *8*, 718-724; d) R. R. Salunkhe, J. Tang, N. Kobayashi, J. Kim, Y. Ide, S. Tominaka, J. H. Kim, Y. Yamauchi, *Chem. Sci*. **2016**, *7*, 5704-5713; e) W. Chaikittisilp, K. Ariga, Y. Yamauchi, *J. Mater. Chem. A* **2013**, *1*, 14-19; f) J. Yang, H. L. Wu, M. Zhu, W. J. Ren, Y. Lin, H. B. Chen, F. Pan, *Nano Energy* **2017**, *33*, 453-461.

[16] S. L. Jin, H. G. Deng, Z. Liang, W. M. Qiao, L. C. Ling, *New Carbon Mater*. **2012**, *27*, 87-92.

[17] J. K. Sun, Q. Xu, *Chem. Commun*. **2014**, *50*, 13502-13505.

[18] A. J. Amali, J. K. Sun, Q. Xu, *Chem. Commun*. **2014**, *50*, 1519-1522.

[19] a) B. Loges, A. Boddien, F. Gärtner, H. Junge, M. Beller, *Top. Catal.* **2010**, *53*, 902-914; b) Z. P. Li, Q. Xu, *Acc. Chem. Res.* **2017**, *50*, 1449-1458; c) T. He, P. Pachfule, H. Wu, Q. Xu, P. Chen, *Nat. Rev. Mater.* **2016**, *1*, 16059.

[20] a) S. Moret, P. J. Dyson, G. Laurenczy, *Nat. Chem.* **2014**, *5*, 4017; b) J. F. Hull, Y. Himeda, W. H. Wang, B. Hashiguchi, R. Periana, D. J. Szalda, J. T. Muckerman, E. Fujita, *Nat. Chem.* **2012**, *4*, 383; c) M. Navlani-García, K. Mori, D. Salinas-Torres, Y. Kuwahara, H. Yamashita, *Front. Mater*. **2019**, *6*, 44.

[21] H. L. Jiang, Q. Xu, *J. Mater. Chem.* **2011**, *21*, 13705-13725.

[22] Q. J. Wang, L. Y. Chen, Z. Liu, N. Tsumori, M. Kitta, Q. Xu, *Adv. Funct. Mater.* **2019***, 29,* 1903341.

[23] a) X. J. Gu, Z. H. Lu, H. L. Jiang, T. Akita, Q. Xu, *J. Am. Chem. Soc.* **2011**, *133*, 11822-11825; b) Q. L. Zhu, N. Tsumori, Q. Xu, *J. Am. Chem. Soc.* **2015**, *137*, 11743-11748; c) H. L. Jiang, T. Akita, T. Ishida, M. Haruta, Q. Xu, *J. Am. Chem. Soc.* **2011**, *133*, 1304-1306; d) X. C. Yang, P. Pachfule, Y. Chen, N. Tsumori, Q. Xu, *Chem. Commun.* **2016**, *52*, 4171-4174; e) N. Tsumori, L. Y. Chen, Q. J. Wang, Q. L. Zhu, M. Kitta, Q. Xu, *Chem* **2018**, *4*, 845-586; f) X. C. Yang, J. K. Sun, M. Kitta, H. Pang, Q. Xu, *Nat. Catal.* **2018**, *1*, 214-220.

[24] A. K. Singh, Q. Xu, *ChemCatChem* **2013**, *5*, 652-676.

[25] a) J. M. Yan, X. B. Zhang, T. Akita, M. Haruta, Q. Xu, *J. Am. Chem. Soc.* **2010**, *132*, 5326-5327; b) P. Z. Li, A. Aijaz, Q. Xu, *Angew. Chem., Int. Ed.* **2012**, *51*, 6753-6756; c) M. Iguchi, Y. Himeda, Y. Manaka, H. Kawanami, *ChemSusChem* **2016**, *9*, 2749-2753; d) A. Boddien, D. Mellmann, F. Gärtner, R. Jackstell, H. Junge, P. J. Dyson, G. Laurenczy, R. Ludwig, M. Beller, *Science* **2011**, *333*, 1733-1736.

[26] a) M. Yadav, A. K. Singh, N. Tsumori, Q. Xu, *J. Mater. Chem.* **2012**, *22*, 19146-19150; b) Z. P. Li, X. C. Yang, N. Tsumori, Z. Liu, Y. Himeda, T. Autrey, Q. Xu, *ACS Catal.* **2017**, *7*, 2720-2724.

[27] a) M. Navlani-García, D. Salinas-Torres, K. Mori, A. F. Léonard, Y. Kuwahara, N. Job, H. Yamashita, *Catal. Today* **2019**, *324*, 90-96; b) D. Salinas-Torres, M. Navlani-García, K. Mori, Y. Kuwahara, H. Yamashita, *Appl. Catal. A: Gen*. **2019**, *571*, 25-41; c) M. Navlani-García, K. Mori, Y. Kuwahara, H. Yamashita, *NPG Asia Mater*. **2018**, *10*, 277-292; d) M. Navlani-García, D. Salinas-Torres, K. Mori, Y.

Kuwahara, H. Yamashita, *Int. J. Hydrogen Energy* **2019**, *44*, 28483-28493.

[28] M. Yadav, T. Akita, N. Tsumori, Q. Xu, *J. Mater. Chem.* **2012**, *22*, 12582-12594.

[29] F. Z. Song, Q. L. Zhu, N. Tsumori, Q. Xu, *ACS Catal.* **2015**, *5*, 5141-5144.

[30] W. Hong, M. Kitta, N. Tsumori, Y. Himeda, T. Autrey, Q. Xu, *J. Mater. Chem. A* **2019**, *7*, 18835-18839.

[31] a) S. Zhang, Ö. Metin, D. Su, S. Sun, *Angew. Chem., Int. Ed.* **2013**, *52*, 3681-3684; b) Y. Huang, X. Zhou, M. Yin, C. Liu, W. Xing, *Chem. Mater.* **2010**, *22*, 5122-5128.

[32] Y. Chen, Q. L. Zhu, N. Tsumori, Q. Xu, *J. Am. Chem. Soc.* **2015**, *137*, 106-109.

[33] a) M. Yurderi, A. Bulut, N. Caner, M. Celebi, M. Kaya, M. Zahmakiran, *Chem. Commun*. **2015**, *51*, 11417-11420; b) F. Z. Song, Q. L. Zhu, X. C. Yang, W. W. Zhan, P. Pachfule, N. Tsumori, Q. Xu, *Adv. Energy Mater*. **2018**, *8*, 1701416; c) Q. L. Zhu, F. Z. Song, Q. J. Wang, N. Tsumori, Y. Himeda, T. Autrey, Q. Xu*, J. Mater. Chem. A* **2018**, *6*, 5544-5549.

[34] Q. L. Zhu, N. Tsumori, Q. Xu, *Chem. Sci.* **2014**, *5*, 195-199.

[35] Q. J. Wang, N. Tsumori, M. Kitta, Q. Xu, *ACS Catal*. **2018**, *8*, 12041-12045.

[36] a) L. Xin, F. Yang, S. Rasouli, Y. Qiu, Z. F. Li, A. Uzunoglu, C. J. Sun, Y. Liu, P. Ferreira, W. Li, Y. Ren, L. A. Stanciu, J. Xie, *ACS Catal*. **2016**, *6*, 2642-2653; b) K. Koh, J. E. Seo, J. H. Lee, A. Goswami, C. W. Yoon, T. Asefa, *J. Mater. Chem. A* **2014**, *2*, 20444-20449.

Chapter 2

Hierarchically Porous Carbons Derived from Metal-Organic Framework/Chitosan Composites for High-Performance Supercapacitors

Hierarchically porous carbon materials with high surface areas are hopeful candidates for energy storage and conversion. Herein, we present the facile synthesis of hierarchically porous carbons through the calcination of meta-organic framework (MOF)/chitosan composites. The effects of chitosan (CS) addictive on the pore structures of resultant carbons are discussed. The corresponding MOF/chitosan precursors could be readily converted into hierarchically porous carbons (NPC-*V*, *V* = 1, 2, 4, and 6) with much higher ratios of meso-/macropore volume to micropore volume ($V_{meso\text{-}macro}/V_{micro}$). The derived carbon NPC-2 with the high ratio of $V_{meso\text{-}macro}/V_{micro}$ = 1.47 demonstrates a high specific surface area of 2375 $m^2\ g^{-1}$, and a high pore volume of 2.49 $cm^3\ g^{-1}$, as well as a high graphitization degree, comparison with its counterpart (NPC) without chitosan addition. These excellent features are favorable of rapid ion diffusion/transport, endowing NPC-2 with enhanced electrochemical behaviors as supercapacitor electrodes in a symmetric-electrode system, corresponding to a high specific capacitance of 199.9 F g^{-1} in the aqueous electrolyte and good rate capability. Good cycling stability is also observed after 10 000 cycles.

2.1 Introduction

Supercapacitors are regarded as highly efficient electrochemical devices for energy storage with high power density and long cycle life, which can satisfy the demand for energy utilization and consumption nowadays.[1] The energy storage mechanism of the electrochemical double-layered capacitor (EDLC) is ascribed to the ion adsorption/desorption at the interface between the electrolyte and electrodes, without occurrence of redox reaction. As we all know, the electrode materials have a crucial influence on the electrochemical behaviours of supercapacitors. Thus, many efforts have been devoted to synthesize the high-performance supercapacitor electrodes, which are expected to be applied in practice for the portable electronic systems.[2]

Until now, carbonaceous materials have received considerable attention as electrodes of EDLCs, due to their remarkable mechanical properties, superb thermal and electrical characters, and excellent chemical stabilities.[3] Generally, high surface areas, hierarchical pore distributions, and good electric conductivities are dramatically necessary for outstanding electrodes, which can afford excellent capacitive properties.[4] Traditional activated carbons (ACs) from the biomass precursors are widely utilized as supercapacitor electrodes, because of their high specific surface areas and pore volumes determined by the precursors and activation processes. Yet, ACs usually display uncontrollable pore structures and not-well-defined porosities with insufficient meso-/macropores, which could lower the capacitance of supercapacitors.[5] Specifically, the micropores serve as the ion traps where the charge storage occurs, while the meso-/macropores are used as the ion-diffusion reservoirs, which can diminish the transport paths for ions to the micropores.[6] Therefore, the structure of hierarchical porosity

ranging from micro- to macropores in carbon electrodes is of great significance for the enhancement of capacitive property. Recently, owing to the ordered channels, high surface areas, and tunable porous structures, metal-organic frameworks (MOFs), which are built by bridging metal ions/clusters with organic ligands, have been utilized as self-sacrificial templates to prepare the unique nanoporous materials via pyrolysis. Particularly, MOF-derived nanoporous carbons with distinct architectures are often used in applications of energy storage and conversion, like supercapacitors, gas storage, catalysis, batteries and fuel cells *etc*.[2a, 7] Actually, during the thermal treatment process of MOFs at high temperature of 600~1000 ^{o}C, it is inevitable to destroy the original structures or morphologies to some extent. Thereby, it is still a challenge to obtain the well-defined porous architectures for MOF-derived nanoporous carbons.

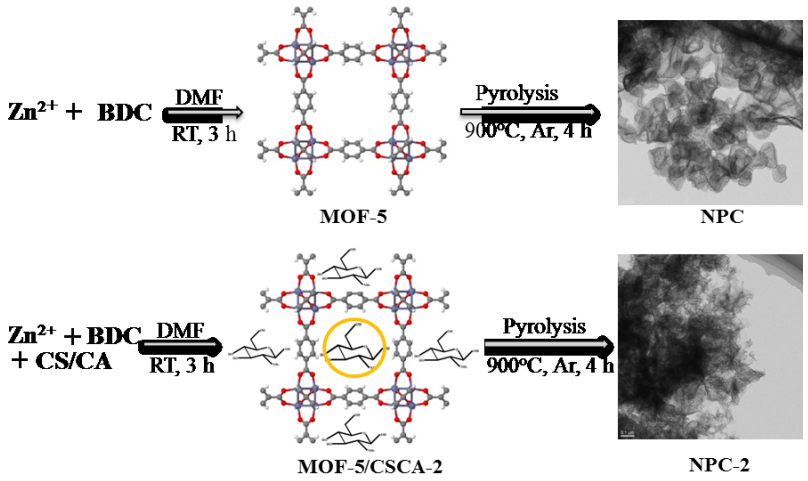

Figure 2.1 Schematic illustration of synthesis of NPC and NPC-2 *via* pyrolysis of MOF-5 and MOF-5/CSCA-2, respectively. The yellow circle in MOF-5/CSCA-2 means the chitosan molecules which are filled in the cavities.

Here, for the first time we report a facile strategy for the preparation of hierarchically porous carbons with micro-/meso-/macro porosities from the pyrolysis of MOF-

5/chitosan composites, followed by wash using acid (Figure 2.1). Through the optimization of synthetic conditions, the hierarchically porous carbon (NPC-2) not only shows a high ratio of $V_{meso\text{-}macro}/V_{micro}$ = 1.47, but also a very high specific surface area of 2375 m^2 g^{-1}, and total pore volume of 2.49 cm^3 g^{-1}. Chitosan is used as a pore structure-directing agent, which leads to the porous carbon framework NPC-2 with the enhanced surface area and pore volume. These greatly facilitate the rapid ion transport/diffusion and provide better performances for EDLCs. The combination of a high surface area, a high pore volume and hierarchical porosity with more mesopores endow NPC-2 itself with excellent supercapacitor performances, displaying high specific capacitance, good rate performance and excellent cycling stability in aqueous electrolyte.

2.2 Experimental section

2.2.1 Materials

All chemicals were commercial and used without further purification. Zinc nitrate hexahydrate ($Zn(NO_3)_2 \cdot 6H_2O$, 99%), chitosan ($(C_6H_{11}NO_4)_n$), and hydrochloric acid (HCl, 37%) were purchased from Wako Pure Chemical Industries. Sulfuric acid (H_2SO_4, 98%), citric acid monohydrate ($C_6H_8O_7 \cdot H_2O$, 99.5%), trimethylamine ($C_6H_{15}N$, 99%), methanol (CH_4O, 99.8%), and *N*,*N*-dimethylformamide (C_3H_7NO, 99.5%) were purchased from Kishida Chemical Co., Ltd. Terephthalic acid ($C_8H_6O_4$, 98%) was purchased from Sigma-Aldrich. Deionized (DI) water with a specific resistance of > 18.0 MΩ·cm was used in experiments.

2.2.2 Characterization and instrumentation

The microstructures were observed by JEOL JSM-IT100 scanning electron microscopy (SEM). Transmission electron microscopy (TEM) were performed on a Titan3 G2 60-300 (FEI) with a Super-X EDS system (Bruker) under operating voltage of 300 kV and a TECNAI G^2 F20 at an accelerating voltage of 200 kV. High-annular dark-field scanning TEM (HAADF-STEM) and elemental mapping analyses were recorded on a Titan3 G2 60-300 (FEI). The power X-ray diffraction (XRD) measurements were executed on a Rigaku Ultima IV X-ray diffractometer with a Cu Kα source. Thermo-gravimetric analyses (TGA) were recorded using a Rigaku Thermo plus EVO2/TG-DTA analyser under argon atmosphere at a heating speed of 10 $^{o}C\ min^{-1}$ from room temperature to 700 ^{o}C. Raman scattering spectra were obtained from a laser Raman microscope system (Nanophoton RAMANtouch) with an excitation wavelength of 532 nm. Fourier transform infrared spectroscopy (FTIR) analyses were performed on Shimadzu IRTracer-100 using ATR mode. Elemental analyses were carried out on CE EA1110 and Perkinelmer 2400II instruments. The metal content was measured by inductively coupled plasma optical emission spectroscopy (ICP-OES) on the Thermo Scientific iCAP6300. X-ray photoelectron spectroscopic (XPS) measurements were conducted on a Shimadzu ESCA-3400 X-ray photoelectron spectrometer using a Mg Kα source (10 kV, 10 mA). After drying under vacuum at 120 ^{o}C for 12 h, the N_2 adsorption/desorption isotherms were measured using automatic volumetric adsorption instrument (BELSORP-max) at 77 K. The surface areas and the pore size distributions were calculated using Brunauer-Emmett-Teller (BET) method and the non-localized density functional theory (NLDFT) method, respectively.

2.2.3 Syntheses of samples

1) Synthesis of MOF-5

MOF-5 was prepared using a reported facile procedure. $Zn(NO_3)_2 \cdot 6H_2O$ (1.52 g, 5.109 mmol) was dissolved in 25 mL of DMF at room temperature. A solution of BDC (0.638 g, 3.840 mmol) in another 25 mL of DMF was added under stirring, followed by introducing TEA (2.0 g, 33.835 mmol). The mixture was stirred for 3 h at room temperature. The precipitant was filtered and washed with DMF (2 × 40 mL) and methanol (2 × 40 mL). Finally, the sample was dried at 60 ^{o}C to afford MOF-5.

2) Syntheses of MOF-5/CSCA-*V* composites

Citric acid (CA) solution was prepared by dissolving citric acid monohydrate (0.25 g, 1.190 mmol) into 15 mL H_2O at room temperature. CS solution was prepared by adding chitosan (0.1 g) into the above CA solution, which was transferred into a Teflon-lined autoclave, heated to 130 ^{o}C over 0.5 h and kept at this temperature for 6 h. A certain volume of the above CS solution (V = 1, 2, 4, and 6 mL) was introduced into BDC (0.638 g, 3.840 mmol) in 25 mL of DMF, followed by mixing with $Zn(NO_3)_2 \cdot 6H_2O$ (1.52 g, 5.109 mmol) in another 25 mL of DMF under stirring. After adding TEA (2.0 g, 33.835 mmol), the mixture was stirred for 3 h at room temperature. The precipitant was filtered and washed with DMF (2 × 40 mL) and methanol (2 × 40 mL). Finally, the sample was dried at 60 ^{o}C to give MOF-5/chitosan composite, denoted as MOF-5/CSCA-V (V = 1, 2, 4, and 6).

3) Syntheses of hierarchically porous carbons of NPC-*V* and NPC

The MOF-5/CSCA-V sample (1.2 g) was transferred into a ceramic boat and placed in a tube furnace in an argon flow for 2 h at room temperature. Then, the temperature was raised to 175 ^{o}C and kept at this temperature for 1 h, and then raised to 900 ^{o}C and kept

at 900 ^{o}C for 4 h. After cooling down to room temperature, the black material was immersed in a 2 M HCl solution for 24 h with stirring, followed by washing with DI water and dried at 60 ^{o}C to give nanoporous carbons, denoted as NPC-*V* (*V* = 1, 2, 4, and 6). Using the same procedures, the carbon derived from MOF-5 is called NPC.

2.2.4 Syntheses of comparative samples

1) Synthesis of MOF-5-CA composite

The process is similar to that of MOF-5/CSCA-2, except no use of chitosan solid. Specifically, a citric acid (CA) solution was prepared by dissolving citric acid monohydrate (0.25 g, 1.190 mmol) into 15 mL H_2O at room temperature. 2 mL of the above CA solution was introduced into terephthalic acid (0.638 g, 3.840 mmol) in 25 mL of DMF, followed by mixing with $Zn(NO_3)_2 \cdot 6H_2O$ (1.52 g, 5.109 mmol) in another 25 mL of DMF under stirring. After adding trimethylamine (TEA) (2.0 g, 33.835 mmol), the mixture was stirred for 3 h at room temperature. The precipitant was filtered and washed with DMF (2 × 40 mL) and methanol (2 × 40 mL). Finally, the sample was dried at 60 ^{o}C to give the MOF-5-CA composite.

2) Syntheses of porous carbons (NPC-CA and NPC-2-*T*s)

NPC-CA was synthesized by pyrolysis of MOF-5-CA precursor, using the same heating program with that of NPC-2. Specifically, the MOF-5-CA was transferred into a ceramic boat and placed in a tube furnace in an argon flow for 2 h at room temperature. Then, the temperature was raised to 175 ^{o}C and kept at 175 ^{o}C for 1 h, and then raised to 900 ^{o}C and kept at 900 ^{o}C for 4 h. After cooling down to room temperature, the black material was immersed in a 2 M HCl solution for 24 h with stirring, followed by washing with DI water and dried at 60 ^{o}C to give nanoporous carbon, denoted as NPC-

CA.

NPC-2-*T*s (*T* = 700, 800, and 1000) were synthesized by the pyrolysis of MOF-5/CSCA-2 precursor at 700 ^{o}C, 800 ^{o}C, and 1000 ^{o}C, respectively. The heating program is the same as that of NPC-CA.

2.2.5 Electrochemical measurements

The electrochemical measurements were carried out under ambient conditions in a two-electrode capacitor with an aqueous solution of sulfuric acid (1.0 M) as electrolyte within a potential range from 0 to 1.0 V. Each electrode contains 2.0 mg of carbon material without adding any binder and conductive agent, in which a glassy paper separator was sandwiched between two electrodes and platinum plates were used as electronic collectors. The capacitor was evacuated for 1 h to allow the electrode material fully soaked in the electrolyte before the electrochemical measurements.

Cyclic voltammogram (CV) at different sweep rates for the capacitor was performed on a Solartron electrochemical workstation (SI1287). The specific capacitance is calculated according to Equation (2.1):

$$C = 2 \times \Delta Q / (\Delta V \times m), \qquad (2.1)$$

where ΔQ is the charge integrated from the whole voltage range, ΔV is the whole voltage difference, and m is the mass of carbon on an electrode. Galvanostatic charge/discharge (GC) examinations at various current densities were performed on a Solartron electrochemical workstation (SI1287). The specific capacitance of each electrode was calculated according to Equation (2.2):

$$C = 2 \times I \times \Delta t / (\Delta V \times m), \qquad (2.2)$$

where I is the discharge current, Δt is the discharge time, ΔV is the voltage difference within the discharge time Δt, and m is the mass of carbon on an electrode.

2.3 Results and discussion

2.3.1 Characterization

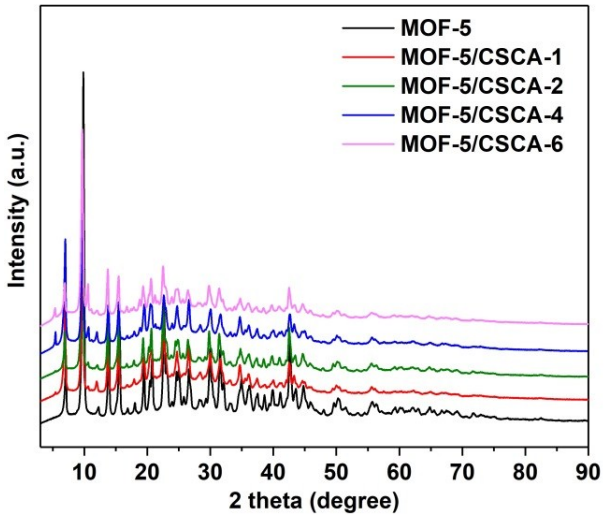

Figure 2.2 Power XRD patterns for MOF-5 and MOF-5/CSCA-*V* (*V* = 1, 2, 4, and 6) composites.

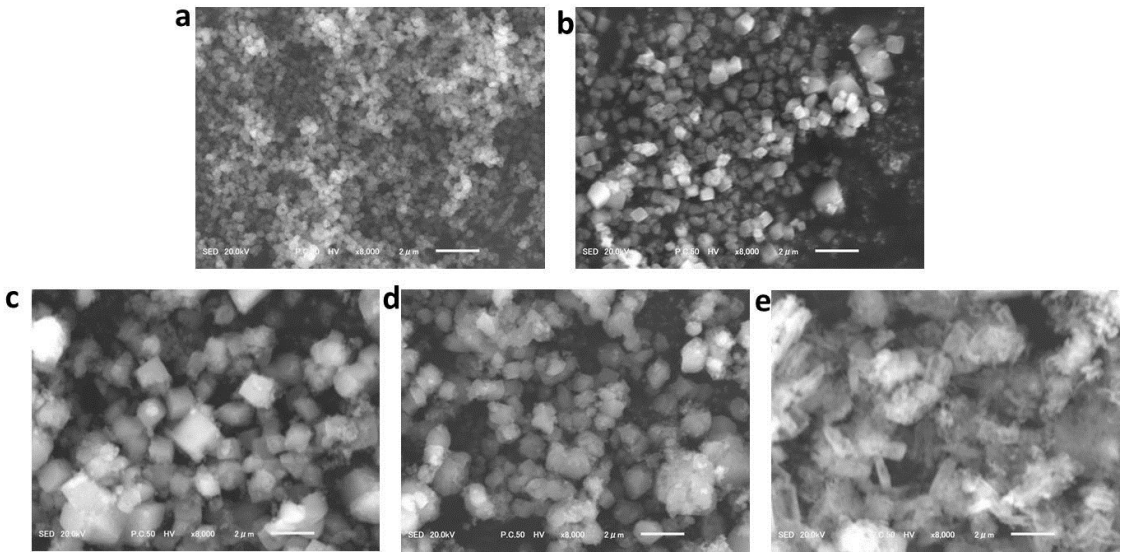

Figure 2.3 SEM images of (a) MOF-5, (b) MOF-5/CSCA-1, (c) MOF-5/CSCA-2, (d) MOF-5/CSCA-4, and (e) MOF-5/CSCA-6. Scale bar in a-e: 2μm.

MOF-5/CSCA-*V* (*V* = 1, 2, 4, and 6) was prepared at room temperature by mixing *N,N*-dimethylformamide (DMF) solution of terephthalic acid (BDC), a citric acid (CA) solution of CS, and DMF solution of Zn^{2+} metal, followed by adding trimethylamine (TEA). CSCA-*V* means the volume of CS solution used in the synthesis with *V* = 1, 2, 4, and 6 mL. The XRD patterns of MOF-5/CSCA-*V* (*V* = 1, 2, 4, and 6) show the preserved MOF-5 framework (Figure 2.2). SEM images are not exactly the same and the morphology of MOF-5/CSCA-6 is totally different from others, due to the excess CS solution of 6 mL (Figure 2.3). MOF-5/CSCA-2 shows good cubic structure (Figure 2.3c) with a particle size of ~ 1.2 μm, which is three times larger than that of MOF-5 (~ 340 nm).

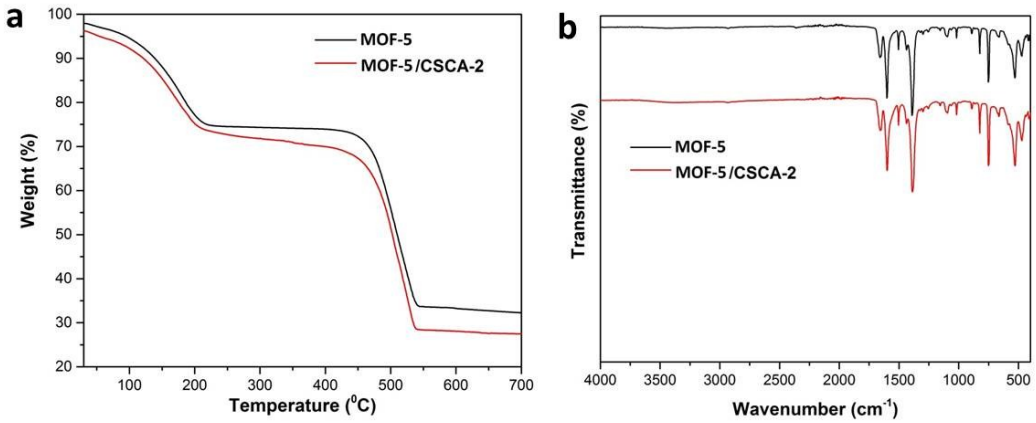

Figure 2.4 (a) TG and (b) FTIR curves of MOF-5 and MOF-5/CSCA-2.

TG and FTIR curves of MOF-5 and MOF-5/CSCA-2 (Figure 2.4) show that there is almost no difference. About TG, two steps of weight losses are clearly observed for both, which correspond to the loss of solvent molecules below 200 ^{o}C (~ 22% weight loss) and the decomposition of the host frameworks in the range of 450~530 ^{o}C (~ 40% weight loss), respectively. In addition, their FTIR curves both display the asymmetric

(1504 and 1600 cm^{-1}) and symmetric vibrations (1387 cm^{-1}) of carboxylate groups in BDC. Several bands are detected at 1300~700 cm^{-1}, assigned to the out-of-plane vibrations of BDC.[8]

Table 2.1 Chemical compositions of MOF-5 and MOF-5/CSCA-2 from elemental analysis and ICP.

Samples	C (wt%)	H (wt%)	N (wt%)	Zn (wt%)
MOF-5	39.28	3.34	4.14	24.2
MOF-5/CSCA-2	39.46	3.49	4.28	23.6

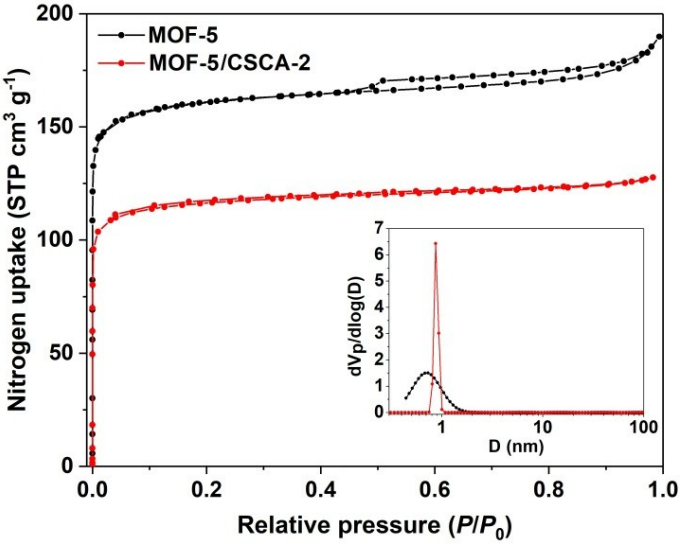

Figure 2.5 N_2 adsorption-desorption isotherms at 77 K and the corresponding NLDFT pore size distributions of MOF-5 and MOF-5/CSCA-2.

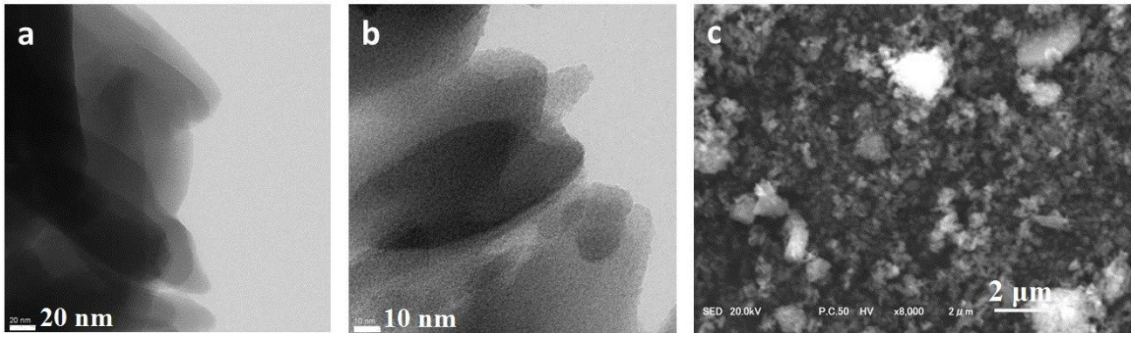

Figure 2.6 (a, b) TEM, and (c) SEM images of MOF-5@CSCA, which was prepared by mixing as-prepared MOF-5 (0.02 g) with CS solution (0.04 mL), followed by drying at 60 ^{o}C.

As for the element contents, it has been found that MOF-5/CSCA-2 owns a little lower content of Zn and higher contents of C, H, and N than those of MOF-5 (Table 2.1). The N_2 adsorption-desorption isotherms (Figure 2.5) indicate a BET surface area of 402 m^2 g^{-1} and a pore volume of 0.20 cm^3 g^{-1} of MOF-5/CSCA-2 composite, which is lower than that of MOF-5 with a BET surface area of 540 m^2 g^{-1} and a pore volume of 0.29 cm^3 g^{-1}, implying that CS is accommodated into the cavities of MOF-5/CSCA-2 framework and occupies the partial tunnels. The pore size distribution of both MOF-5 and MOF-5/CSCA-2 (inset in Figure 2.5) reveals the micropores (< 1 nm). Besides, we also directly mixed MOF-5 with CS solution, called MOF-5@CSCA, which exhibits much eroded textures (Figure 2.6).

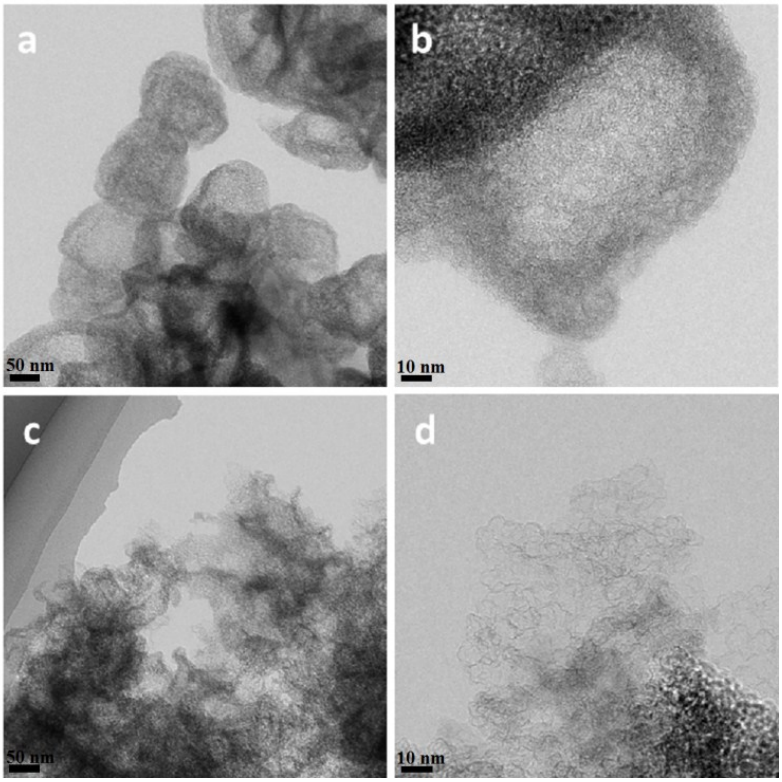

Figure 2.7 TEM images of (a-b) NPC, and (c-d) NPC-2.

NPC and NPC-2 were synthesized through the pyrolysis of MOF-5 and MOF-5/CSCA-2 at 900 ^{o}C in an argon flow, respectively, followed by acid treatment to remove the metal impurities. NPC shows hollow structures (Figure 2.7a and b). NPC-2 displays ordinary carbon morphology, with very thin carbon layers in the edges (Figure 2.7c and d). Introducing CS solution in the preparation process readily tunes the morphology of resultant porous carbons.

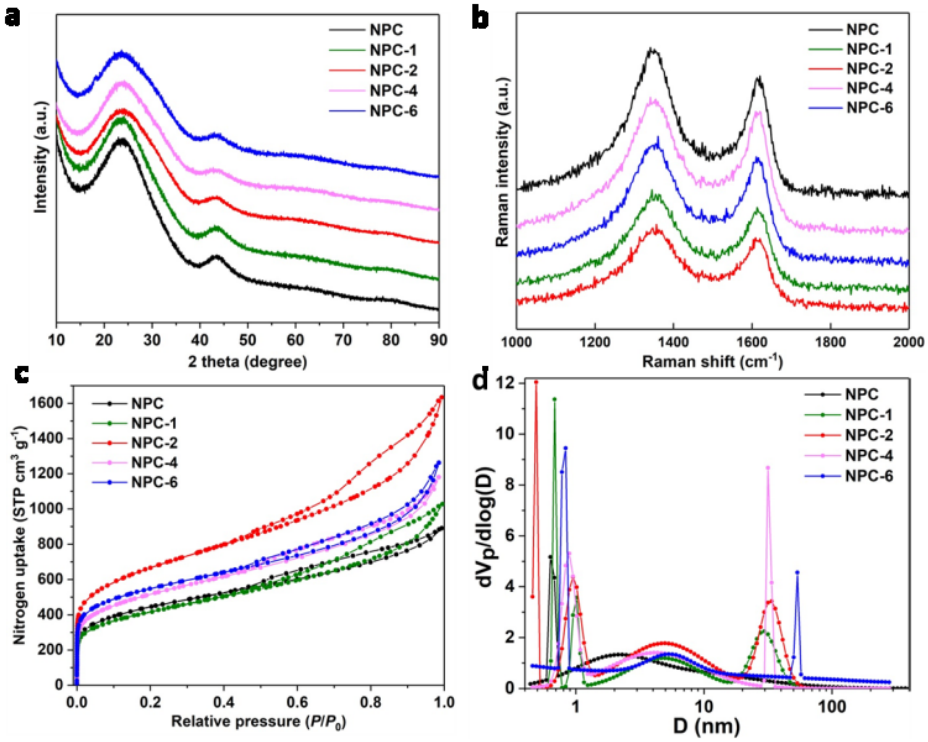

Figure 2.8 (a) Power XRD patterns, (b) Raman spectra, (c) N_2 adsorption-desorption isotherms at 77 K, and (d) the corresponding NLDFT pore size distributions for hierarchically porous carbons.

Table 2.2 BET surface areas (S_{BET}), pore volumes (V_{pore}) and $V_{meso\text{-}macro}/V_{micro}$ for hierarchically porous carbons.

Samples	S_{BET}	V_{pore} ($cm^3\ g^{-1}$)			$V_{meso\text{-}macro}/$
	($m^2\ g^{-1}$)	V_{total}	V_{micro} [a]	$V_{meso\text{-}macro}$ [b]	V_{micro}
NPC	1578	1.37	0.79	0.58	0.73
NPC-1	1476	1.56	0.63	0.93	1.48
NPC-2	2375	2.49	1.01	1.48	1.47
NPC-4	1850	1.83	0.91	0.92	1.01
NPC-6	1797	1.77	0.74	1.03	1.39

[a] Calculated by micropore analysis method (MP method). [b] Calculated by subtracting micropore volume from total pore volume.

The XRD patterns of NPC and NPC-*V* (*V* = 1, 2, 4, and 6) (Figure 2.8a) display amorphous structures with two broad peaks at 2 theta = ~ 24° and ~ 43°, which are assigned to the typical (002) and (101) planes of graphitic carbon, respectively.[7d, 9] Besides, no other diffraction peaks are discovered, indicating the impurities were well removed by acid treatment. Raman spectra (Figure 2.8b) display two typical bands at ~ 1348 cm^{-1} (D band) and ~ 1615 cm^{-1} (G band), ascribed to the disordered carbons and in-plane vibrations of graphitic sp^2 carbons, respectively.[9-10] Commonly, I_D/I_G (the ratio of relative intensity of D to G band) is utilized to evaluate the graphitization degree of carbon materials.[11] For samples of NPC, NPC-1, -2, -4, and -6, the I_D/I_G ratios are calculated to be 1.23, 1.13, 1.10, 1.09, and 1.14, respectively. It reveals that all samples contain graphitic and disordered carbons, meaning the partial graphitization.

The N_2 adsorption-desorption curves at 77 K (Figure 2.8c) of hierarchically porous carbons exhibit type IV isotherms with apparent hysteresis loops in the P/P_0 range from 0.5 to 1, indicating the existence of meso-/macropores. The existence of micropores is also observed in the low relative pressure. It is noteworthy that NPC-2 shows the highest surface area of 2375 $m^2\ g^{-1}$ and the maximum total pore volume of 2.49 $cm^3\ g^{-1}$, while NPC demonstrates the lower surface area of 1578 $m^2\ g^{-1}$ and the smallest total pore volume of 1.37 $cm^3\ g^{-1}$ (Table 2.2). Obviously, in comparison with the pristine NPC with a $V_{meso\text{-}macro}/V_{micro}$ ratio of 0.73, the NPC-2 sample has a much higher $V_{meso\text{-}macro}/V_{micro}$ ratio of 1.47, indicating that the decomposition of chitosan-encapsulating MOF-5 caused more meso-/macropores with a pore size larger than 20 nm (Figure 2.8d). Moreover, the pore size distributions using NLDFT method (Figure 2.8d) confirm the hierarchical pore structure of NPC-2 with both micro (0.5-0.9 nm) and mesopores (2-10 nm, 20-50 nm). Other samples including NPC-1, -4, and -6 also display the similar

hierarchically porous structures with micro- and meso- or macropores (Figure 2.8d). However, NPC only shows peaks in pore size distribution at < 20 nm. It can be seen that the specific surface areas and pore volumes of resultant carbons can be effectively controlled by adding CS solution during the synthesis of precursors. Besides, introducing CS with a suitable amount in the preparation process readily expands the porosity of NPC-2, because that the decomposition of CS molecules within the cavities of host during heating makes a positive contribution to pores.

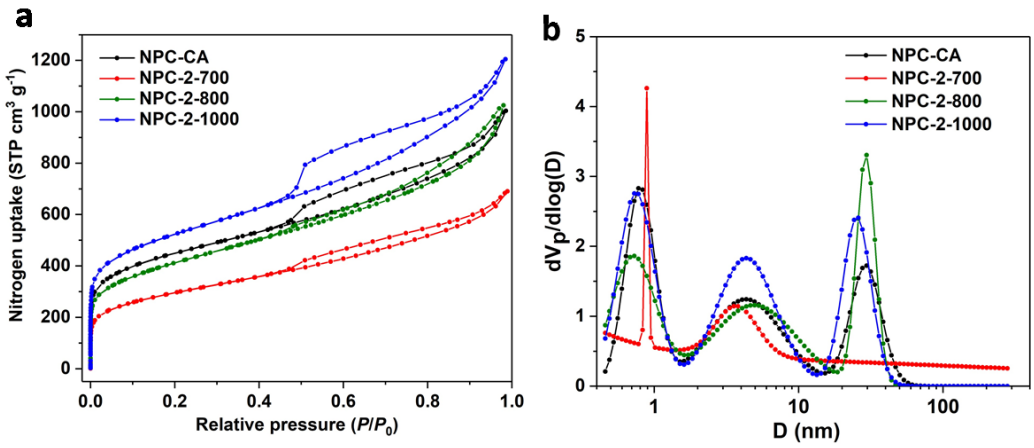

Figure 2.9 (a) N_2 adsorption-desorption isotherms at 77 K, and (b) the corresponding NLDFT pore size distributions for the comparative carbons.

Without the CS additive, NPC-CA displays a very low BET surface area and pore volume (Figure 2.9, Table 2.3), comparable to that of NPC, implying that CS plays an important role to modify the pore structures. Besides, NPC-2-*T*s at various pyrolysis temperatures (*T* = 700, 800, and 1000 ^{o}C) were also synthesized and investigated (Table 2.3). Clearly, NPC-2 at 900 ^{o}C holds the largest values of BET surface area and pore volume, while NPC-2-700 shows the smallest BET surface area (1051 m^2 g^{-1}) and pore volume (1.07 cm^3 g^{-1}). This is because that pyrolysis temperature of 900 ^{o}C is very close

to the boiling point of Zn metal (908 °C),[12] which is favorable for pore expansion in the carbonization procedure of MOF-5/CSCA-2.

Table 2.3 BET surface areas (S_{BET}), pore volumes (V_{pore}) and $V_{meso\text{-}macro}/V_{micro}$ for the comparative carbons.

Samples	S_{BET} ($m^2\ g^{-1}$)	V_{pore} ($cm^3\ g^{-1}$)			$V_{meso\text{-}macro}/V_{micro}$
		V_{total}	V_{micro}[a]	$V_{meso\text{-}macro}$[b]	
NPC-CA	1555	1.55	0.79	0.76	0.96
NPC-2-700	1051	1.07	0.54	0.53	0.98
NPC-2-800	1472	1.58	0.63	0.95	1.51
NPC-2-1000	1848	1.86	0.89	0.97	1.09

[a] Calculated by micropore analysis method (MP method). [b] Calculated by subtracting micropore volume from total pore volume.

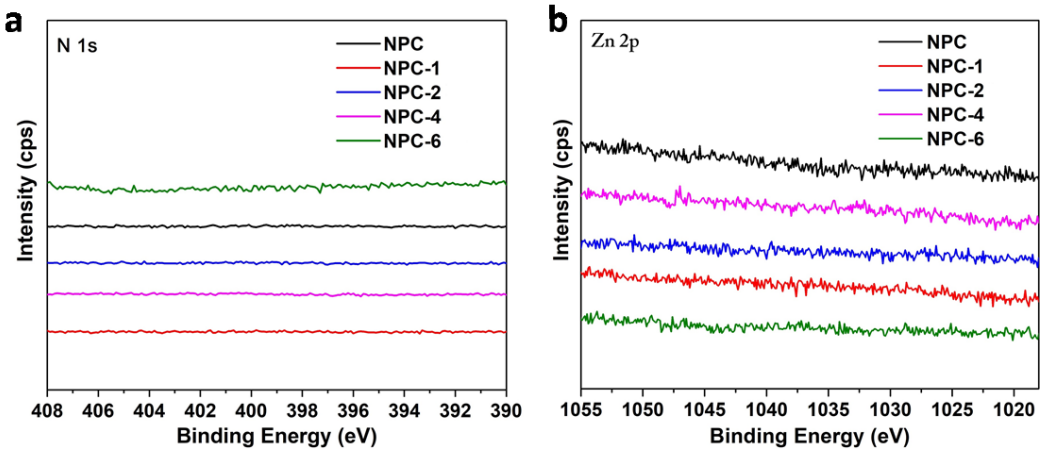

Figure 2.10 XPS spectra of (a) N 1s peak and (b) Zn 2p for the hierarchically porous carbons.

XPS (Figure 2.10a) shows that there is no obvious peak for N 1s, meaning no nitrogen content in the hierarchically porous carbons. This is consistent with the result of elemental analysis (Table 2.4). Figure 2.10b demonstrates no Zn 2p signal, indicating that the residual Zn impurities from the pyrolysis were removed well by hydrochloric acid solution, in agreement with the result of XRD (Figure 2.8a). Besides, the elemental mapping analysis shows the uniform distribution of C and O in NPC-2 (Figure 2.11).

Table 2.4 Chemical compositions of hierarchically porous carbons from elemental analysis.

Samples	C (wt%)	H (wt%)	N (wt%)
NPC	87.26	1.17	-0.22
NPC-1	79.94	1.60	0.34
NPC-2	81.12	1.22	-1.30
NPC-4	80.73	1.98	-0.79
NPC-6	81.0	2.12	-0.82

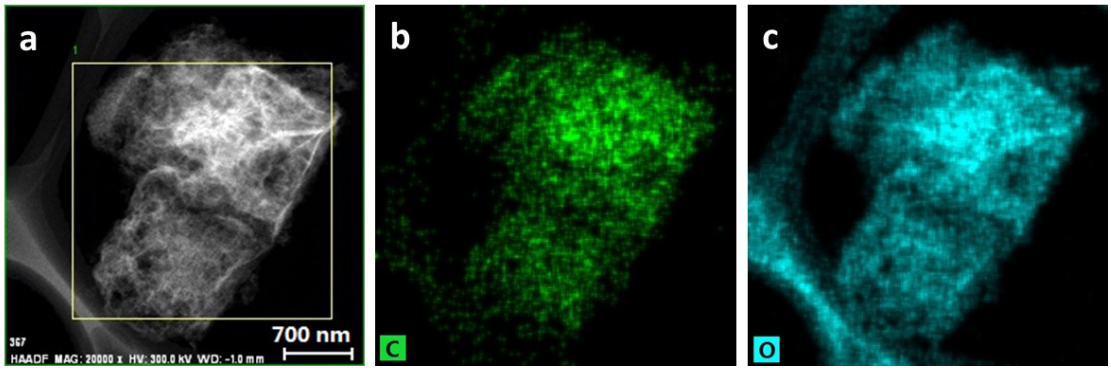

Figure 2.11 (a) HAADF-STEM and the corresponding elemental mapping images of (b) C, (c) O in NPC-2.

2.3.2 Electrochemical measurement

The cyclic voltammogram (CV) and galvanostatic charge/discharge (GC) curves were investigated by adopting a two-electrode symmetrical supercapacitor cell, where 1 M H_2SO_4 solution was used as the electrolyte and there was no reference electrode.

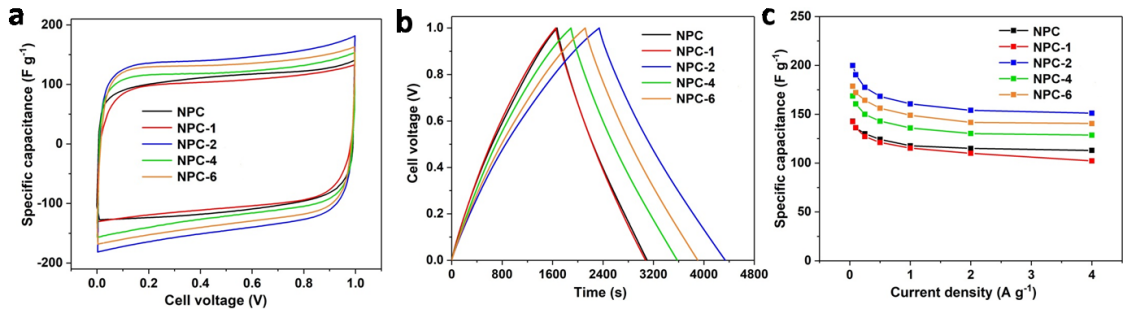

Figure 2.12 Electrochemical performances of hierarchically porous carbons. (a) CV curves at a sweep rate of 50 mV s^{-1}, (b) GC curves at a current density of 0.05 A g^{-1}, and (c) specific capacitance at different current densities.

Table 2.5 Specific capacitances at different current densities for hierarchically porous carbons.

Samples	Specific capacitance (F g^{-1})						
	Current density (A g^{-1})						
	0.05	**0.1**	**0.25**	**0.5**	**1**	**2**	**4**
NPC	142.9	136.2	130.0	124.3	117.7	115	113.0
NPC-1	142.4	136.2	127.1	121.1	115.3	110.0	102.2
NPC-2	199.9	190.4	177.5	168.3	160.6	154.0	151.1
NPC-4	168.6	160.6	149.9	142.9	136.0	130.2	102.2
NPC-6	178.6	172.2	164.2	156.2	148.9	141.6	140.5

The CV curves in Figure 2.12a show nearly rectangular shapes without any redox peaks at a sweep rate of 50 mV s^{-1}, displaying the typical characteristics of EDLCs for

hierarchically porous carbons.[13] Besides, the symmetric profiles of GC curves were observed in Figure 2.12b, indicating the good electrochemically capacitive properties. It is noted that the specific capacitance of NPC-2 is as high as 199.9 F g^{-1} at a current density of 0.05 A g^{-1}, owing to its highest specific surface area and appropriate hierarchical micro-/mesopores with abundant mesopores, which are very favourable for supplying facile transport channels for electrolytes into the pores, promoting the quick charge transfer and reducing the distance of ion transport.[14] Additionally, NPC-2 holds the relatively high degree of graphitization among the five carbon samples, resulting in the enhanced electrical conductivity and thus improving the supercapacitor performance.[15]

For comparison, NPC-1, -4, and -6 demonstrate the lower specific capacitance under the current density of 0.05 A g^{-1}, corresponding to the values of 142.4, 168.6, and 178.6 F g^{-1}, respectively (Figure 2.12c and Table 2.5). What's more, NPC with lower specific surface area shows a quite small specific capacitance (142.9 F g^{-1} at 0.05 A g^{-1}).

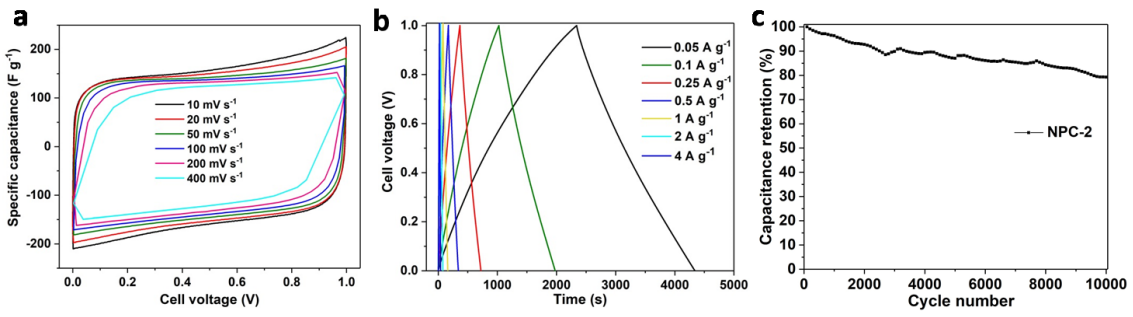

Figure 2.13 Electrochemical performances of NPC-2. (a) CV curves at different sweep rates (10~400 mV s^{-1}), (b) GC curves at different current densities (0.05~4 A g^{-1}), and (c) cycling stability at a current density of 2 A g^{-1}.

Figure 2.13a illustrates the detailed CV curves of NPC-2 in different sweep rates. Notably, even under the high sweep rate of 400 mV s^{-1}, the shape of rectangular is still well maintained, meaning its superb electrochemical capability. Moreover, Figure 2.13b shows that NPC-2 displays a specific capacitance of 151.1 F g^{-1} at a current density of 4 A g^{-1}, corresponding to a high retention of 75.6% when the current density increased from 0.05 to 4 A g^{-1}. This result demonstrates the good rate capability of NPC-2, which is mainly ascribed to its hierarchically porous structures. Because of the high specific surface area, pore volume and hierarchically porous structures, NPC-2 exhibits a high specific capacitance and the excellent rate performance in the aqueous electrolyte with a symmetric cell, which are comparable to those reported carbon materials under the similar test conditions, such as carbon nanorods derived from MOF-74-Rod (187 F g^{-1} at 0.05 A g^{-1}),[7d] hierarchically porous carbon film *via* calcination of HKUST-1/CNT (157.9 F g^{-1} at 1 A g^{-1}),[16] yet smaller than that of N- and S- codoped carbon nanocapsules derived from TU@MIL-101-NH_2 composite (272 F g^{-1} at 0.1 A g^{-1}).[6c]

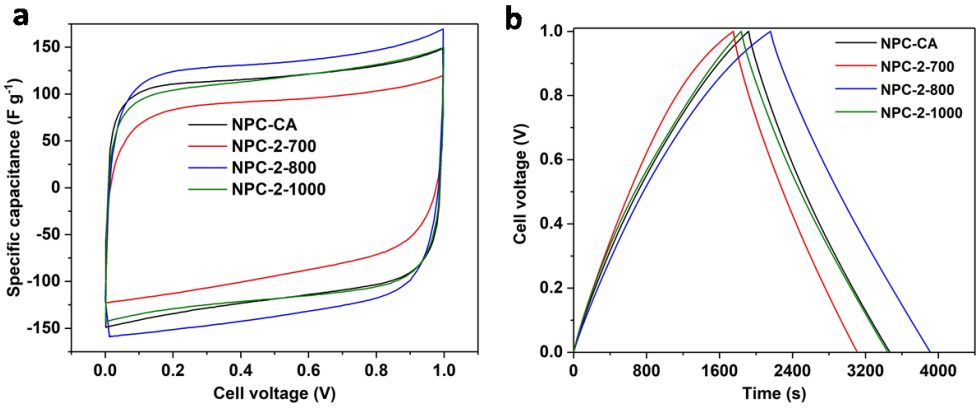

Figure 2.14 Electrochemical performances of the comparative carbons. (a) Cyclic voltammetrical curves at a sweep rate of 50 mV s^{-1}, (b) galvanostatic charge-discharge curves at a current density of 0.05 A g^{-1}.

Table 2.6 Specific capacitances at different densities for the comparative carbons.

Samples	Specific capacitance (F g^{-1})						
	Current density (A g^{-1})						
	0.05	**0.1**	**0.25**	**0.5**	**1**	**2**	**4**
NPC-CA	155.0	149.5	141.2	134.1	128.9	122.1	120.8
NPC-2-700	135.8	129.2	119.5	111.8	104.7	97.1	95.0
NPC-2-800	175.2	169.3	160.3	152.9	146.4	141.2	136.3
NPC-2-1000	160.8	153.7	143.4	135.2	128.1	122.0	118.6

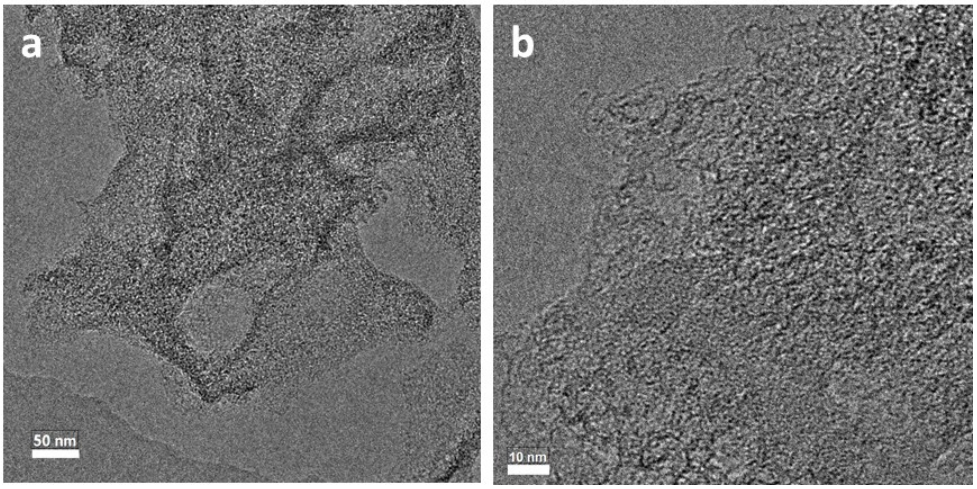

Figure 2.15 TEM images of (a-b) NPC-2 after cycle test.

Furthermore, we also studied the electrochemical behaviours of some comparative samples, which show lower specific capacitances than that of NPC-2 (Figure 2.14 and Table 2.6). Especially, NPC-CA possesses the very low specific capacitance (155 F g^{-1} at 0.05 A g^{-1}), implying that CA has no effects on the capacitive property. To some extent, chitosan is utilized as the pore structure-directing agent, which has a positive effect on the surface area and pore volume in resultant carbon, leading to a fast transport of ions. Moreover, NPC-2-700, -800, and -1000 were also studied as supercapacitor electrodes. From the results in Table 2.6, we found that the temperature of 900 ^{o}C is the

most proper to obtain the excellent electrochemical performance of NPC-2. In addition, the outstanding cycling performance was observed for NPC-2, with a capacitance loss of 21% after 10 000 cycles at a current density of 2 A g^{-1} (Figure 2.13c). Additionally, no significant changes of NPC-2 morphologies are observed after cycle test (Figure 2.15).

In short, NPC-2 not only shows the highest specific capacitance, but also excellent cycling stability and good rate performance, ascribed to the high specific surface area, pore volume, and the unique hierarchically porous architecture with more mesopores within the carbon networks, which have an advantage for fast ion diffusion and accessibility.[17]

2.4 Conclusion

In summary, we have developed a facile and general method to fabricate the hierarchically porous carbons (ranging from micro- to macropores) from the pyrolysis of MOF-5/chitosan composites at 900 ^{o}C for the first time, where chitosan is considered as pore structure-directing agent. With the optimization of conditions, the resultant carbon of NPC-2 exhibited the high specific surface area of 2375 m^2 g^{-1} and high pore volumes of 2.49 cm^3 g^{-1}, compared to the pristine carbon of NPC without the CS additive. As electrodes for EDLCs, hierarchically porous carbon NPC-2 demonstrated the best capacitive behaviour with a specific capacitance of 199.9 F g^{-1} in 1 M H_2SO_4 electrolyte, excellent rate capability of 75.6% from 0.05 A g^{-1} to 4 A g^{-1}, and superior cycling performance in a symmetric cell. We ascribed the excellent supercapacitor properties of NPC-2 to its high specific surface area, large pore volume, and hierarchical pore structures especially with abundant mesopores.

References

[1] a) J. R. Miller, P. Simon, *Science* **2008**, *321*, 651-652; b) M. Winter, R. J. Brodd, *Chem. Rev.* **2004**, *104*, 4245-4270; c) G. Wang, L. Zhang, J. Zhang, *Chem. Soc. Rev.* **2012**, *41*, 797-828; d) E. Frackowiak, F. Beguin, *Carbon* **2001**, *39*, 937-950; e) Y. Shao, M. F. El-Kady, J. Sun, Y. Li, Q. Zhang, M. Zhu, H. Wang, B. Dunn, R. B. Kaner, *Chem. Rev.* **2018**, *118*, 9233-9280; f) C. Tang, Z. Pu, Q. Liu, A. M. Asiri, X. Sun, Y. Luo, Y. He, *ChemElectroChem* **2015**, *2*, 1903-1907; g) Z. Xing, Q. Chu, X. Ren, C. Ge, A. H. Qusti, A. M. Asiri, A. O. Al-Youbi, X. Sun, *J. Power Sources* **2014**, *245*, 463-467.

[2] a) B. Liu, H. Shioyama, T. Akita, Q. Xu, *J. Am. Chem. Soc.* **2008**, *130*, 5390-5391; b) D. Sheberla, J. C. Bachman, J. S. Elias, C. J. Sun, Y. Shao-Horn, M. Dincă, *Nat. Mater.* **2017**, *16*, 220-224; c) R. R. Salunkhe, J. Tang, N. Kobayashi, J. Kim, Y. Ide, S. Tominaka, J. H. Kim, Y. Yamauchi, *Chem. Sci.* **2016**, *7*, 5704-5713; d) W. Xia, C. Qu, Z. Liang, B. Zhao, S. Dai, B. Qiu, Y. Jiao, Q. Zhang, X. Huang, W. Guo, *Nano Lett.* **2017**, *17*, 2788-2795; e) T. Deng, W. Zhang, O. Arcelus, D. Wang, X. Y. Shi, X. Y. Zhang, J. Carrasco, T. Rojo, W. T. Zheng, *Commun. Chem.* **2018**, *1*, 6; f) J. Guo, D. Wu, T. Wang, Y. Ma, *Appl. Surf. Sci.* **2019**, *475*, 56-66; g) H. Jiang, X. Ye, Y. Zhu, L. Wang, P. Zhao, Z. Yue, J. Xie, Z. Wan, C. Jia, *Appl. Surf. Sci.* **2019**, *470*, 573-580.

[3] a) L. L. Zhang, X. Zhao, *Chem. Soc. Rev.* **2009**, *38*, 2520-2531; b) E. Frackowiak, *Phys. Chem. Chem. Phys.* **2007**, *9*, 1774-1785; c) J. K. Sun, Q. Xu, *Energy Environ. Sci.* **2014**, *7*, 2071-2100; d) L. Zhou, Z. C. Zhuang, H. H. Zhao, M. T. Lin, D. Y. Zhao, L. Q. Mai, *Adv. Mater.* **2017**, *29*, 1602914; e) W. Xia, A. Mahmood, R. Zou, Q. Xu, *Energy Environ. Sci.* **2015**, *8*, 1837-1866.

[4] a) J. W. F. To, Z. Chen, H. B. Yao, J. J. He, K. Kim, H. H. Chou, L. Pan, J. Wilcox, Y. Cui, Z. N. Bao, *ACS Cent. Sci.* **2015**, *1*, 68-76; b) Y. W. Zhu, S. Murali, M. D. Stoller, K. Ganesh, W. Cai, P. J. Ferreira, A. Pirkle, R. M. Wallace, K. A. Cychosz, M. Thommes, *Science* **2011**, *332*, 1537-1541; c) E. Raymundo-Piñero, M. Cadek, F. Béguin, *Adv. Funct. Mater.* **2009**, *19*, 1032-1039; d) Z. S. Wu, A. Winter, L. Chen, Y. Sun, A. Turchanin, X. Feng, K. Müllen, *Adv. Mater.* **2012**, *24*, 5130-5135.

[5] a) F. Qi, Z. Xia, R. Sun, X. Sun, X. Xu, W. Wei, S. Wang, G. Sun, *J. Mater. Chem. A* **2018**, *6*, 14170-14177; b) J. Gamby, P. Taberna, P. Simon, J. Fauvarque, M. Chesneau, *J. Power Sources* **2001**, *101*, 109-116; c) K. Xia, Q. Gao, J. Jiang, J. Hu, *Carbon* **2008**, *46*, 1718-1726.

[6] a) M. Zhi, F. Yang, F. Meng, M. Li, A. Manivannan, N. Wu, *ACS Sustainable Chem. Eng.* **2014**, *2*, 1592-1598; b) D. W. Wang, F. Li, M. Liu, G. Q. Lu, H. M. Cheng, *Angew. Chem. Int. Ed.* **2008**, *120*, 379-382; c) Q. L. Zhu, P. Pachfule, P. Strubel, Z. Li, R. Zou, Z. Liu, S. Kaskel, Q. Xu, *Energy Storage Mater.* **2018**, *13*, 72-79; d) B. Z. Fang, J. H. Kim, M. S. Kim, A. Bonakdarpour, A. Lam, D. P. Wilkinson, J. S. Yu, *J. Mater. Chem.* **2012**, *22*, 19031-19038.

[7] a) P. Zhang, F. Sun, Z. H. Xiang, Z. G. Shen, J. Yun, D. P. Cao, *Energy Environ. Sci.* **2014**, *7*, 442-450; b) R. R. Salunkhe, Y. V. Kaneti, J. Kim, J. H. Kim, Y. Yamauchi, *Acc. Chem. Res.* **2016**, *49*, 2796-2806; c) C. C. Hou, Q. Xu, *Adv. Energy Mater.* **2018**, 1801307; d) P. Pachfule, D. Shinde, M. Majumder, Q. Xu, *Nat. Chem.* **2016**, *8*, 718-724; e) S. Dang, Q. L. Zhu, Q. Xu, *Nat. Rev. Mater.* **2017**, *3*, 17075; f) H. L. Wang, Q. L. Zhu, R. Q. Zou, Q. Xu, *Chem* **2017**, *2*, 52-80; g) T. Y. Ma, S. Dai, M. Jaroniec, S. Z. Qiao, *J. Am. Chem. Soc.* **2014**, *136*, 13925-13931; h) K. Shen, X. Chen, J. Chen, Y. W. Li, *ACS Catal.* **2016**, *6*, 5887-5903.

[8] a) C. Petit, T. J. Bandosz, *Adv. Funct. Mater.* **2010**, *20*, 111-118; b) L. M. Huang, H. T. Wang, J. X. Chen, Z. B. Wang, J. Y. Sun, D. Y. Zhao, Y. S. Yan, *Microporous Mesoporous Mater.* **2003**, *58*, 105-114.

[9] S. Zhong, C. X. Zhan, D. P. Cao, *Carbon* **2015**, *85*, 51-59.

[10] J. W. Jeon, R. Sharma, P. Meduri, B. W. Arey, H. T. Schaef, J. L. Lutkenhaus, J. P. Lemmon, P. K. Thallapally, M. I. Nandasiri, B. P. McGrail, *ACS Appl. Mater. Interfaces* **2014**, *6*, 7214-7222.

[11] A. C. Ferrari, J. Meyer, V. Scardaci, C. Casiraghi, M. Lazzeri, F. Mauri, S. Piscanec, D. Jiang, K. Novoselov, S. Roth, *Phys. Rev. Lett.* **2006**, *97*, 187401.

[12] S. J. Yang, T. Kim, J. H. Im, Y. S. Kim, K. Lee, H. Jung, C. R. Park, *Chem. Mater.* **2012**, *24*, 464-470.

[13] P. Simon, Y. Gogotsi, *Nat. Mater.* **2008**, *7*, 845-854.

[14] a) Y. Li, Z. Li, P. K. Shen, *Adv. Mater.* **2013**, *25*, 2474-2480; b) J. Hou, C. Cao, F. Idrees, X. Ma, *ACS Nano* **2015**, *9*, 2556-2564.

[15] Z. Li, Z. Xu, X. Tan, H. Wang, C. M. Holt, T. Stephenson, B. C. Olsen, D. Mitlin, *Energy Environ. Sci.* **2013**, *6*, 871-878.

[16] Y. Liu, G. Li, Y. Guo, Y. Ying, X. Peng, *ACS Appl. Mater. Interfaces* **2017**, *9*, 14043-14050.

[17] Y. B. Huang, P. Pachfule, J. K. Sun, Q. Xu, *J. Mater. Chem. A* **2016**, *4*, 4273-4279.

Chapter 3

Immobilizing Palladium Nanoparticles on Boron-Oxygen-Functionalized Carbon Nanospheres towards Efficient Hydrogen Generation from Formic Acid

Carbon nanospheres (XC-72R) were functionalized by boron-oxygen (B-O) through coannealing with boric acid, to which highly dispersed palladium nanoparticles (Pd NPs) (~ 1.7 nm) were immobilized by a wet chemical reduction for the first time. The resultant Pd/OB-C catalyst exhibits significantly improved activity for the dehydrogenation from formic acid (FA) compared to pristine XC-72R supported Pd NPs (Pd/C). Impressively, by adding melamine precursor, the B-O and nitrogen (N)-functionalized product OB-C-N displays an extremely high B content, ca. 34 times higher than OB-C. The Pd/OB-C-N catalyst with an ultrafine Pd particle size of ~ 1.4 nm shows a superb activity, with a turnover frequency (TOF) as high as 5354 h^{-1} at 323 K, owing to the uniform ultrafine Pd NPs and the effect from B-O and N functionalities.

3.1 Introduction

Nowadays, in order to avoid excessive consumption of fossil fuels, clean hydrogen-powered society has become an ultimate target for human beings. Particularly, as a promising energy-related strategy, hydrogen fuel cells have received considerable attention in many fields, such as vehicle system and portable power supply, owing to its pollution-free emissions with high conversion efficiency.[1] Recently, more and more efforts have been made to study liquid chemical hydrides as hydrogen carriers.[2] For

example, formic acid (FA), which has a high hydrogen content of 4.4 wt.%, shows a lot of advantages, including excellent stability, non-toxicity, and simple storage and transport.[3] Generally, FA has two pathways of decomposition as shown in Equations (3.1) and (3.2) in the presence of a catalyst.[4]

$$HCOOH \rightarrow H_2 + CO_2 \qquad (3.1)$$

$$HCOOH \rightarrow H_2O + CO \qquad (3.2)$$

Pathway (3.2) should be avoided, because the catalyst deactivation could occur and CO is also toxic to fuel cell catalysts. Numerous studies have demonstrated that palladium (Pd) possesses excellent catalytic properties for the dehydrogenation from FA.[5] Besides, carbon-based materials are often utilized as the support to immobilize Pd NPs, owing to their superb mechanical and chemical stability.[6] Compared to the pristine carbon, heteroatom functionalization, like N, not only endows the carbon with a lot of active sites, but also generates unique electronic properties by tailoring the electron-donor in carbon.[7] Yet, until now research works on study of NPs immobilized on B-functionalized carbons for FA dehydrogenation still remains a challenge.

In this study, boron-oxygen (B-O)-functionalized carbon nanospheres (OB-C) were fabricated via a one-step coannealing process. For the first time, Pd NPs (~ 1.7 nm) were successfully immobilized on OB-C by a wet chemical reduction, which demonstrated a greatly improved performance for the complete hydrogen generation from FA, in comparison with Pd NPs supported on unmodified XC-72R (Pd/C). OB-C has proved to be an excellent support to anchor ultrafine Pd NPs because of the B-O functionalities. Interestingly, by adding melamine into the precursor mixture of XC-72R and boric acid, the resultant OB-C-N reveals a B content as high as 12.4 wt.%. As a

result, Pd/OB-C-N demonstrates an ultrafine Pd particle size and outstanding catalytic activity for FA dehydrogenation.

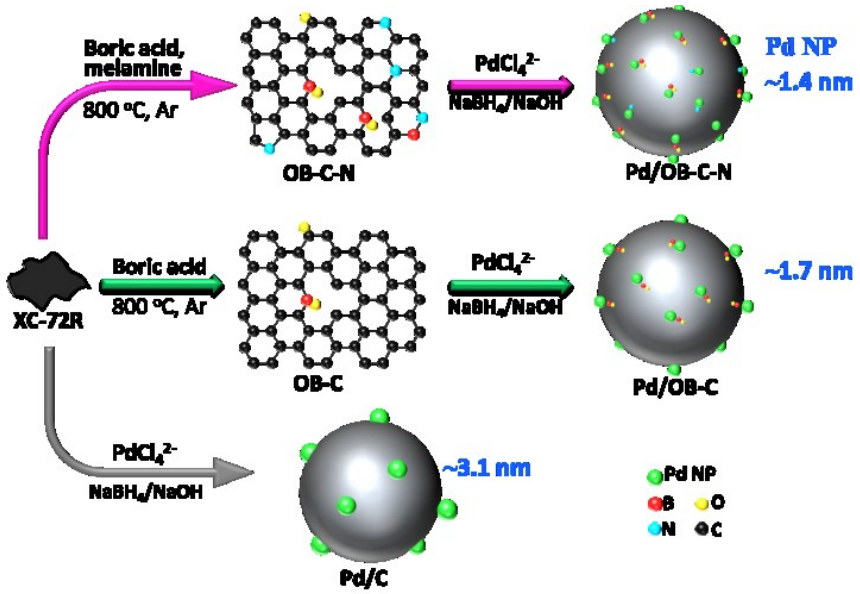

Figure 3.1 Schematic illustration of the syntheses of Pd NPs immobilized on functionalized carbon nanospheres.

The syntheses of functionalized carbon nanoshperes and immobilization of Pd NPs on them are illustrated in Figure 3.1. OB-C was prepared by a facile coannealing of XC-72R and boric acid in an argon flow at 800 ^{o}C, followed by treatment using water. By employing different boric acid amounts, OB-Cs were prepared, denoted as OB-C1, OB-C2, and OB-C3. Remarkably, by adding melamine precursor, B-O and N-functionalized carbon nanospheres (OB-C-N) were synthesized, displaying a much higher B content than that of OB-C. By altering the amounts of melamine while keeping the boric acid amount unchanged, OB-C-Ns (OB-C-N1, OB-C-N2, and OB-C-N3) were prepared. The Pd/OB-C and Pd/OB-C-N catalysts were prepared by a typical wet chemical impregnation and reduction process using $NaBH_4$ as the reducing agent. This sodium

hydroxide (NaOH)-assisted reduction approach is favorable to acquire the well-dispersed ultrafine Pd NPs on carbon nanospheres.[8]

3.2 Experimental section

3.2.1 Materials

All chemicals were commercially available and used without further purification. Formic acid (FA, HCOOH, Kishida Chemical Co., Ltd., > 98%), sodium formate (SF, HCOONa, Kishida Chemical Co., Ltd., > 98%), Vulcan XC-72R (Carbon, Cabot Corp., USA), melamine monomer ($C_3H_6N_6$, Tokyo Chemical Industry Co., Ltd., > 98.0%), boric acid (H_3BO_3, Wako Pure Chemical Industries, ≥ 99.5%), potassium tetrachloropalladate (K_2PdCl_4, Wako Pure Chemical Industries, > 97%), sodium hydroxide (NaOH, Wako Pure Chemical Industries, > 93%), and sodium borohyride ($NaBH_4$, Tokyo Chemical Industry Co., Ltd., > 95%) were used as received. De-ionized (DI) water with a specific resistance of > 18.0 MΩ·cm was used in all experiments.

3.2.2 Characterization and instrumentation

The powder X-ray diffraction (XRD) measurements were executed on a Rigaku Ultima IV X-ray diffractometer with a Cu Kα source. X-ray photoelectron spectroscopic (XPS) measurements were conducted on a Shimadzu ESCA-3400 X-ray photoelectron spectrometer using a Mg Kα source. The XPS spectra has been calibrated by carbon (284.6 eV). The N_2 adsorption/desorption isotherms were measured using automatic volumetric adsorption instrument (BELSORP-max) at 77 K. The surface areas were calculated using Brunauer-Emmett-Teller (BET) method. Elemental analyses were carried out on Perkinelmer 2400II instruments. The Pd and B contents were measured by inductively coupled plasma optical emission spectroscopy (ICP-OES) on the Varian

Vista-MPX. Transmission electron microscopic (TEM) and high-annular dark-field scanning TEM (HAADF-STEM) pictures were recorded on TECNAI G^2 F20 machine with operating voltage at 200 kV equipped with energy-dispersive X-ray detector (EDX). Electron energy loss spectroscopic (EELS) element mapping and spectrum were obtained on a Titan3 G2 60-300 (FEI) with a Super-X EDX system (Bruker) and imaging filter (Quantum, GATAN) under operating voltage of 300 kV. The gas generated from the catalytic reaction was collected after purging the reactor with argon at least three times, which was tested by GC-8A (molecular sieve 5A, Ar as carrier gas) and GC-8A (Porapack N, He as carrier gas) analyzers (Shimadzu). Raman scattering spectra were obtained from a laser Raman microscope system (Nanophoton RAMANtouch) with an excitation wavelength of 532 nm. Fourier transform infrared spectroscopy (FTIR) analyses were performed on Shimadzu IRTracer-100 using ATR mode.

3.2.3 Syntheses of samples

1) Syntheses of OB-C

Typically, 0.2 g of Vulcan XC-72R carbon and 0.5 g of boric acid were mixed and ground in a mortar for ~ 15 minutes. The mixture was then transferred to a ceramic crucible and heated in a tube furnace at 800 ^{o}C for 2 h in an argon flow, followed by cooling down to room temperature (rt). The raw product was subsequently soaked in DI water for 24 h under stirring. The final product, denoted as OB-C1, was obtained via centrifugation, washed with plenty of DI water, and then dried at 60 ^{o}C. Besides, by altering the amount of boric acid to 0.3 g and 0.7 g, respectively, OB-C2 and OB-C3 were also prepared using the same procedure as that of OB-C1.

2) Syntheses of OB-C-N

Typically, 0.2 g of XC-72R, 0.7 g of melamine monomer, and 0.5 g of boric acid were mixed and ground in a mortar for ~ 15 minutes. The consequent preparation processes are the same as that of OB-C1. The resultant carbon product is called OB-C-N1. Besides, by altering the amount of melamine to 0.5 g and 1.0 g, respectively, OB-C-N2 and OB-C-N3 were also synthesized using the same procedure as that of OB-C-N1. Similarly, OB-C-N1-*T* samples (*T* represents the annealing temperature of 700, 900 or 1000 ^{o}C) were also prepared.

3) Syntheses of Pd nanocatalysts

The above carbons were used as the supports to immobilize Pd NPs by a traditional wet chemical impregnation and reduction. Typically, 100 mg of OB-C-N1 was dispersed in 5 mL of DI water under stirring at rt. Then, an aqueous solution of K_2PdCl_4 (0.1 M, 0.6 mL) was added and the mixture was subsequently stirring for 1 h. 30 mg of fresh $NaBH_4$ dissolved in 1 mL of 2.0 M NaOH solution was introduced into the above solution, followed by stirring for 2 h. Finally, the catalyst Pd/OB-C-N1 was centrifuged, washed with DI water for 3 times, and dried under vacuum at rt.

3.2.4 Catalytic activity characterization

1) Procedure for the hydrogen generation of formic acid

Reaction apparatus for testing the H_2/CO_2 evolution from the FA/SF system is the same as the previously reported. Commonly, a mixture including the as-prepared nanocatalyst and DI water (~ 1.0 mL) was placed in a two-necked round-bottom flask (30 mL), which was placed in a water bath with a preset temperature of 30, 40, 50, and 60 ^{o}C. A

gas burette filled with water was connected to the reaction flask to determine the volume of released gas with temperature kept at 298 K during the measurements. The reaction started when the FA/SF solution with various molar ratios (1 mL) was injected into the mixture. Through recording the displacement of water in the gas burette, the volume of the released gas was monitored. The molar ratios of metal Pd to FA were theoretically fixed at 0.02 for the catalytic reactions unless otherwise noted.

2) Durability test of Pd/OB-C-N

For testing the durability of the as-synthesized Pd/OB-C-N1, the catalyst was recollected by centrifugation after finishing the decomposition of FA and washed with DI water for 3 times. For the next cycle, 1 mL of FA (3.0 M) and SF (7.5 M) was injected into the flask. Such cycling processes for FA dehydrogenation were performed for 5 runs at 50 ^{o}C.

3) Calculation methods

The turnover frequency (TOF) is based on the metal amount (Pd atoms) in the catalyst, which is calculated from the equation as follow:

$$TOF = \frac{PV}{(RT) * 2n_{\mathrm{Pd}}t}$$

where P is the atmospheric pressure (101325 Pa), V is the final released gas volume of (H_2 + CO_2), R is the universal gas constant (8.3145 m^3 Pa mol^{-1} K^{-1}), T is the room temperature (298 K), n_{Pd} is the total mole number of Pd atoms in the catalyst, and t is the completion time of the reaction in hour.

3.3 Results and discussion

3.3.1 Characterization of OB-C and Pd/OB-C

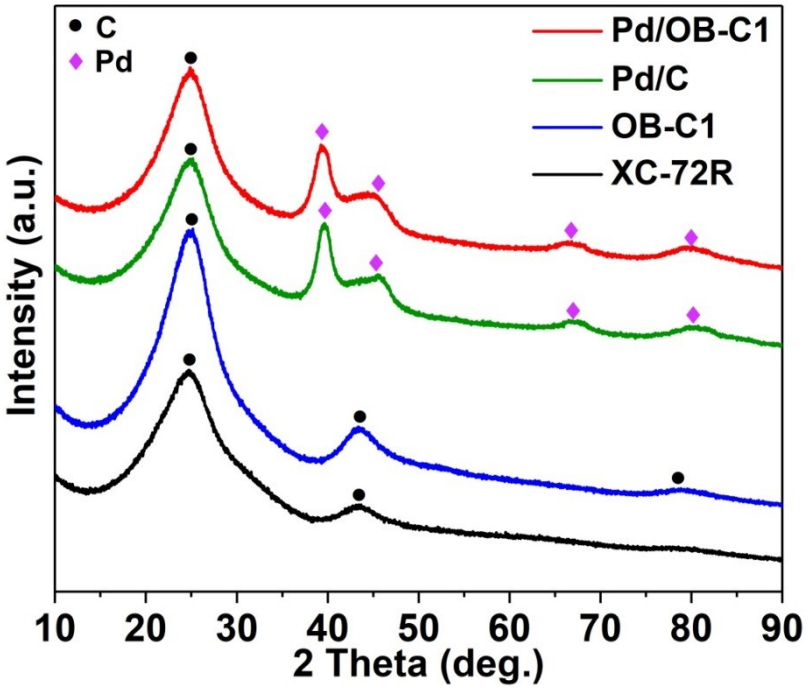

Figure 3.2 XRD patterns of Pd/OB-C1, Pd/C, XC-72R, and OB-C1.

X-ray diffraction (XRD) patterns of XC-72R and OB-C1 both show two characteristic peaks of carbon at 2θ ≈ 25.4 (002) and 43.0° (101) (Figure 3.2). For OB-C1, a weak peak at 2θ ≈ 79° is observed, assigned to (110) of carbon.[9] The typical XRD peaks of metallic Pd are clearly observed at 2θ ≈ 39.8 (111), 46.0 (200), 66.5 (220), and 81.0° (311) for as-prepared Pd/C and Pd/OB-C1 (Figure 3.2), in good agreement with the JCPDS 46-1043 file.[7c]

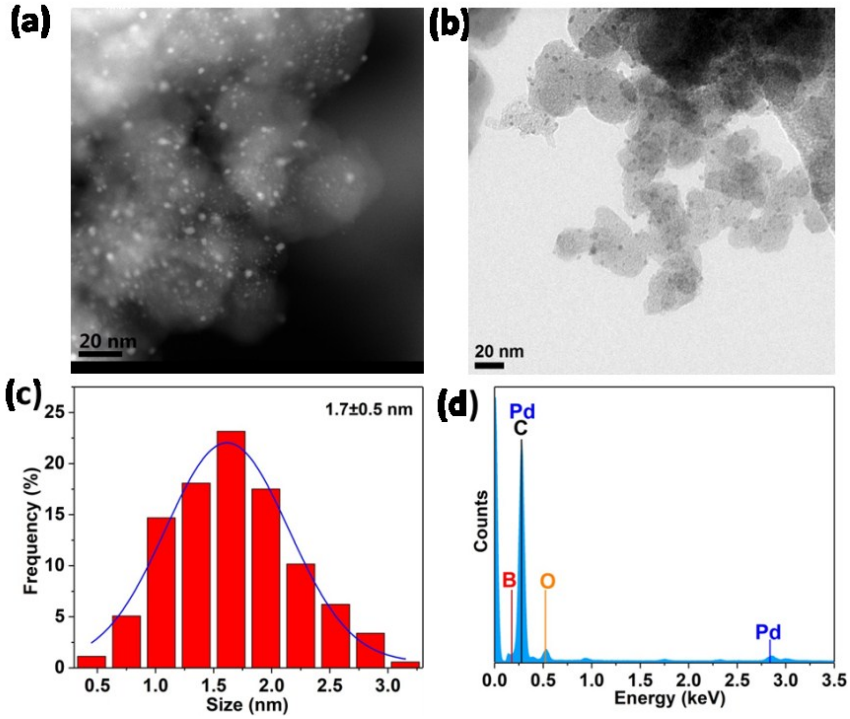

Figure 3.3 (a) HAADF-STEM and (b) TEM images, (c) corresponding Pd particle size distribution, and (d) EDX spectrum of the as-prepared Pd/OB-C1 catalyst.

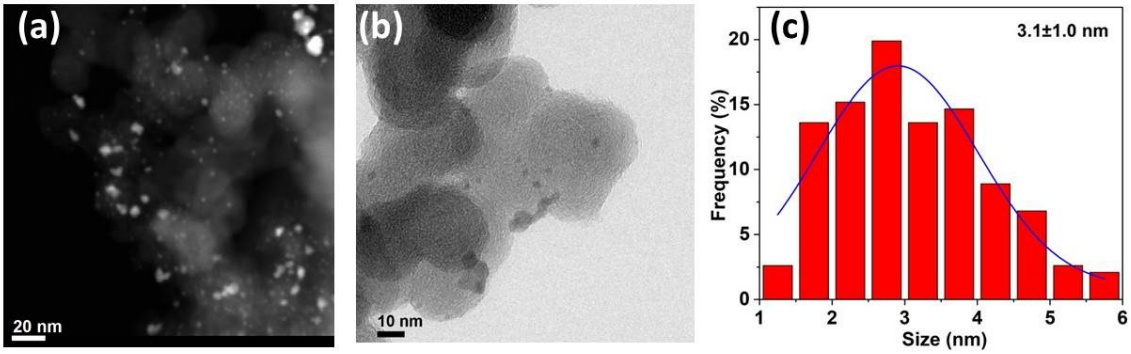

Figure 3.4 (a) HAADF-STEM and (b) TEM images, and (c) corresponding Pd particle size distribution of the as-prepared Pd/C catalyst.

The morphologies of Pd/C and Pd/OB-C1 were characterized by the transmission electron microscopy (TEM) and high-angle annular dark-field scanning TEM (HAADF-STEM). The Pd NPs are well distributed on OB-C1 with a small Pd particle size (~ 1.7 nm) (Figure 3.3a-c), while Pd NPs roughly disperse on pristine XC-72R with aggregation in a large particle size of ~ 3.1 nm (Figure 3.4). The energy-dispersive X-ray (EDX) spectrum proves the coexistence of B and metallic Pd in the Pd/OB-C1 (Figure 3.3d). The contents of B and Pd were further measured by inductively coupled plasma-optical emission spectroscopy (ICP-OES), which are determined to be 0.25 and 5.6 wt.%, respectively (Table 3.1). Obviously, even if OB-C1 has a low content of B, it could still capture the $PdCl_4^{2-}$ precursor and control the growth of Pd NPs, leading to a small Pd particle size and uniform dispersion, due to the strong interaction between B species and Pd NPs.

Table 3.1 ICP (Pd and B) analyses for the samples.

Samples	Pd content (wt%)	B content (wt%)
OB-C1	-	0.35
Pd/C	5.8	0.027
Pd/OB-C1	5.6	0.25

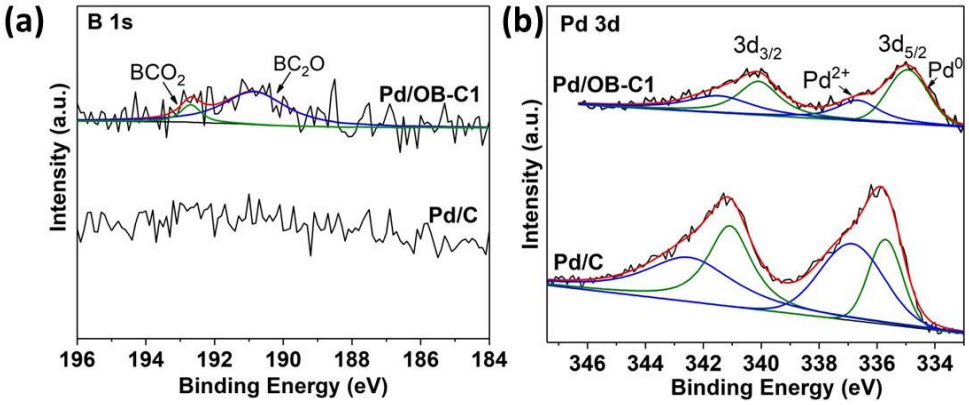

Figure 3.5 XPS spectra of (a) B 1s and (b) Pd 3d of Pd/OB-C1 and Pd/C.

$$H_3BO_3 \rightarrow HBO_2 + H_2O \quad (3.3)$$

$$4HBO_2 \rightarrow H_2B_4O_7 + H_2O \quad (3.4)$$

$$H_2B_4O_7 \rightarrow 2B_2O_3 + H_2O \quad (3.5)$$

$$xB_2O_3 + yC \rightarrow mO_2BC/OBC_2 + nCO \quad (3.6)$$

The chemical states of elements (B and Pd) of the samples were investigated by X-ray photoelectron spectroscopy (XPS). Pd/OB-C1 shows a broad B 1s peak (Figure 3.5a), implying a low content of B, which is consistent with ICP result in Table 3.1. It is worth noting that all the B atoms are connected to C and O atoms in the forms of BCO_2 (192.4 eV) and BC_2O (190.7 eV).[10] During the annealing, boric acid firstly undergoes dehydration to produce boron oxide and subsequently reacts with XC-72R to form B-O-functionalized carbon nanospheres as shown in Equations (3.3)-(3.6).[11] No boron is detected over Pd/C catalyst (Figure 3.5a), in accordance with the ICP result of negligible B content (0.027 wt.% for B), indicating B could not be incorporated in XC-72R during the reduction using $NaBH_4$. In high-resolution Pd 3d spectrum over Pd/OB-C1 (Figure 3.5b), doublets of Pd $3d_{5/2}$ and Pd $3d_{3/2}$ are clearly observed and

deconvoluted into four peaks, which correspond to metallic Pd^0 (340.1 and 334.7 eV) and Pd^{2+} (342.2 and 336.5 eV). The Pd^{2+} is probably caused by oxidation on the surface of the catalyst in air.[7d] A noticeable binding energy shift for Pd is observed on Pd/OB-C1 as compared to Pd/C (Figure 3.5b), because of the charge transfer caused by B doping.[7f]

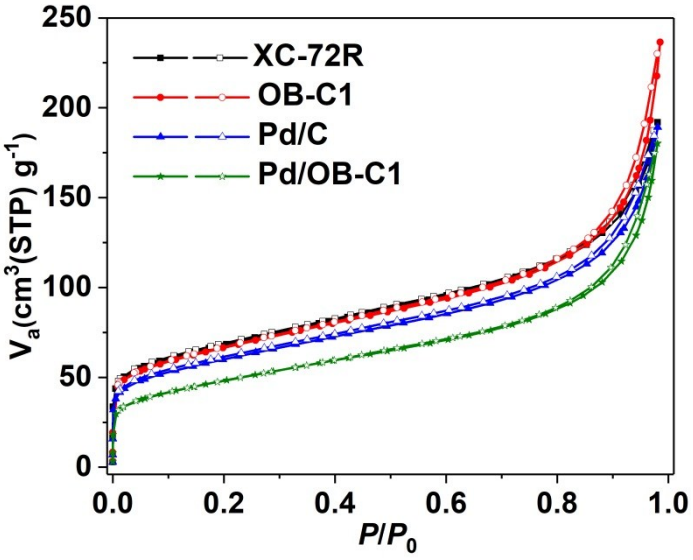

Figure 3.6 N_2 sorption isotherms of the as-prepared samples at 77 K.

Table 3.2 BET surface areas and pore volumes of the prepared samples.

Samples	S_{BET} ($m^2 \cdot g^{-1}$)	Pore volume ($cm^3 \cdot g^{-1}$)
XC-72R	240	0.297
OB-C1	235	0.366
Pd/C	213	0.293
Pd/OB-C1	171	0.279

N_2 sorption measurements were used to gain more information about the samples. The Brunauer-Emmett-Teller (BET) surface areas of XC-72R, OB-C1, Pd/C, and Pd/OB-C1 are 240, 235, 213, and 171 $m^2 \cdot g^{-1}$, respectively (Figure 3.6 and Table 3.2). Compared to OB-C1, the Pd/OB-C1 catalyst shows a decreased surface area and pore volume, displaying that some Pd NPs are dispersed in the pores of the support.

3.3.2 Catalytic activity of Pd/OB-C

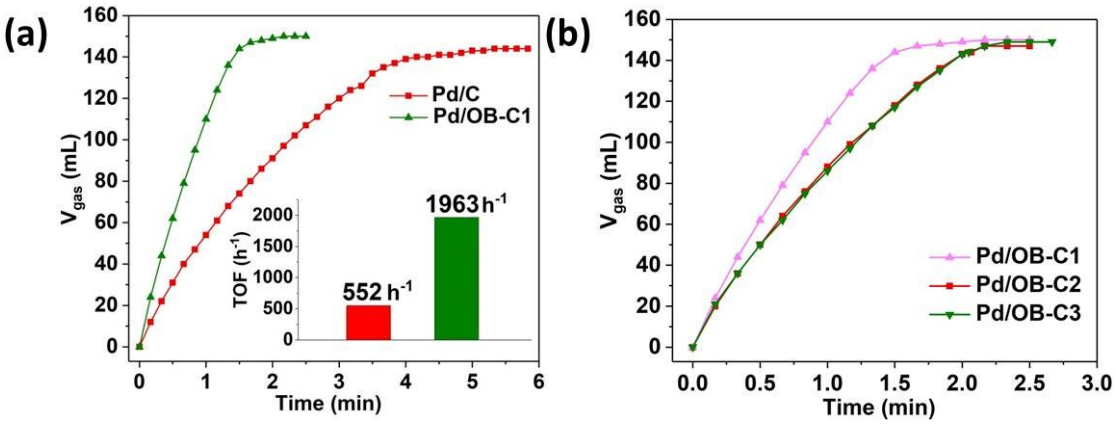

Figure 3.7 Volume of the generated gas (H_2 + CO_2) *versus* time for the hydrogen generation from the aqueous FA-SF solution (n_{FA}: n_{SF} = 1:2.5; FA, 3 mmol; n_{Pd}/n_{FA} = 0.02) at 323 K over the catalysts of (a) Pd/OB-C1 and Pd/C, and (b) Pd/OB-C1, Pd/OB-C2, and Pd/OB-C3. Inset of (a): the TOF values of the dehydrogenation of FA over the catalysts.

The as-prepared catalysts were applied for dehydrogenation of FA. Remarkably, compared to Pd/C, the Pd/OB-C1 catalyst demonstrates a significantly enhanced catalytic performance, generating the gas (H_2 and CO_2) of 144 mL within 1.5 min at 323 K in a FA/SF (sodium formate) system (n_{Pd}/n_{FA} = 0.02, n_{FA}:n_{SF} = 1:2.5) (Figure 3.7a).

The corresponding turnover frequency (TOF) value is 1963 h^{-1} at 323 K on the basis of total metal amount employed in the catalyst (Figure 3.7a, inset), which is ca. 2.6 times higher than that of Pd/C under the same condition. The result illustrates the positive effect of B-O functionality of the carbon nanosphere support on the catalytic activity. Comparative catalysts, Pd/OB-C2 and Pd/OB-C3, were synthesized for FA dehydrogenation, showing that Pd/OB-C1 is the best catalyst (Figure 3.7b).

3.3.3 Characterization of OB-C-N and Pd/OB-C-N

Table 3.3 ICP (Pd and B) and elemental analyses (N) for the samples.

Samples	Pd content (wt%)	B content (wt%)	N content (wt%)
OB-C-N1	-	12.4	14.12
Pd/OB-C-N1	6.6	9.3	10.13

Melamine was introduced into the precursor mixture of XC-72R and boric acid, of which the annealing gave the product OB-C-N1. Surprisingly, ICP analysis indicates a B content as high as 12.4 wt.% in OB-C-N1 (Table 3.3), which is ca. 34 times higher than OB-C1. Elemental analysis also exhibits a N content as high as 14.12 wt.% (Table 3.3). Adding melamine into the precursor mixture could effectively incorporate more B atoms into the carbon framework, probably owing to the powerful interaction between the decomposition products and carbon nanoshperes during the heat treatment. The possible explanation is that because B atoms have larger atomic radius than that of C, it is difficult to dope B into C framework; yet, introducing N with smaller atomic radius than that of C could counteract the lattice stress caused by B.[12]

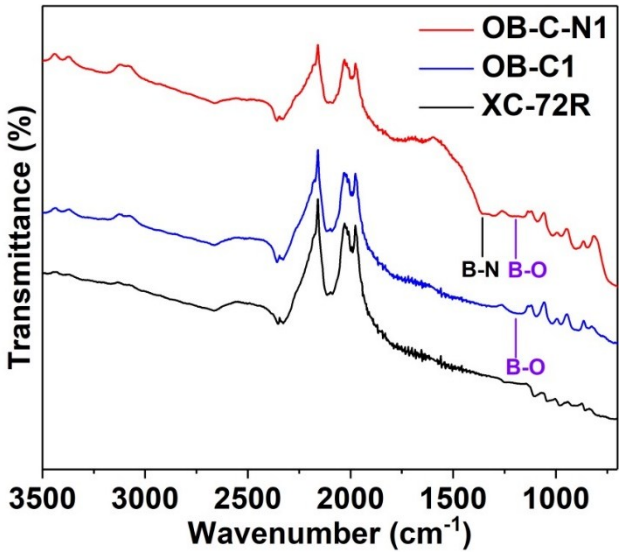

Figure 3.8 FTIR spectra of OB-C-N1, OB-C1, and XC-72R samples.

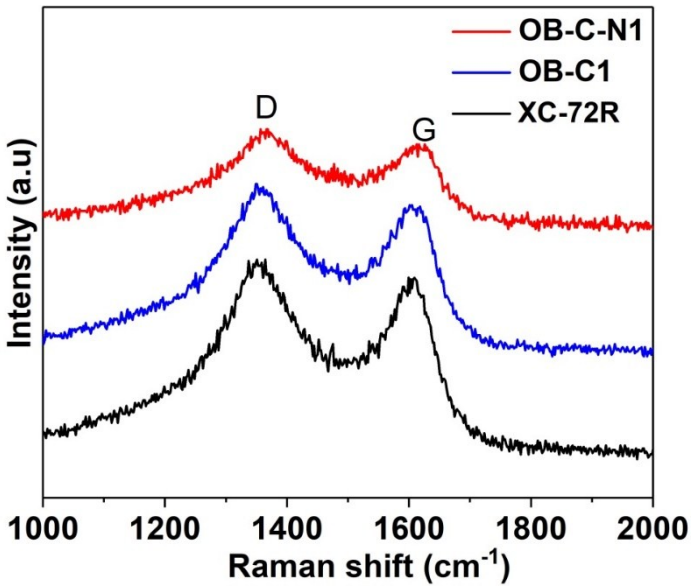

Figure 3.9 Raman spectra of OB-C-N1, OB-C1, and XC-72R samples.

Fourier transform infrared spectroscopy (FTIR) analysis was performed to investigate the chemical environment of the samples (Figure 3.8). Broad peaks located at ~ 1300 and ~ 1360 cm^{-1} could be observed only for OB-C-N1, which are ascribed to the C-N and in-plane B-N-C stretching vibrations, respectively.[13] Additionally, the band centered

at ~ 1200 cm^{-1} both found in OB-C1 and OB-C-N1 corresponds to in-plane B-O-H bending vibration, indicating the existence of B-O species.[11a] The bands at 1088 and 1760 cm^{-1} are due to the vibrations of C-O and C=O, respectively.[14] The band centered at 1647 cm^{-1} demonstrates the C=C stretching.[15] Strong bands in the range of 2100 ~ 2000 cm^{-1} are probably due to C-C triple bonds or cumulative double bonds.[16]

Besides, Raman spectra (Figure 3.9) reveal two typical bands at ~ 1350 cm^{-1} (D band) and ~ 1607 cm^{-1} (G band) for all three samples.[17] The intensity ratio of the D band and G band (I_D/I_G) can evaluate the graphitization degree of carbon materials. For XC-72R, OB-C1 and OB-C-N1, the I_D/I_G ratios are 1.09, 1.11, and 1.17, implying more defects or disorders in OB-C-N1 caused by a higher level of B-O and N doping.[18]

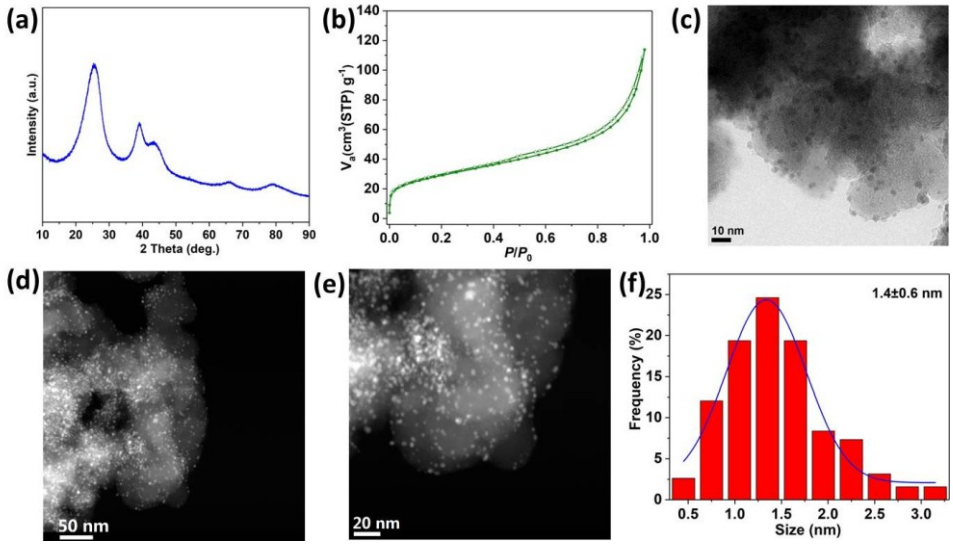

Figure 3.10 (a) XRD pattern, (b) N_2 sorption isotherm (77 K), (c) TEM and (d-e) HAADF-STEM images, and (f) corresponding Pd particle size distribution of as-prepared Pd/OB-C-N1.

Pd NPs were successfully immobilized on OB-C-N1 using the same method as that of Pd/OB-C1. There is no significant difference in XRD patterns between Pd/OB-C-N1 and Pd/OB-C1 (Figure 3.10a). According to the N_2 sorption isotherms (Figure 3.10b), the BET surface area and pore volume of Pd/OB-C-N1 is 104 $m^2 \cdot g^{-1}$ and 0.176 $cm^3 \cdot g^{-1}$, respectively, which is smaller than those of Pd/OB-C1. From TEM and HAADF-STEM, it is clearly observed that Pd NPs are highly dispersed on OB-C-N1, with an ultrafine particle size of ~ 1.4 nm (Figure 3.10c-f).

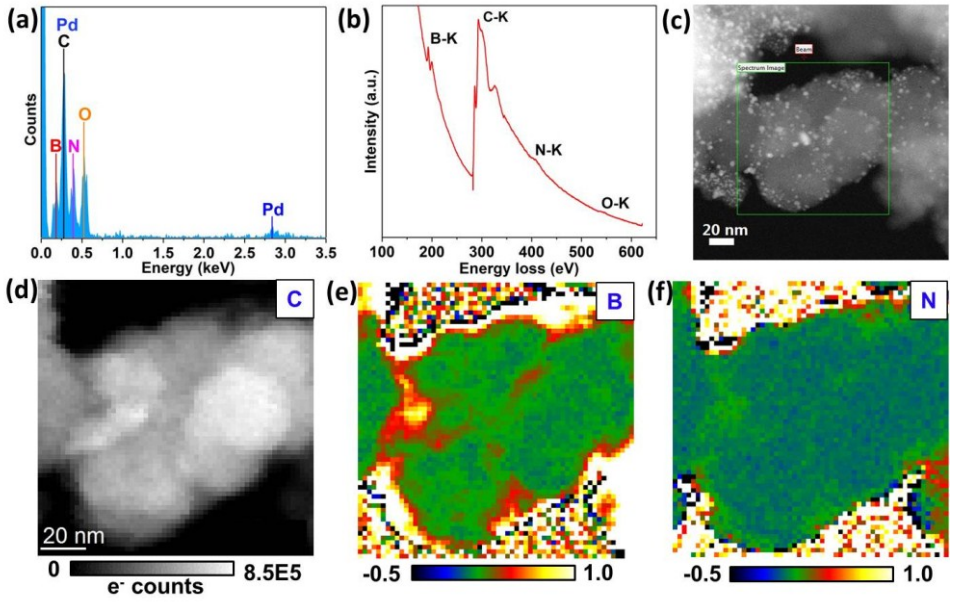

Figure 3.11 (a) EDX and (b) EELS spectra, (c) HAADF-STEM and corresponding EELS mapping images for (d) C, (e) B, (f) N elements of as-prepared Pd/OB-C-N1. The scale bars in d-f are the same.

The EDX analysis strongly proves the coexistence of Pd, C, B, N and O elements (Figure 3.11a). Electron energy loss spectroscopic (EELS) mapping shows uniform distributions of C, B, and N elements in Pd/OB-C-N1 (Figure 3.11b-f). Impressively,

Pd/OB-C-N1 owns a very high content of B (9.3 wt.%) (Table 3.3), which is ca. 36 times higher than that of Pd/OB-C1. XPS spectra of C 1s, B 1s, N 1s, and Pd 3d are presented in Figure 3.12a-d. Notably, Pd/OB-C-N1 demonstrates a lot of B-O and N species, in the forms of O-B-C (BCO_2 and BC_2O) and N-C (pyridinc-, pyrrolic-, and graphitic-N).

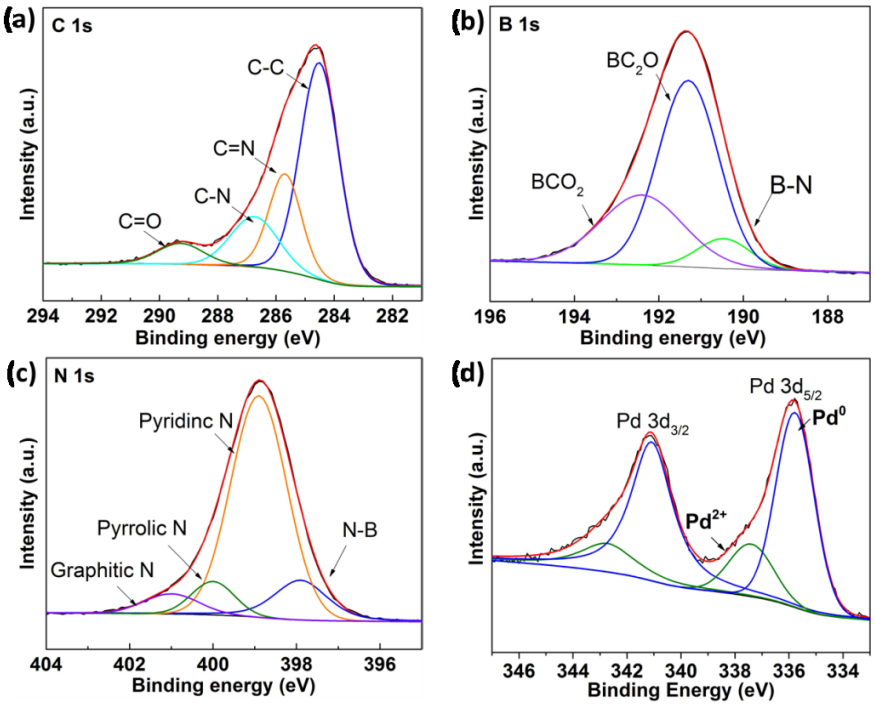

Figure 3.12 XPS spectra of (a) C 1s, (b) B 1s, (c) N 1s, and (d) Pd 3d of as-prepared Pd/OB-C-N1.

3.3.4 Catalytic activity of Pd/OB-C-N

Awesomely, the Pd/OB-C-N1 catalyst demonstrates an outstanding catalytic performance, generating the gas (H_2 and CO_2) of 144 mL within 0.55 min at 323 K (n_{Pd}/n_{FA} = 0.02, n_{FA}:n_{SF} = 1:2.5) in a FA/SF system (Figure 3.13). The corresponding TOF value is as high as 5354 h^{-1} at 323 K (Figure 3.13, inset), which is much higher than those of Pd/OB-C1 and Pd/C, among the best catalysts reported thus far for FA dehydrogenation under the similar condition (Table 3.4). The excess volume of gas, over the theoretical value of 144 mL from FA decomposition, is due to the decomposition of SF in this system (Figure 3.14).

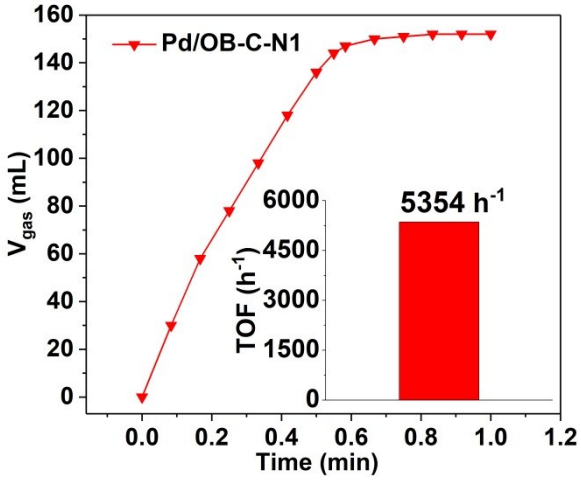

Figure 3.13 Volume of the generated gas (H_2 + CO_2) *versus* time for the hydrogen generation from the aqueous FA-SF solution over Pd/OB-C-N1 at 323 K (n_{FA}: n_{SF} = 1:2.5; FA, 3 mmol; n_{Pd}/n_{FA} = 0.02).

Table 3.4 Catalytic activities for dehydrogenation of FA catalyzed by different heterogeneous catalysts.

Catalyst	Temp. (K)	Additive	TOF (h^{-1})	Ea ($kJ \cdot mol^{-1}$)	Ref.
Pd/N-MSC-30-two-175	303	HCOONa	1803 [b]	43.7	7d
$(Co_6)Ag_{0.1}Pd_{0.9}$/rGO	323	HCOONa	2739 [b]	43.1	3e
Pd/C_m	323	HCOONa	4452 [a]	39.6	5d
Pd/MSC-30	323	HCOONa	2623 [b]	38.6	8
$(Co_3)_EAu_{0.6}Pd_{0.4}$/rGO	323	HCOONa	4840 [b]	39.77	5c
Pd/PDA-rGO	323	HCOONa	3810 [b]	54.3	6b
Pd-B/C	303	HCOONa	1184 [a]	-	19
$Pd/CN_{0.25}$	298	None	5530 [c] 752 [a]	48.8	20
$Pd_{0.6}Ag_{0.4}@ZrO_2$/C/rGO	323	HCOONa	2700 [a]	50.1	5a
Pd/OB-C-N1	303 313 323 333	HCOONa	**1803** **2804** **5354** **7067**	39.86	**This work**

[a] Initial TOF values calculated on initial time for FA dehydrogenation on the basis of metal atoms.
[b] TOF values calculated on the complete time for FA dehydrogenation on the basis of metal atoms.
[c] Initial TOF values calculated on initial time for FA dehydrogenation on the basis of surface metal sites.

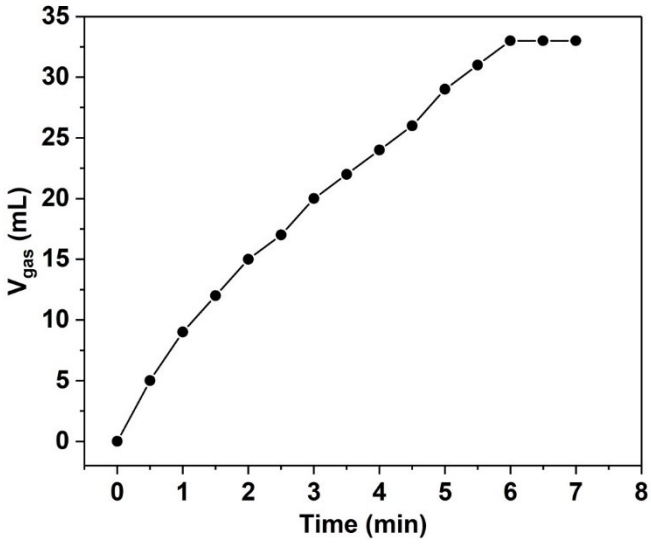

Figure 3.14 Volume of the generated gas *versus* time from aqueous SF solution (7.5 M, 1 mL) over the as-prepared Pd/OB-C-N1 catalyst at 323 K.

Gas chromatography (GC) analyses confirm the existence of H_2 and CO_2 in released gas and no CO impurity was detected at the level of detection limit of 10 ppm (Figure 3.15).

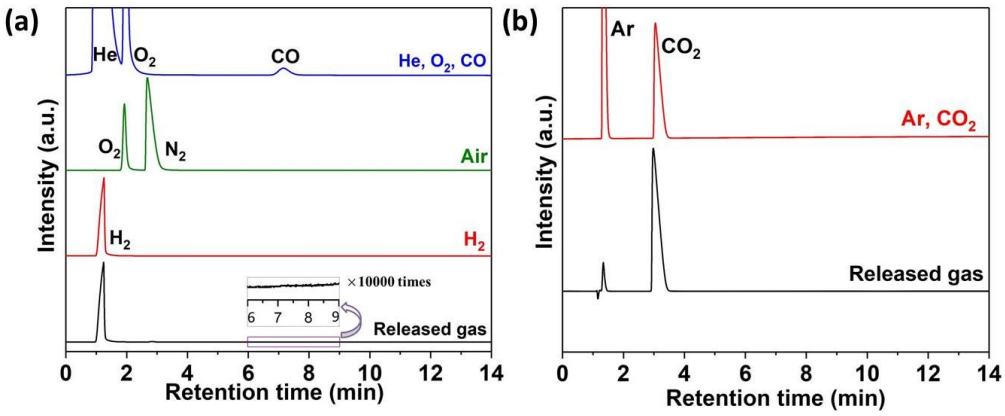

Figure 3.15 Gas chromatograms of (a) CO, air and H_2 as reference gases, (b) CO_2 as reference gas, and the released gas from FA decomposition over the as-prepared Pd/OB-C-N1 catalyst (n_{Pd}/n_{FA} = 0.02) at 323 K.

Comparative catalysts, Pd/OB-C-N2, Pd/OB-C-N3, and Pd/OB-C-N1-*T* (*T* = 700, 900, and 1000 °C) were synthesized for FA dehydrogenation, exhibiting that Pd/OB-C-N1-800 is the best catalyst (Figure 3.16).

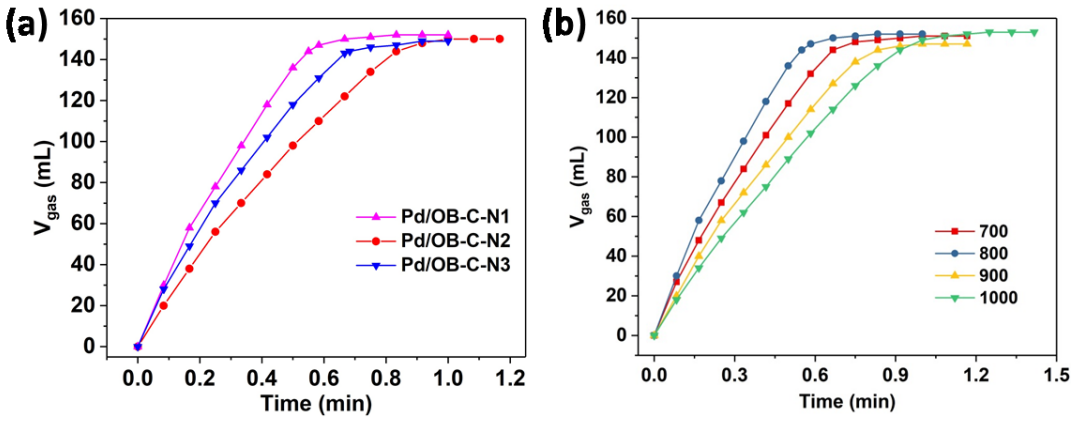

Figure 3.16 Volume of the generated gas (CO_2 + H_2) *versus* time for the hydrogen generation from the aqueous FA-SF solution (n_{FA}: n_{SF} = 1:2.5; FA, 3 mmol; n_{Pd}/n_{FA} = 0.02) at 323 K over (a) Pd/OB-C-N1, Pd/OB-C-N2, Pd/OB-C-N3, and (b) Pd/OB-C-N1-*T* (*T* = 700, 800, 900, and 1000 °C, standing for the annealing temperature for preparation of functionalized carbons).

The time-dependent H_2 generation at various reaction temperatures over Pd/OB-C-N1 in FA/SF system was recorded (Figure 3.17a). The hydrogen is completely released within 0.42, 1.05, and 1.63 min at 333, 313, and 303 K (n_{Pd}/n_{FA} = 0.02, n_{FA}:n_{SF} = 1:2.5), respectively, corresponding to TOFs of 7067, 2804, and 1803 h^{-1}. The Arrhenius plot (Figure 3.17b) gives an activation energy (E_a) of 39.86 kJ·mol^{-1}, which is comparable to other heterogeneous catalysts in similar conditions (Table 3.4). This means that Pd/OB-C-N1 as an effective catalyst can convert FA into CO-free H_2 even at moderate temperature.

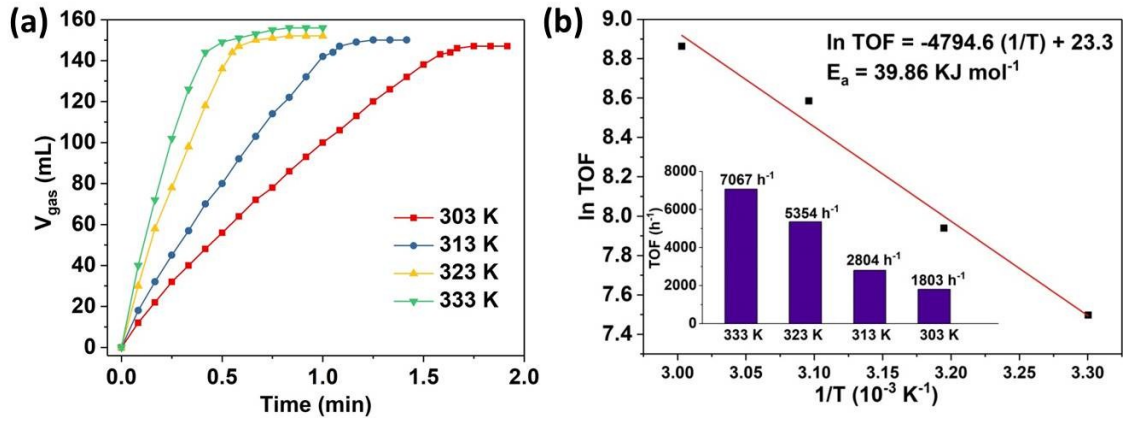

Figure 3.17 (a) Volume of the released gas (H_2 + CO_2) *versus* time for the hydrogen generation from the aqueous FA-SF solution at different temperatures over Pd/OB-C-N1 catalyst (n_{FA}:n_{SF} = 1:2.5; FA, 3 mmol; n_{Pd}/n_{FA}= 0.02) and (b) Arrhenius plot (ln TOF *vs.* 1/*T*) and TOF values (Inset of (b)) over Pd/OB-C-N1catalyst.

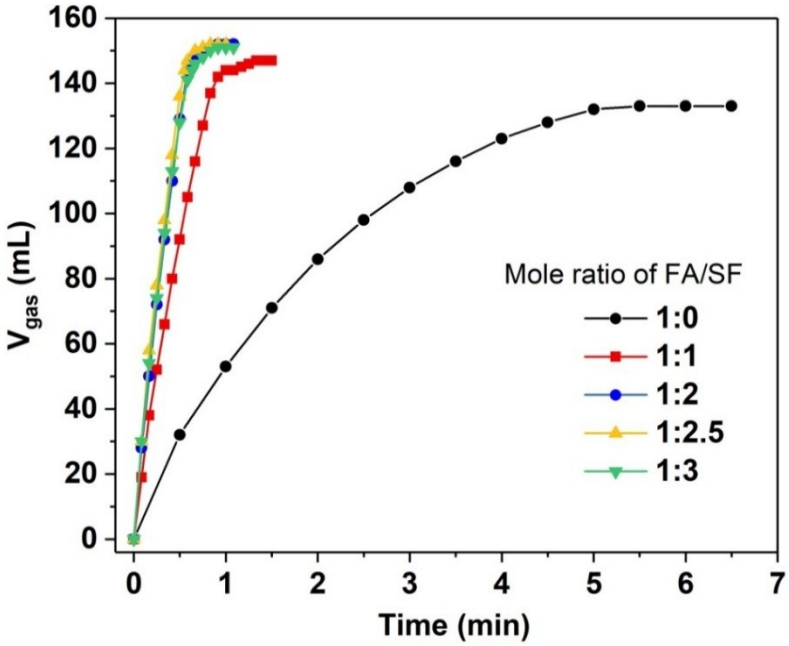

Figure 3.18 Volume of the generated gas (CO_2 + H_2) *versus* time for the hydrogen generation from the aqueous FA-SF solution with different FA/SF mole ratios over the as-prepared Pd/OB-C-N1 catalyst (FA = 3 mmol; n_{Pd}/n_{FA} = 0.02) at 323 K.

We also examined the influence of SF concentrations on the performance for FA dehydrogenation (Figure 3.18). It is found that the catalytic activity was improved with increasing the SF molar percentage in the FA-SF solution until it reached the molar percentage of 71.4%. Then, further increasing the molar percentage of SF had no extra positive contribution to the FA decomposition.

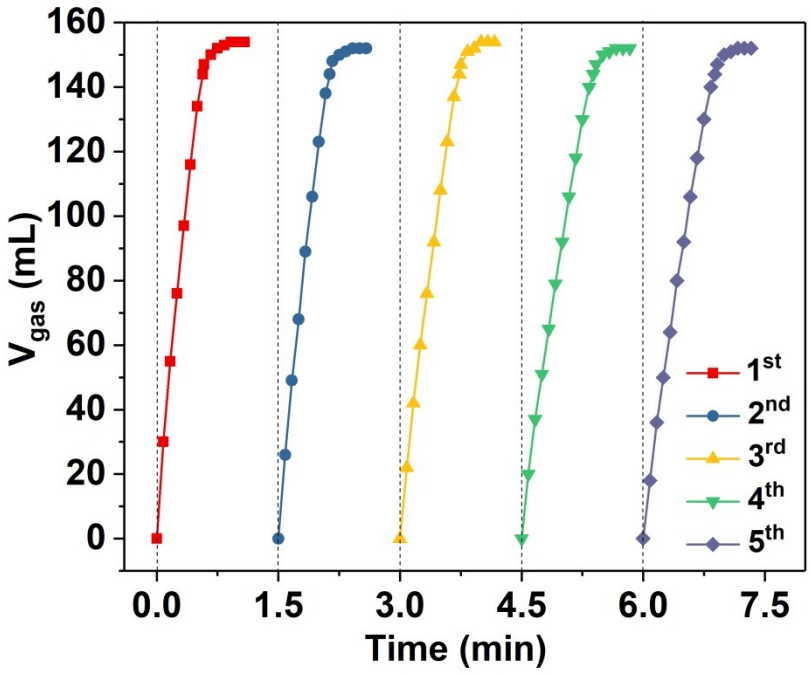

Figure 3.19 Durability test for the hydrogen generation from the aqueous FA-SF solution over the as-prepared Pd/OB-C-N1 catalyst at 323 K (n_{FA}:n_{SF} = 1:2.5; FA, 3 mmol per cycle; n_{Pd}/n_{FA} = 0.02).

Durability or recyclability of a catalyst plays a crucial role in practical applications. After completing the FA decomposition at 323 K in each cycle, the Pd/OB-C-N1 catalyst was centrifuged and washed with water. No apparent loss in catalytic activity was found over 5 runs, indicating the good recyclability (Figure 3.19). The catalyst after

5 runs was characterized by XRD, XPS, and STEM. The XRD pattern shows that the structure of Pd is well preserved (Figure 3.20a). XPS peak of Pd 3d are retained, meaning its excellent stability (Figure 3.20b). Notably, the Pd NPs still display a good dispersity on the OB-C-N1 (Figure 3.20c-f).

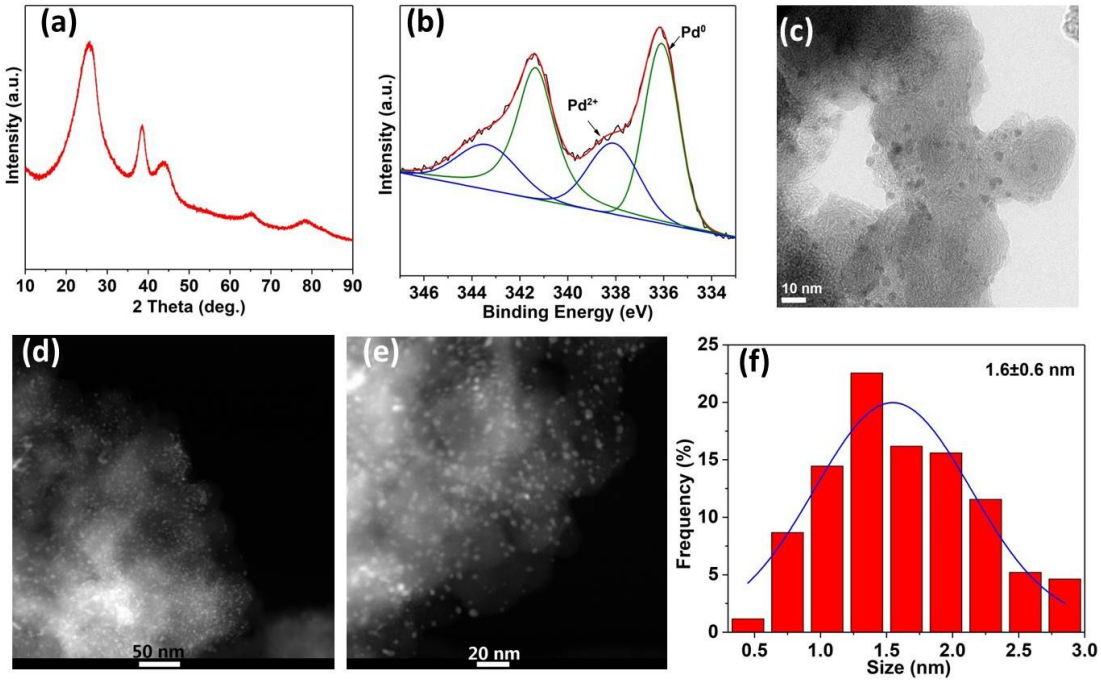

Figure 3.20 (a) XRD pattern, (b) Pd 3d XPS spectrum, (c) TEM and (d-e) HAADF-STEM images, and (f) corresponding Pd particle size distribution of the recycled Pd/OB-C-N1 catalyst.

The greatly enhanced catalytic activity of Pd/OB-C-N1 thanks to a high level of B-O and N doping and the small Pd particle size. During the decomposition of melamine and boric acid in the heating progress, the decomposition products and XC-72R interact with each other, leading to the functionalized carbon nanosphere surface with sufficient and robust B-O and N species. The B-O species have abilities to capture $PdCl_4^{2-}$

precursors during the synthetic process and strengthen the interaction between the support and Pd NPs. Meanwhile, N dopants provide more basic sites, facilitating the deprotonation of FA.[7d] As for the catalytic mechanism, FA firstly undergoes the O-H bond cleavage to produce a proton H^+ and Pd-formate intermediate. Subsequently, the Pd-formate go through the dissociation of C-H bond to yield CO_2 gas and a Pd-hydride species. Then, the H^+ reacts with H^- in Pd-hydride to generate H_2.[21]

3.4 Conclusion

In summary, we have successfully synthesized B-O-functionalized carbon nanospheres (OB-C1) by a facile one-step coanneling method with boric acid as a B source. Highly uniform Pd NPs supported on OB-C1 have been readily obtained through a traditional wet chemical impregnation and reduction method. We conclude that the B-O species have a strong interaction with the Pd NPs and are favorable to anchor Pd with a good dispersity and small sizes, providing a significantly improved activity over Pd/OB-C1 for FA dehydrogenation. Surprisingly, much amounts of the B-O species were incorporated into the carbon framework by adding melamine into the precursor mixture of XC-72R and boric acid, providing the highly B-O-functionalized carbon nanospheres (OB-C-N1). Given the ultrafine Pd particle size (~ 1.4 nm) and extensive B-O and N functionalities, the resultant Pd/OB-C-N1 demonstrates remarkable catalytic activity with 100% selectivity of H_2 towards CO-free generation for FA dehydrogenation. Notably, it also reveals excellent cycling stability during the FA decomposition. The current work promotes further exploration for precise design of novel nanocatalysts with carbon supports effectively functionalized by boron within the carbon framework, which are promising to be ideal candidates for practical application in fuel cells.

References

[1] a) L. Schlapbach, A. Züttel, *Nature* **2001,** *414*, 353-358; b) C. W. Hamilton, R. T. Baker, A. Staubitz, I. Manners, *Chem. Soc. Rev.* **2009,** *38*, 279-293; c) Q. L. Zhu, Q. Xu, *Energy Environ. Sci.* **2015,** *8*, 478-512; d) H. J. Yin, H. J. Tang, D. Wang, Y. Gao, Z. Y. Tang, *ACS Nano* **2012,** *6*, 8288-8297.

[2] a) X. C. Yang, J. K. Sun, M. Kitta, H. Pang, Q. Xu, *Nat. Catal.* **2018,** *1*, 214-220; b) Q. L. Zhu, Q. Xu, *Chem* **2016,** *1*, 220-245; c) M. Yadav, Q. Xu, *Energy Environ. Sci.* **2012,** *5*, 9698-9725; d) M. Yadav, A. K. Singh, N. Tsumori, Q. Xu, *J. Mater. Chem.* **2012,** *22*, 19146-19150; e) C. Tan, X. Huang, H. Zhang, *Materials Today* **2013,** *16*, 29-36.

[3] a) D. Mellmann, P. Sponholz, H. Junge, M. Beller, *Chem. Soc. Rev.* **2016,** *45*, 3954-3988; b) A. Boddien, D. Mellmann, F. Gärtner, R. Jackstell, H. Junge, P. J. Dyson, G. Laurenczy, R. Ludwig, M. Beller, *Science* **2011,** *333*, 1733-1736; c) J. F. Hull, Y. Himeda, W. H. Wang, B. Hashiguchi, R. Periana, D. J. Szalda, J. T. Muckerman, E. Fujita, *Nat. Chem.* **2012,** *4*, 383-388; d) C. Fellay, P. J. Dyson, G. Laurenczy, *Angew. Chem., Int. Ed.* **2008,** *47*, 3966-3968; e) Y. Chen, Q. L. Zhu, N. Tsumori, Q. Xu, *J. Am. Chem. Soc.* **2015,** *137*, 106-109.

[4] a) Z. P. Li, Q. Xu, *Acc. Chem. Res.* **2017,** *50*, 1449-1458; b) K. Sordakis, C. Tang, L. K. Vogt, H. Junge, P. J. Dyson, M. Beller, G. Laurenczy, *Chem. Rev.* **2017,** *118*, 372-433.

[5] a) F. Z. Song, Q. L. Zhu, X. C. Yang, W. W. Zhan, P. Pachfule, N. Tsumori, Q. Xu, *Adv. Energy Mater.* **2018,** *8*, 1701416; b) N. Wang, Q. M. Sun, R. S. Bai, X. Li, G. Q. Guo, J. H. Yu, *J. Am. Chem. Soc.* **2016,** *138*, 7484-7487; c) X. C. Yang, P.

Pachfule, Y. Chen, N. Tsumori, Q. Xu, *Chem. Commun.* **2016,** *52*, 4171-4174; d) Q. L. Zhu, N. Tsumori, Q. Xu, *J. Am. Chem. Soc.* **2015,** *137*, 11743-11748.

[6] a) D. Li, H. Q. Xu, L. Jiao, H. L. Jiang, *EnergyChem* **2019**, 100005; b) F. Z. Song, Q. L. Zhu, N. Tsumori, Q. Xu, *ACS Catal.* **2015,** *5*, 5141-5144; c) Y. Chen, X. Li, K. Park, L. Zhou, H. Huang, Y. W. Mai, J. B. Goodenough, *Angew. Chem., Int. Ed.* **2016,** *55*, 15831-15834; d) W. Chaikittisilp, K. Ariga, Y. Yamauchi, *J. Mater. Chem. A* **2013,** *1*, 14-19.

[7] a) X. Zhao, H. Yang, P. Jing, W. Shi, G. Yang, P. Cheng, *Small* **2017,** *13*, 1603279; b) L. He, F. Weniger, H. Neumann, M. Beller, *Angew. Chem., Int. Ed.* **2016,** *55*, 12582-12594; c) Q. J. Wang, N. Tsumori, M. Kitta, Q. Xu, *ACS Catal.* **2018,** *8*, 12041-12045; d) Z. P. Li, X. C. Yang, N. Tsumori, Z. Liu, Y. Himeda, T. Autrey, Q. Xu, *ACS Catal.* **2017,** *7*, 2720-2724; e) Y. Zheng, Y. Jiao, L. Ge, M. Jaroniec, S. Z. Qiao, *Angew. Chem., Int. Ed.* **2013,** *52*, 3110-3116; f) X. Wang, G. Sun, P. Routh, D. H. Kim, W. Huang, P. Chen, *Chem. Soc. Rev.* **2014,** *43*, 7067-7098; g) Y. Z. Chen, G. Cai, Y. Wang, Q. Xu, S. H. Yu, H. L. Jiang, *Green Chem.* **2016,** *18*, 1212-1217.

[8] Q. L. Zhu, N. Tsumori, Q. Xu, *Chem. Sci.* **2014,** *5*, 195-199.

[9] Z. Zhang, J. Xi, H. Zhou, X. Qiu, *Electrochim. Acta* **2016,** *218*, 15-23.

[10] a) Y. Zhao, L. Yang, S. Chen, X. Wang, Y. Ma, Q. Wu, Y. Jiang, W. Qian, Z. Hu, *J. Am. Chem. Soc.* **2013,** *135*, 1201-1204; b) X. Du, C. Du, P. Cai, W. Luo, G. Cheng, *ChemCatChem* **2016,** *8*, 1410-1416.

[11] a) Y. Zhang, H. Zhang, Y. Zhao, X. Han, H. Wang, Y. Gao, *Appl. Surf. Sci.* **2018,** *457*, 439-448; b) S. Chowdhury, Y. Jiang, S. Muthukaruppan, R. Balasubramanian,

Carbon **2018,** *128*, 237-248; c) S. Aghili, M. Panjepour, M. Meratian, *J. Therm. Anal. Calorim.* **2018,** *131*, 2443-2455.

[12] X. Liu, Y. Wang, L. Chen, P. Chen, S. Jia, Y. Zhang, S. Zhou, J. Zang, *ACS Appl. Mater. Interfaces* **2018,** *10*, 37067-37078.

[13] a) R. Goyal, B. Sarkar, A. Bag, F. Lefebvre, S. Sameer, C. Pendem, A. Bordoloi, *J. Mater. Chem. A* **2016,** *4*, 18559-18569; b) X. A. Zhao, C. Ong, Y. Tsang, Y. Wong, P. Chan, C. Choy, *Appl. Phys. Lett.* **1995,** *66*, 2652-2654.

[14] J. Romanos, M. Beckner, D. Stalla, A. Tekeei, G. Suppes, S. Jalisatgi, M. Lee, F. Hawthorne, J. Robertson, L. Firlej, *Carbon* **2013,** *54*, 208-214.

[15] S. Shin, J. Jang, S. H. Yoon, I. Mochida, *Carbon* **1997,** *35*, 1739-1743.

[16] H. G. Huang, C. L. Xiang, Y. S. Ning, J. Y. Huang, S. G. Ang, G. Q. Xu, *J. Phys. Chem. B* **2005,** *109*, 19296-19300.

[17] P. Pachfule, D. Shinde, M. Majumder, Q. Xu, *Nat. Chem.* **2016,** *8*, 718-724.

[18] D. W. Wang, F. Li, Z. G. Chen, G. Q. Lu, H. M. Cheng, *Chem. Mater.* **2008,** *20*, 7195-7200.

[19] K. Jiang, K. Xu, S. Zou, W. B. Cai, *J. Am. Chem. Soc*. **2014**, *136*, 4861-4864.

[20] Q. Y. Bi, J. D. Lin, Y. M. Liu, H. Y. He, F. Q. Huang, Y. Cao, *Angew. Chem. Int. Ed*. **2016**, *55*, 11849-11853.

[21] S. Zhong, Q. Xu, *Bull. Chem. Soc. Jpn.* **2018,** *91*, 1606-1617.

Chapter 4

Immobilizing Ultrafine Palladium Nanoparticles on Fe_3C/Fe- and N-functionalized Porous Carbon towards Fast Hydrogen Generation from Formic Acid

A Fe_3C/Fe- and N-functionalized porous carbon with a micro-/mesoporous porosity was synthesized. This distinct carbon (Fe_3C-Fe@NC) was used as a support to immobilize palladium nanoparticles (Pd NPs) (~ 1.4 nm) using a wet chemical reduction method. The Pd/Fe_3C-Fe@NC catalyst exhibits a superb activity for formic acid (FA) dehydrogenation, providing a rather high turnover frequency (TOF) of 7361 h^{-1} at 323 K, attributed to the ultrafine Pd NPs and the effects from Fe_3C/Fe and N in the support.

4.1 Introduction

Hydrogen, as a clean and renewable energy carrier, has attracted great attention in recent years.[1] In this respect, formic acid (FA) has been considered as the prospective chemical hydrogen storage material for hydrogen-powered fuel cells, owing to its excellent features including high hydrogen content (4.4 wt%), good stability, easy transportation, and low toxicity.[2] Numerous investigations have revealed that palladium (Pd)-based metal nanoparticles (NPs) possess outstanding catalytic performance in the dehydrogenation of FA to CO-free hydrogen even under ambient conditions ($HCOOH \rightarrow H_2 + CO_2$).[3] However, metal NPs are easy to aggregate, due to the high surface energy, which usually causes the loss in catalytic activity.[4] Many kinds of solid

materials, including silicon,[5] zeolite,[6] activated carbons,[7] graphene,[8] metal-organic frameworks (MOFs),[9] have been explored as supports to immobilize ultrafine Pd NPs, boosting their catalytic performance.[10]

Metal-organic framework (MOF)-derived porous carbons have recently been highlighted, owing to their tunable porosity, structural diversity, large surface area, and controllable components by varying the conditions of pyrolysis.[11] Nitrogen (N)-containing MOFs, as a sacrificial template, could provide in situ N-doped porous carbon. The N species not only anchor Pd NPs during the preparation and catalytic process, but also serve as alkaline active sites, facilitating the rate-determined step of FA deprotonation.[7a,12] Thus, MOF-derived N-doped porous carbon could be an appropriate support to stabilize Pd NPs for rapid hydrogen generation from FA.

Herein, for the first time, we develop a novel nanostructured Fe_3C/Fe- and N-doped carbon support (Fe_3C-Fe@NC) derived from calcining the mixture of ZIF-8 and sodium iron EDTA (EDTA-Na-Fe(III)). After treatment to remove impurities, the resultant Fe_3C-Fe@NC with micro- and mesoporous porosity and high contents of Fe and N was readily obtained, which was applied as the support to immobilize Pd NPs using a typical wet chemical reduction method. Interestingly, Fe-based nanocomposites exist in forms of metallic Fe and Fe_3C that are tightly wrapped in the N-doped carbon layers. Besides, Fe atoms form either Fe-N_x configurations or iron-based aggregations. The supported Pd NPs (Pd/Fe_3C-Fe@NC) with an average particle size of 1.4 nm demonstrate much high turnover frequency (TOF) values of 7361 and 11 778 h^{-1} at 323 and 333 K, respectively, for hydrogen generation from the aqueous FA/sodium formate (SF) solution.

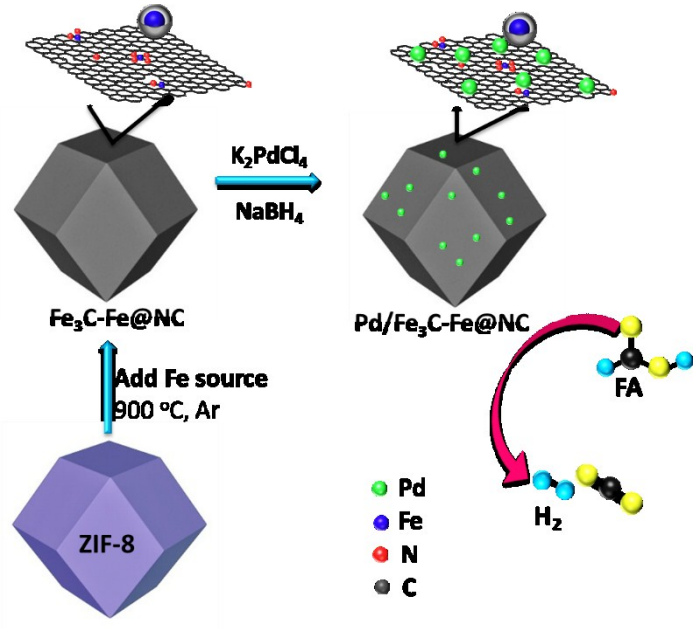

Figure 4.1 Schematic illustration of the preparation of Pd NPs immobilized on Fe_3C-Fe@NC support.

The synthesis of Fe_3C-Fe@NC-supported Pd nanocatalyst is shown in Figure 4.1. Nanostructured Fe_3C-Fe@NC with hierarchical pores was synthesized by a facile co-carbonization of a mixture of ZIF-8 and NaFe(III)EDTA at 900 ^oC for 2 hours in an argon flow, followed by acid and alkali treatment to remove the impurities. In addition, the control samples, Fe_3C-Fe@NC-x (x =1, 2, or 3) and Fe_3C-Fe@NC-2-*T* (*T* = 800, 900, or 1000^o) were prepared by altering iron source amounts and pyrolysis temperature, respectively. Finally, Fe_3C-Fe@NC was then utilized as the support to immobilize the Pd NPs through a representative wet chemical reduction procedure using $NaBH_4$ as a reducing agent, designated as Pd/Fe_3C-Fe@NC. For comparison, singly N-doped porous carbon (NC) with only micropores was also synthesized directly from the pyrolysis of ZIF-8 with no addition of Fe source, to which Pd NPs was immobilized using the same method (denoted as Pd/NC).

4.2 Experimental section

4.2.1 Materials

All chemicals were commercially available and used without further purification. Zinc nitrate hexahydrate ($Zn(NO_3)_2 \cdot 6H_2O$, Wako Pure Chemical Industries, 99%), 2-methylimidazole ($C_4H_6N_2$, Tokyo Chemical Industry Co., Ltd., > 98.0%), methanol (CH_4O, Kishida Chem. Co., 99.8%), ethylenediaminetetraacetic acid monosodium iron(Ⅲ) salt (EDTA-Na-Fe(Ⅲ), $C_{10}H_{12}N_2O_8NaFe$, Kishida Chem. Co.), hydrochloric acid (HCl, Wako Pure Chemical Industries, 37%), sodium hydroxide (NaOH, Wako Pure Chemical Industries, > 93%), formic acid (FA, HCOOH, Kishida Chem. Co., > 98%), sodium formate (SF, HCOONa, Kishida Chemical Co., > 98%), potassium tetrachloropalladate (K_2PdCl_4, Wako Pure Chemical Industries, > 97%), and sodium borohyride ($NaBH_4$, Tokyo Chemical Industry Co., Ltd., > 95%) were used as received. De-ionized (DI) water with a specific resistance of > 18.0 MΩ·cm was used in all experiments.

4.2.2 Characterization and instrumentation

The X-ray diffraction (XRD) measurements were executed on a Rigaku Ultima IV X-ray diffractometer with a Cu Kα source. X-ray photoelectron spectroscopic (XPS) measurements were conducted on a Shimadzu ESCA-3400 X-ray photoelectron spectrometer using a Mg Kα source. The N_2 sorption isotherms were measured using automatic volumetric adsorption instrument (BELSORP-max) at 77 K. The surface areas and the pore size distributions were calculated using Brunauer-Emmett-Teller (BET) method and the non-localized density functional theory (NLDFT) method, respectively. Raman scattering spectra were obtained from a laser Raman microscope

system (Nanophoton RAMANtouch) with an excitation wavelength of 532 nm. Elemental analyses were performed on Perkinelmer 2400II instruments. The Pd and Fe contents were obtained by inductively coupled plasma optical emission spectroscopy (ICP-OES) on the Varian Vista-MPX. Transmission electron microscopic (TEM) and high-annular dark-field scanning TEM (HAADF-STEM) pictures were recorded on TECNAI G^2 F20 with operating voltage at 200 kV and Titan3 G2 60-300 (FEI) machine under operating voltage of 300 kV. Element mapping images were obtained on a Titan3 G2 60-300 (FEI). The gas generated from the catalytic reaction was collected after purging the reactor with argon at least three times, which was tested by GC-8A (molecular sieve 5A, Ar as carrier gas) and GC-8A (Porapack N, He as carrier gas) analyzers (Shimadzu).

4.2.3 Syntheses of samples

1) Synthesis of ZIF-8

ZIF-8 was prepared using a reported facile process. $Zn(NO_3)_2 \cdot 6H_2O$ (4.41 g, 14.82 mmol) was dissolved in 300 mL of methanol at room temperature (rt). 2-methylimidazole (9.66 g, 117.66 mmol) was introduced into the above solution under stirring. The mixture was stirred for overnight at rt. The white precipitant was obtained by centrifuging and washed with methanol for three times. Finally, the product was dried at 60 ^oC to give ZIF-8.

2) Syntheses of Fe_3C-Fe@NCs and NC

Typically, 1.0 g of ZIF-8 and 0.2 g of EDTA-Na-Fe(Ⅲ) were mixed and ground in a mortar for several minutes until they were evenly mixed. The light yellow mixture was transferred to a ceramic crucible, heated in a tube furnace at 900 ^oC for 2 hours in an

argon flow, and then cooled down to rt. To remove the residual impurities on the surface, the raw product was firstly soaked in 100 mL of 2 M HCl solution for 24 hours, followed by water wash, and subsequently immersed in 100 mL of 2 M NaOH solution for 24 hours under stirring, followed by washing with plenty of DI water and drying at 60 ^{o}C. The resultant carbon product was denoted as Fe_3C-Fe@NC-2. By altering the iron source amount to 0.1 g and 0.4 g, respectively, Fe_3C-Fe@NC-1 and Fe_3C-Fe@NC-3 were synthesized using the same preparation process as that of Fe_3C-Fe@NC-2. Similarly, Fe_3C-Fe@NC-2-*T* samples were also fabricated at pyrolysis temperatures of *T* = 800 or 1000 ^{o}C.

For comparison, NC was prepared directly from the pyrolysis of ZIF-8 at 900 ^{o}C for 2 hours in an argon flow, followed by treatment with HCl solution.

3) Syntheses of Pd nanocatalysts

The above-mentioned carbons were utilized as the supports to immobilize the Pd NPs by a typical wet chemical reduction method. For example, 100 mg of Fe_3C-Fe@NC-2 was dispersed in 5 mL of DI water under stirring at rt. Subsequently, an aqueous solution of K_2PdCl_4 (0.1 M, 0.6 mL) was introduced and the mixture was continued to stir for 1 hour. 30 mg of fresh $NaBH_4$ solid dissolved in 1 mL of DI water was added into the above solution, followed by stirring for 3 hours. Finally, the resultant catalyst Pd/Fe_3C-Fe@NC-2 was centrifuged and washed with DI water for 3 times for further use.

4.2.4 Catalytic activity characterization

1) Procedure for hydrogen generation of formic acid (FA)

Reaction apparatus for testing the H_2/CO_2 evolution from the FA/sodium formate (SF) system is the same as the previous report. Generally, a mixture containing the as-prepared catalyst and DI water (~ 1.0 mL) was transferred into a two-necked round-bottom flask, which was placed in a water bath with a preset temperature at 30, 40, 50, and 60 ^{o}C. A gas burette filled with water was connected to the reaction flask to detect the volume of released gas with temperature kept at 298 K during the measurements. The reaction started when the FA/SF solution with various molar ratios (1 mL) was injected into the mixture. Through recording the displacement of water in the gas burette, the volume of the released gas was monitored. The molar ratios of metal Pd to FA were theoretically fixed at 0.02 for the catalytic reactions.

2) Durability test of Pd/Fe_3C-Fe@NC-2

To test the durability of the as-synthesized Pd/Fe_3C-Fe@NC-2, the catalyst was recollected by centrifugation after completing the decomposition of FA and washed with DI water for 3 times. For the next cycle, 1 mL of FA (3.0 M) and SF (7.5 M) was injected into the flask. Such cycling procedure for FA dehydrogenation was carried out for 5 runs at 50 ^{o}C.

3) Calculation methods

The turnover frequency (TOF) in this work is based on the metal amount (Pd atoms) in the catalyst, which is calculated from the equation as follow:

$$TOF = \frac{PV}{(RT) * 2n_{\mathrm{Pd}}t}$$

where P is the atmospheric pressure (101325 Pa), V is the final released gas volume of (H_2 + CO_2), R is the universal gas constant (8.3145 m^3 Pa mol^{-1} K^{-1}), T is the room temperature (298 K), n_{Pd} is the total mole number of Pd atoms in the catalyst, and t is

the completion time of the reaction in hour.

4.3 Results and discussion

4.3.1 Characterization

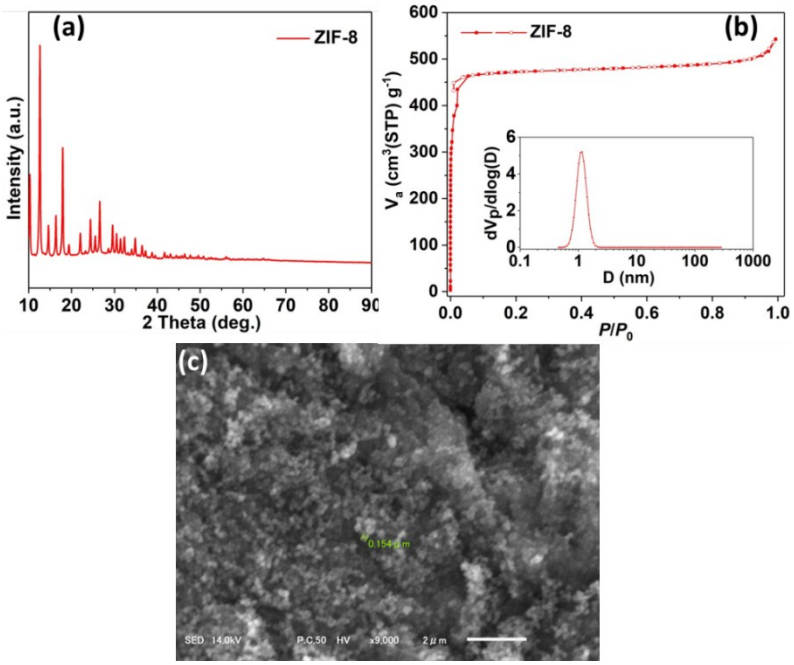

Figure 4.2 (a) XRD pattern, (b) N_2 sorption isotherm at 77 K and (c) SEM image of ZIF-8. Inset of (b) shows the corresponding pore size distribution of ZIF-8.

The X-ray diffraction (XRD) pattern (Figure 4.2a) indicates that ZIF-8 was successfully synthesized.[13] Nitrogen (N_2) sorption isotherm and corresponding pore size distribution (PSD) analysis (Figure 4.2b and inset) exhibit a high Brunauer-Emmett-Teller (BET) surface area of 1488 m^2 g^{-1} and the micropores less than 2 nm. The morphology of ZIF-8 shows nanoscale particles of ~ 154 nm (Figure 4.2c).

After pyrolysis, XRD pattern of NC (Figure 4.3) shows the typical broad peaks of carbons, while Fe_3C-Fe@NC-2 reveals the diffraction peaks of metallic Fe_3C and Fe, in good agreement with the data of Fe_3C (JCPDS No. 35-0772) and Fe (JCPDS No. 06-

0696).[14] Apparent peaks of Pd are observed at 2 theta ≈ 39.8 °, 46 °, and 66.5° (JCPDS No. 46-1043) over Pd/NC.[15] These peaks are not noticeable over Pd/Fe_3C-Fe@NC-2, demonstrating the formation of the small Pd NPs. The contents of Fe, Pd, and N in Pd/Fe_3C-Fe@NC-2 were further measured by inductively coupled plasma-optical emission spectroscopy (ICP-OES) and elemental analysis, which are 4.6, 6.4, and 2.41 wt%, respectively (Tables 4.1 and 4.2). Fe_3C-Fe@NC-2 and NC supports show N contents of 2.71 and 6.39 wt%, respectively.

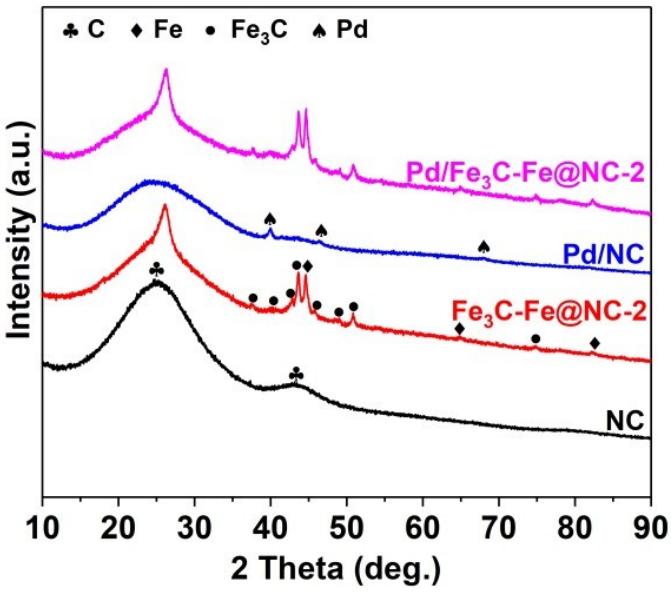

Figure 4.3 XRD patterns of NC, Fe_3C-Fe@NC-2, Pd/NC, and Pd/Fe_3C-Fe@NC-2.

Table 4.1 ICP analyses for the samples.

Sample	Fe content (wt%)	Pd content (wt%)
Pd/NC	-	5.3
Fe_3C-Fe@NC-2	5.1	-
Pd/Fe_3C-Fe@NC-2	4.6	6.4

Table 4.2 Elemental analyses for the samples.

Sample	N content (wt%)
NC	6.39
Fe_3C-Fe@NC-2	2.71
Pd/NC	5.90
Pd/Fe_3C-Fe@NC -2	2.41

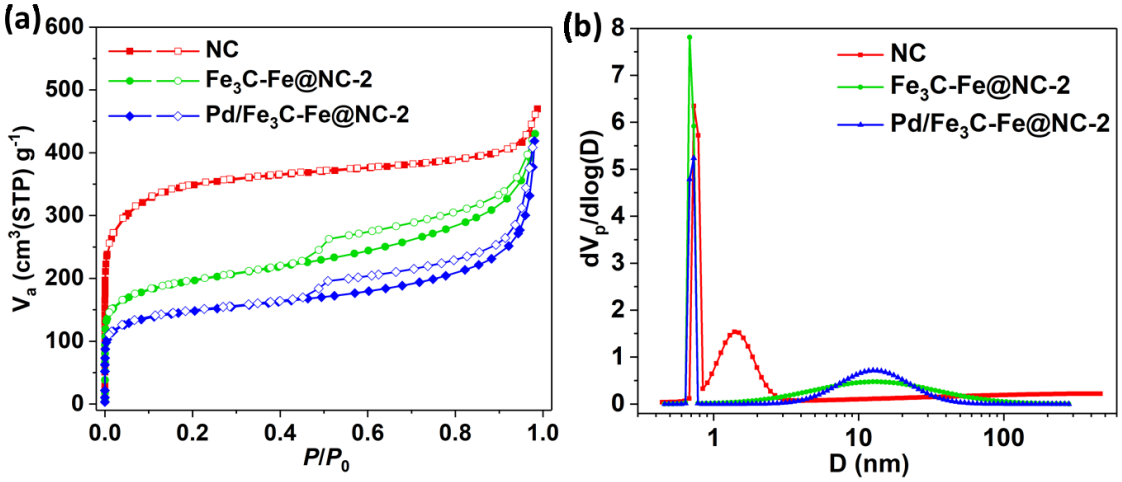

Figure 4.4 (a) N_2 sorption isotherms at 77 K and (b) the corresponding NLDFT pore size distributions over NC, Fe_3C-Fe@NC-2, and Pd/Fe_3C-Fe@NC-2.

According to N_2 sorption isotherms (Figure 4.4a), Fe_3C-Fe@NC-2 shows an obvious hysteresis loop, indicating the existence of mesopores. The calculated BET surface area is 684 m^2 g^{-1}, which is much lower than that of NC (1202 m^2 g^{-1}) (Table 4.3). PSD analysis (Figure 4.4b) confirms the hierarchically porous structure with micropores (~ 0.7 nm) and mesopores (2 ~ 50 nm) for Fe_3C-Fe@NC-2. NC only possesses micropores

(< 2nm), which preserves the pores of ZIF-8 precursor. The incorporation of Fe_3C-Fe in the N-doped carbon results in the pore reconstruction during the carbonization.

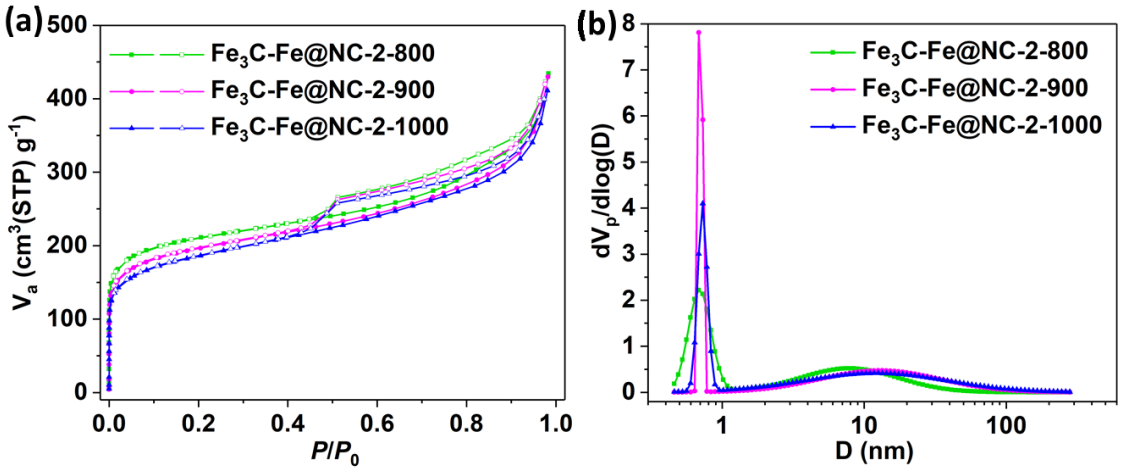

Figure 4.5 (a) N_2 sorption isotherms at 77 K and (b) the corresponding NLDFT pore size distributions over Fe_3C-Fe@NC-2-*T* (*T* = 800, 900, and 1000 ^oC).

Fe_3C-Fe@NC-2-800 and Fe_3C-Fe@NC-2-1000 also demonstrate the same pore size distribution as that of Fe_3C-Fe@NC-2, indicating the hierarchical micro-/mesopores (Figure 4.5). Compared with Fe_3C-Fe@NC-2, the Pd/Fe_3C-Fe@NC-2 catalyst shows a decreased BET surface area and pore volume, displaying that some Pd NPs are inside the pores of Fe_3C-Fe@NC-2.

Table 4.3 BET surface areas and pore volumes of the as-prepared samples.

Sample	S_{BET} (m^2 g^{-1})	Pore volume (cm^3 g^{-1})
ZIF-8	1488	0.832
NC	1202	0.727
Fe_3C-Fe@NC-2	684	0.665
Pd/Fe_3C-Fe@NC-2	515	0.647
Fe_3C-Fe@NC-2-800	731	0.672
Fe_3C-Fe@NC-2-1000	650	0.636

Transmission electron microscopy (TEM) and high-angle annular dark-field scanning TEM (HAADF-STEM) images of Pd/Fe_3C-Fe@NC-2 show that Pd NPs are uniformly dispersed on the Fe_3C-Fe@NC-2 support with an ultrafine Pd particle size of ~ 1.4 nm (Figure 4.6a and c). Large Fe-based particles (20 ~ 40 nm) are detected with some carbon nanotubes (CNTs) around them (Figure 4.6b). Elemental mapping images in Figure 4.6d-e display the homogeneous distribution of Pd, N, and C elements in Pd/Fe_3C-Fe@NC-2. However, Fe element displays two different distributions. In Figure 4.6d, Fe exhibits the exactly same distribution as that of N, probably attributed to Fe-N_x configuration at atomic level. Other parts of Fe aggregates and forms large particles, as shown in Figure 4.6e.[16] During the pyrolysis process, resultant Fe atoms after reduction by C are really active, which either reacts with N to produce Fe-N_x or catalyse C to form CNT/graphite carbon. Then, excessive Fe atoms would gather into large particles with CNT/thin carbon layers surrounding them.[14] The Pd/NC catalyst demonstrates Pd particle sizes of ~ 1.8 nm, where dodecahedron-like NC is clearly seen (Figure 4.7).

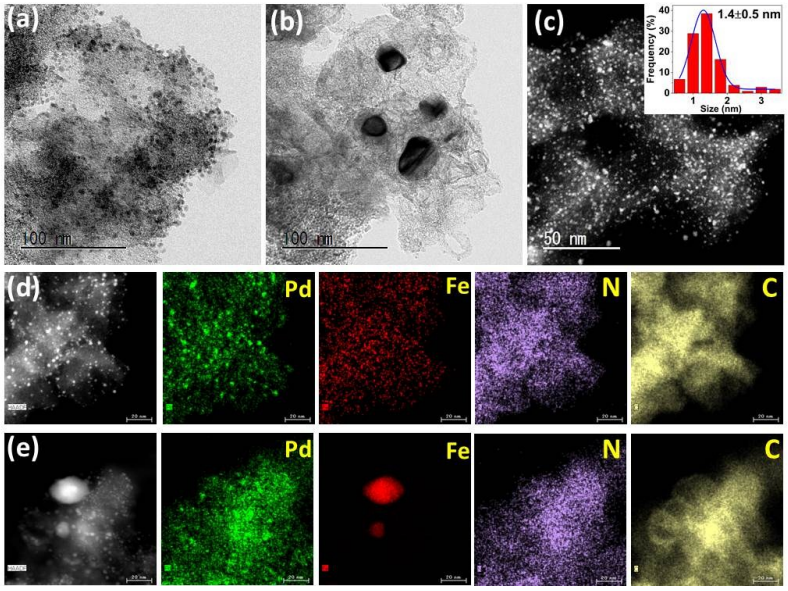

Figure 4.6 (a-b) TEM, (c) HAADF-STEM (inset: the corresponding Pd particle size distribution) and (d-e) elemental mapping images of Pd, Fe, N and C over as-prepared Pd/Fe_3C-Fe@NC-2. Scale bar in d-e is 20 nm.

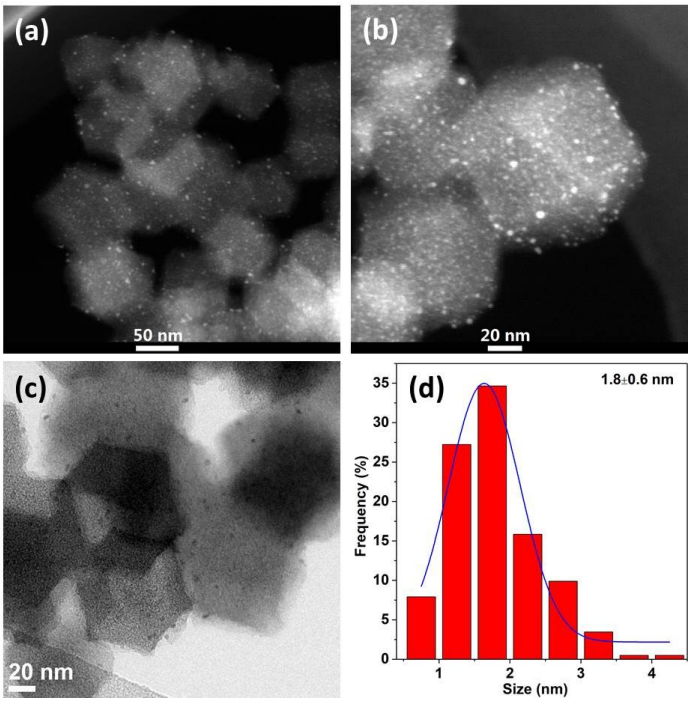

Figure 4.7 (a-b) HAADF-STEM and (c) TEM images, and (d) corresponding Pd particle size distribution of the as-prepared Pd/NC catalyst.

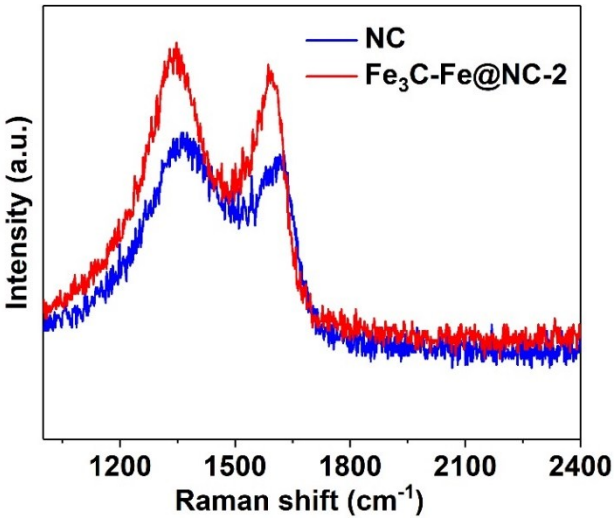

Figure 4.8 Raman spectra of NC and Fe_3C-Fe@NC-2 samples.

Raman spectrum (Figure 4.8) was used to investigate the graphitization degree by the ratio of D peak intensity (I_D) to G peak intensity (I_G).[17] Results show that Fe_3C-Fe@NC-2 and NC own the similar I_D/I_G values, corresponding to 1.05 and 1.08, respectively, meaning the coexistence of graphitic carbons and defected carbons. On one hand, introducing Fe_3C-Fe create many defects in the N-doped porous carbon framework. On the other hand, Fe-based particles catalyze the production of graphite carbon, in good agreement with the sharp peak of XRD patter for Fe_3C-Fe@NC-2 at 2 theta ≈ 26 ^oC.

X-ray photoelectron spectroscopy (XPS) was used to study the chemical states of elements for Pd/Fe_3C-Fe@NC-2. Pd 3d XPS spectrum (Figure 4.9a) shows typical doublet peaks, which are deconvoluted into four peaks, corresponding to metallic Pd^0 (341.2 and 335.9 eV) and Pd^{2+} (343.0 and 337.7 eV).[1c] The Pd^{2+} is possibly attributed to the oxidation on the surface of the catalyst when exposing in air. N 1s XPS spectrum (Figure 4.9b) is deconvoluted three typical peaks, including pyridinc-, pyrrolic-, and

graphitic N.[4b] No Fe 2p signal is observed on the catalyst surface, confirming the iron is encapsulated with carbon layers (Figure 4.9c).

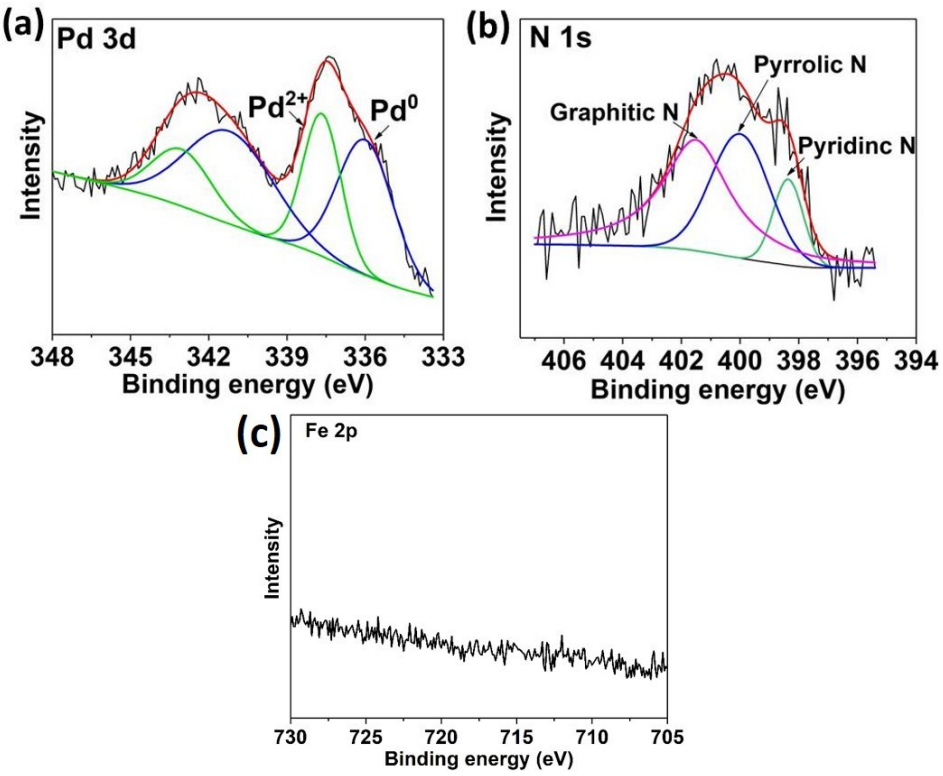

Figure 4.9 XPS spectra of (a) Pd 3d, (b) N 1s, and (c) Fe 2p of as-prepared Pd/Fe_3C-Fe@NC-2.

4.3.2 Catalytic activity

The as-synthesized Pd catalysts were applied for the hydrogen generation from the aqueous FA-SF solution. The Pd/Fe_3C-Fe@NC-2 catalyst exhibits the remarkable catalytic activity (Figure 4.10a), releasing the gas of 144 mL (H_2 + CO_2) within 0.4 min at 323 K (n_{FA}: n_{SF} = 1:2.5; n_{Pd}/n_{FA} = 0.02). The corresponding TOF value is as high as 7361 h^{-1} (Figure 4.10b), which is one of the most active heterogeneous catalysts ever so far under the similar condition (Table 4.4). The surplus gas volume over theoretical

value (144 mL) is owing to the decomposition of SF (Figure 4.11). The Pd/NC catalyst shows a much low rate for completing the reaction within 1.33 min at 323 K, corresponding to a TOF value of 2208 h^{-1} (n_{FA}: n_{SF} = 1:2.5; n_{Pd}/n_{FA} = 0.02).

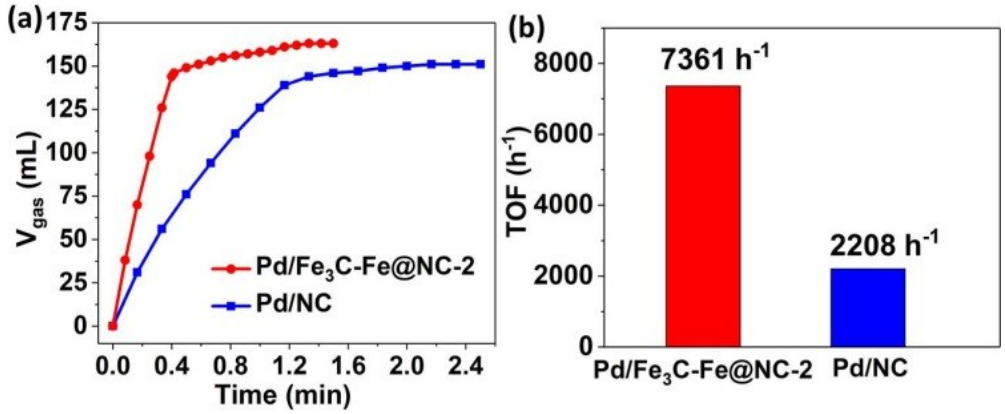

Figure 4.10 (a) Volume of the generated gas (H_2 + CO_2) *versus* time for the hydrogen generation from the aqueous FA-SF solution at 323 K (n_{FA}: n_{SF} = 1:2.5; FA, 3 mmol; n_{Pd}/n_{FA} = 0.02) and (b) the corresponding TOF values of the dehydrogenation of FA over the Pd/Fe$_3$C-Fe@NC-2 and Pd/NC catalysts.

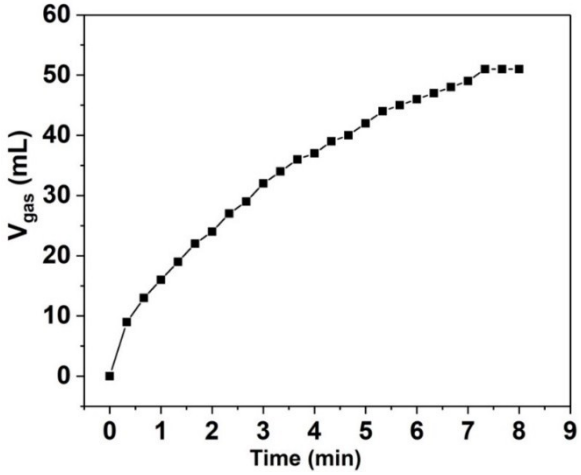

Figure 4.11 Volume of the generated gas *versus* time from aqueous SF solution (7.5 M, 1 mL) over the as-prepared Pd/Fe$_3$C-Fe@NC-2 catalyst at 323 K.

Table 4.4 Catalytic activities for dehydrogenation of FA catalyzed by different heterogeneous catalysts.

Catalyst	Temp. (K)	Additive	TOF (h^{-1})	Ea ($kJ \cdot mol^{-1}$)	Ref.
Pd/N-MSC-30-two-175	323	HCOONa	5890 [b]	43.7	7a
$(Co_6)Ag_{0.1}Pd_{0.9}$/rGO	323	HCOONa	2739 [b]	43.1	10a
Pd/C_m	323	HCOONa	4452 [a]	39.6	7b
Pd/MSC-30	323	HCOONa	2623 [b]	38.6	10e
$(Co_3)_E Au_{0.6}Pd_{0.4}$/rGO	323	HCOONa	4840 [b]	39.77	8b
Pd/PDA-rGO	323	HCOONa	3810 [b]	54.3	10f
Pd@CN900K	323	HCOONa	8000 [b]	46.9	4b
$Pd/CN_{0.25}$	298	None	5530 [c] 752 [a]	48.8	12e
$Pd_{0.6}Ag_{0.4}@ZrO_2$/C/rGO	323	HCOONa	2700 [a]	50.1	10g
in situ-Pd@MSC	333	HCOONa	9110 [a]	31.7	3c
Pd_1Au_1/72-LA	333	HCOONa	11 958 [b]	34.4	10h
Pd/FeNC-2	303	HCOONa	**2208**	47.3	**This**
	313		**4015**		**work**
	323		**7361**		
	333		**11 778**		

[a] Initial TOF values calculated on initial time for FA dehydrogenation on the basis of metal atoms.
[b] TOF values calculated on the complete time for FA dehydrogenation on the basis of metal atoms.
[c] Initial TOF values calculated on initial time for FA dehydrogenation on the basis of surface metal sites.

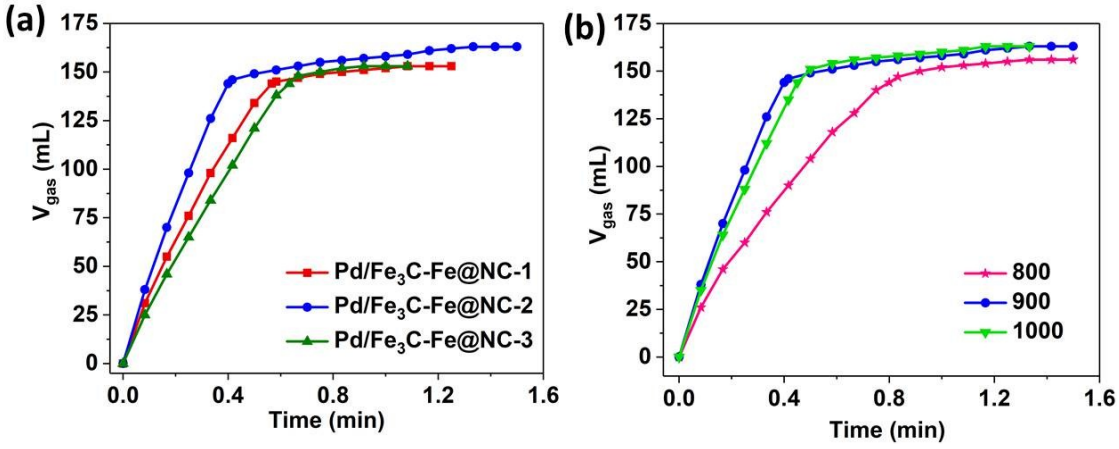

Figure 4.12 Volume of the generated gas (CO_2 + H_2) *versus* time for the hydrogen generation from the aqueous FA-SF solution (n_{FA}: n_{SF} = 1:2.5; FA, 3 mmol; n_{Pd}/n_{FA} = 0.02) at 323 K over (a) Pd/Fe_3C-Fe@NC-1, Pd/Fe_3C-Fe@NC-2, Pd/Fe_3C-Fe@NC-3, and (b) Pd/Fe_3C-Fe@NC-2-*T* (*T* = 800, 900, and 1000 ^oC, standing for the pyrolysis temperature).

Some comparative catalysts (Pd/Fe_3C-Fe@NC-1, -3, and Pd/Fe_3C-Fe@NC-2-800, -1000 ^oC) were prepared for FA dehydrogenation, indicating that Pd/Fe_3C-Fe@NC-2-900 is the most excellent catalyst (Figure 4.12).

Gas chromatography (GC) measurements confirmed the H_2 and CO_2 products in the released gas and no CO trace was found at the level of detection limit of 10 ppm (Figure 4.13 and 4.14), demonstrating 100% hydrogen selectivity, which is very important for the practical use in fuel cells.

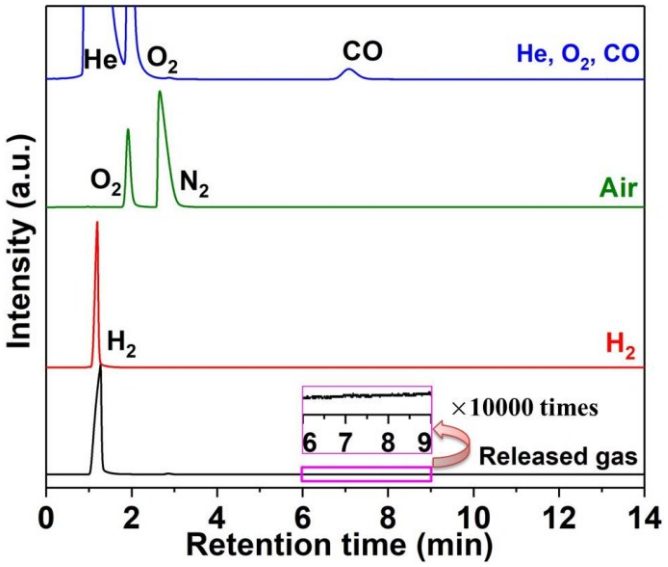

Figure 4.13 Gas chromatograms of CO, air and H_2 as reference gases and the released gas from FA decomposition over the as-prepared Pd/Fe_3C-Fe@NC-2 catalyst (n_{Pd}/n_{FA} = 0.02) at 323 K.

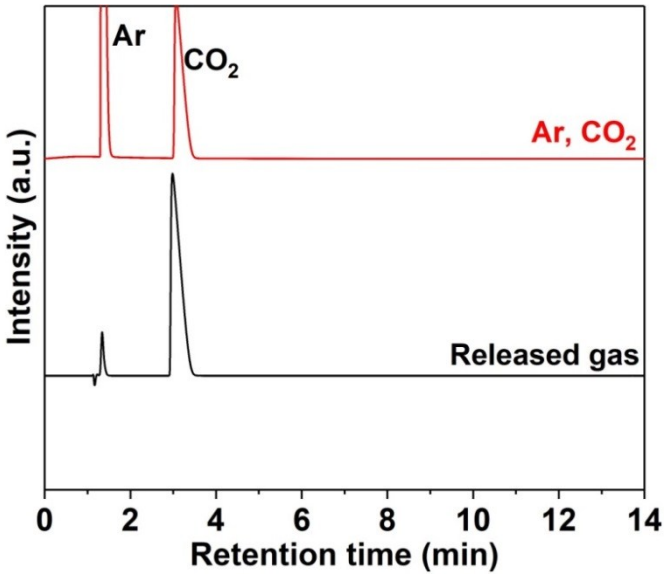

Figure 4.14 Gas chromatograms of CO_2 as reference gas and the released gas from FA decomposition over the as-prepared Pd/Fe_3C-Fe@NC-2 catalyst (n_{Pd}/n_{FA} = 0.02) at 323 K.

The time-dependent hydrogen generation at the reaction temperatures ranging from 303 to 333 K over Pd/Fe_3C-Fe@NC-2 in FA-SF system was carefully recorded (Figure 4.15a). At 303, 313, and 333 K, the hydrogen was completely generated within 1.33, 0.73, and 0.25 min, respectively, affording TOFs of 2208, 4015, and 11 778 h^{-1}. Based on the Arrhenius plot (Figure 4.15b), an activation energy (E_a) of 47.3 KJ mol^{-1} is obtained, comparable to other heterogeneous catalysts in similar conditions (Table 4.4). This suggests that Pd/Fe_3C-Fe@NC-2 is a highly active catalyst, which can convert FA into CO-free hydrogen even at room temperature.

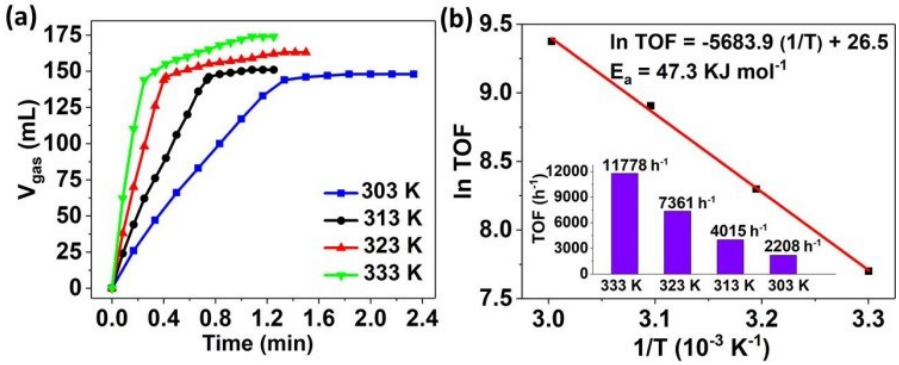

Figure 4.15 (a) Volume of the released gas (H_2 + CO_2) *versus* time for the hydrogen generation from the aqueous FA-SF solution at different temperatures over Pd/Fe_3C-Fe@NC-2 catalyst (n_{FA}:n_{SF} = 1:2.5; FA, 3 mmol; n_{Pd}/n_{FA}= 0.02) and (b) Arrhenius plot (ln TOF *vs.* 1/T) and TOF values (Inset of (b)) over Pd/Fe_3C-Fe@NC-2 catalyst.

Moreover, we also studied the effect of SF concentrations on the catalytic activity for FA dehydrogenation (Figure 4.16). We found that the activity was improved with rising the SF molar percentage in FA-SF system until it is up to 71.4%. Afterwards, further rising the molar percentage of SF had no apparent positive contribution to the activity.

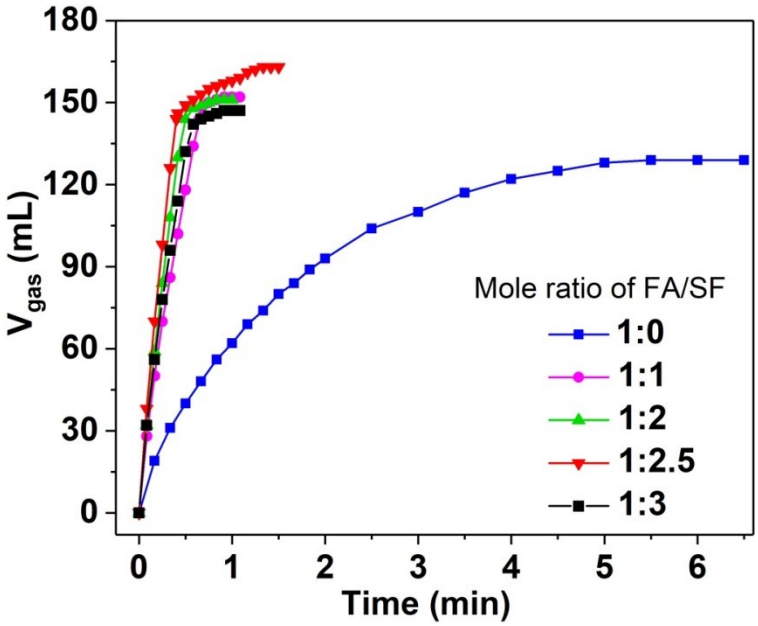

Figure 4.16 Volume of the generated gas (CO_2 + H_2) *versus* time for the hydrogen generation from the aqueous FA-SF solution with different FA/SF mole ratios over the as-prepared Pd/Fe_3C-Fe@NC-2 catalyst (FA = 3 mmol; n_{Pd}/n_{FA} = 0.02) at 323 K.

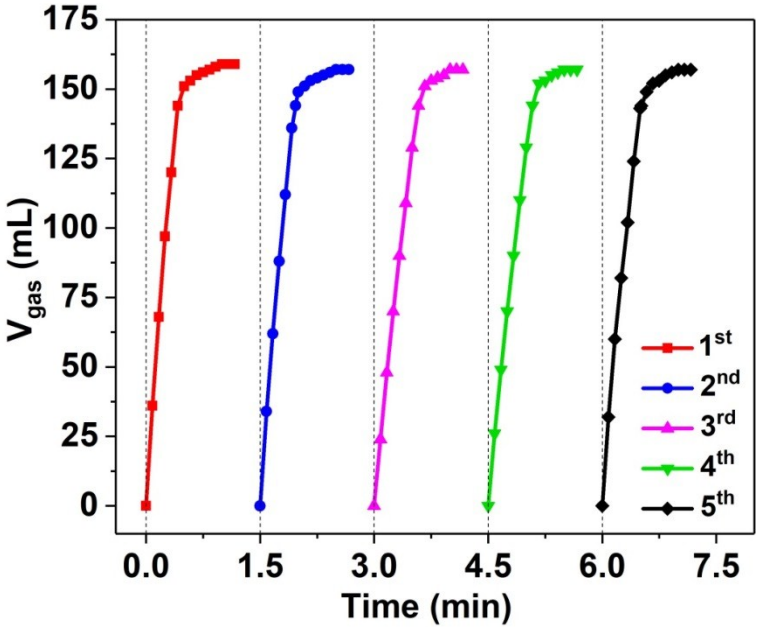

Figure 4.17 Durability test for the hydrogen generation from the aqueous FA-SF solution over the as-prepared Pd/Fe_3C-Fe@NC-2 catalyst at 323 K (n_{FA}: n_{SF} = 1:2.5; FA, 3 mmol per cycle; n_{Pd}/n_{FA} = 0.02).

Durability or recyclability of the catalyst is the key factor for practical application. After finishing the reaction of FA decomposition in each cycle, the Pd/Fe_3C-Fe@NC-2 catalyst was obtained by centrifuging and washed with water for 3 times. Results indicate that over 5 runs no obvious loss in catalytic activity was detected (Figure 4.17), illustrating the good durability of Pd/Fe_3C-Fe@NC-2. The catalyst after 5 cycles was investigated using a series of characterization.

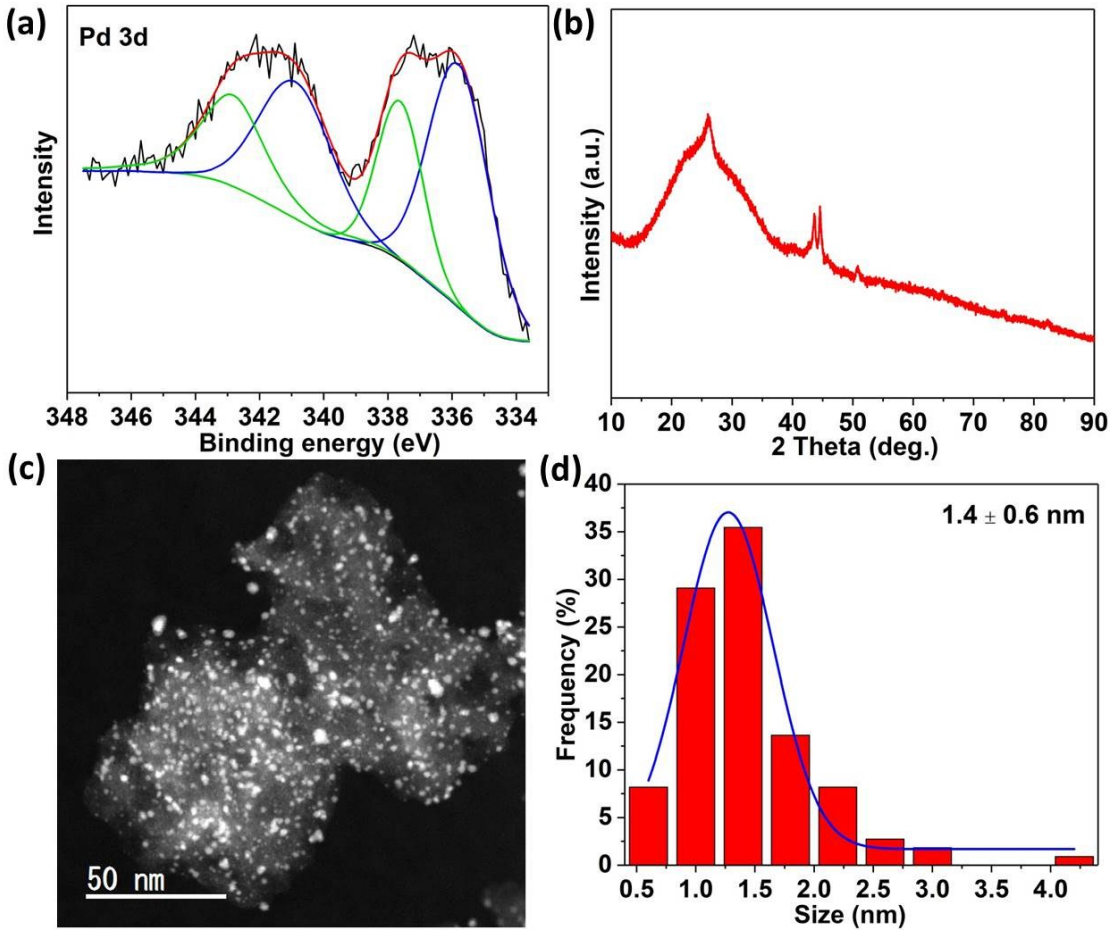

Figure 4.18 (a) Pd 3d XPS spectra, (b) XRD pattern, (c) HAADF-STEM image, and (d) corresponding Pd particle size distribution of recycled Pd/Fe_3C-Fe@NC-2 catalyst.

Pd 3d XPS spectrum is retained, indicating its excellent stability (Figure 4.18a). Notably, XRD pattern reveals the existence of Fe_3C-Fe in the recycled catalyst and the Pd peaks are still unclear (Figure 4.18b), further confirming that Fe_3C-Fe is robustly enfolded within carbon layers. ICP analysis shows that the Fe content in recycled Pd/Fe_3C-Fe@NC-2 is 4.6 wt%, which is the same as the as-prepared catalyst. Although Fe is easily eroded by FA, the capsulated Fe-based nanocomposites by carbon layer are indeed safe. Thus, the available defects in Fe_3C-Fe@NC-2 caused by Fe_3C-Fe doping could be efficiently taken advantage of. HAADF-STEM images exhibit that the Pd NPs uniformly disperse with the similar Pd particle size distribution as that of as-prepared catalyst before reaction (Figure 4.18c-d).

Briefly, the greatly enhanced activity of Pd/Fe_3C-Fe@NC-2 for FA dehydrogenation results from the ultrafine Pd particle size and the high level of Fe_3C-Fe and N doping. Fe_3C-Fe incorporation alters the porosity of N-doped porous carbons. Importantly, Fe-based particles are well protected by outer carbon layers, which is effectively isolated from FA. The defects and basic sites from Fe_3C-Fe and N dopants could control the in-situ growth of Pd NPs and strongly anchor Pd on the Fe_3C-Fe@NC-2 support during the preparation and catalytic reaction, leading to the small Pd particle sizes and uniform dispersion. Additionally, N species are favorable for promoting the deprotonation of FA, which is the key step of FA dehydrogenation.

4.4 Conclusion

In summary, a Fe_3C/Fe- and N-functionalized porous carbon with hierarchical porous structure was synthesized from the pyrolysis of a mixture of ZIF-8 and iron source, to which highly dispersed ultrafine Pd NPs (~ 1.4 nm) was successfully immobilized by a

wet reduction method. Fe-based particles (Fe_3C and Fe) are tightly enfolded by N-doped carbon layers. Thanks to the ultrafine Pd NPs and considerable defects and active sites caused by Fe_3C-Fe and N species in the Fe_3C-Fe@NC-2 support , the resultant Pd/Fe_3C-Fe@NC-2 catalyst completely catalyzed FA into CO-free hydrogen, affording a fairly high TOF value of 7361 h^{-1} at 323 K for FA decomposition in FA-SF system. Good durability of the catalyst is also observed, making it a promising catalyst for practical use. The Fe-based nanocomposites are still well preserved even after cycling without loss in content. This efficient and convenient functionalization approach of carbon supports will open a new window for the fabrication of ultrafine metal NP catalyst for hydrogen generation from hydrogen carriers.

References

[1] a) J. F. Hull, Y. Himeda, W. H. Wang, B. Hashiguchi, R. Periana, D. J. Szalda, J. T. Muckerman, E. Fujita, *Nat. Chem.* **2012**, *4*, 383; b) L. Schlapbach, A. Züttel, *Nature* **2001**, *414*, 353-358; c) Q. L. Zhu, Q. Xu, *Energy Environ. Sci.* **2015**, *8*, 478-512; d) X. Zhao, H. Yang, P. Jing, W. Shi, G. Yang, P. Cheng, *Small* **2017**, *13*, 1603279; e) T. He, P. Pachfule, H. Wu, Q. Xu, P. Chen, *Nat. Rev. Mater.* **2016**, *1*, 16059.

[2] a) D. Mellmann, P. Sponholz, H. Junge, M. Beller, *Chem. Soc. Rev.* **2016**, *45*, 3954-3988; b) A. Boddien, D. Mellmann, F. Gärtner, R. Jackstell, H. Junge, P. J. Dyson, G. Laurenczy, R. Ludwig, M. Beller, *Science* **2011**, *333*, 1733-1736; c) C. Fellay, P. J. Dyson, G. Laurenczy, *Angew. Chem., Int. Ed.* **2008**, *47*, 3966-3968; d) K. Sordakis, C. Tang, L. K. Vogt, H. Junge, P. J. Dyson, M. Beller, G. Laurenczy,

Chem. Rev. **2017**, *118*, 372-433; e) C. W. Hamilton, R. T. Baker, A. Staubitz, I. Manners, *Chem. Soc. Rev.* **2009**, *38*, 279-293.

[3] a) M. Navlani-García, D. Salinas-Torres, K. Mori, A. F. Léonard, Y. Kuwahara, N. Job, H. Yamashita, *Catal. Today*, **2019**, *324*, 90-96; b) Z. P. Li, Q. Xu, *Acc. Chem. Res.* **2017**, *50*, 1449-1458; c) Q. L. Zhu, F. Z. Song, Q. J. Wang, N. Tsumori, Y. Himeda, T. Autrey, Q. Xu, *J. Mater. Chem. A* **2018**, *6*, 5544-5549.

[4] a) W. Zhang, G. Lu, C. Cui, Y. Liu, S. Li, W. Yan, C. Xing, Y. R. Chi, Y. Yang, F. Huo, *Adv. Mater.* **2014**, *26*, 4056-4060; b) Q. J. Wang, N. Tsumori, M. Kitta, Q. Xu, *ACS Catal.* **2018**, *8*, 12041-12045.

[5] a) M. Yadav, A. K. Singh, N. Tsumori, Q. Xu, *J. Mater. Chem. A* **2012**, *22*, 19146-19150; b) X. Kang, H. Liu, M. Hou, X. Sun, H. Han, T. Jiang, Z. Zhang, B. Han, *Angew. Chem., Int. Ed.* **2016**, *55*, 1080-1084.

[6] N. Wang, Q. Sun, R. Bai, X. Li, G. Guo, J. Yu, *J. Am. Chem. Soc.* **2016**, *138*, 7484-7487.

[7] a) P. Z. Li, X. C. Yang, N. Tsumori, Z. Liu, Y. Himeda, T. Autrey, Q. Xu, *ACS Catal.* **2017**, *7*, 2720-2724; b) Q. L. Zhu, N. Tsumori, Q. Xu, *J. Am. Chem. Soc.* **2015**, *137*, 11743-11748.

[8] a) C. Tan, X. Huang, H. Zhang, *Mater. Today* **2013**, *16*, 29-36; b) X. Yang, P. Pachfule, Y. Chen, N. Tsumori, Q. Xu, *Chem. Comm.* **2016**, *52*, 4171-4174.

[9] Y. Z. Chen, Z. U. Wang, H. Wang, J. Lu, S. H. Yu, H. L. Jiang, *J. Am. Chem. Soc.* **2017**, *139*, 2035-2044.

[10] a) Y. Chen, Q. L. Zhu, N. Tsumori, Q. Xu, *J. Am. Chem. Soc.* **2015**, *137*, 106-109; b) X. C. Yang, J. K. Sun, M. Kitta, H. Pang, Q. Xu, *Nat. Catal.* **2018**, *1*, 214; c) H. Yin, H. Tang, D. Wang, Y. Gao, Z. Tang, *ACS Nano* **2012**, *6*, 8288-8297; d) Q. L.

Zhu, Q. Xu, *Chem* **2016**, *1*, 220-245; e) Q. L. Zhu, N. Tsumori, Q. Xu, *Chem. Sci.* **2014**, *5*, 195-199; f) F. Z. Song, Q. L. Zhu, N. Tsumori, Q. Xu, *ACS Catal.* **2015**, *5*, 5141-5144; g) F. Z. Song, Q. L. Zhu, X. C. Yang, W. W. Zhan, P. Pachfule, N. Tsumori, Q. Xu, *Adv. Energy Mater*. **2018**, *8*, 1701416; h) W. Hong, M. Kitta, N. Tsumori, Y. Himeda, T. Autrey, Q. Xu, *J. Mater. Chem. A* **2019**, *7*, 18835-18839

[11] a) L. L. Zou, C. C. Hou, Z. Liu, H. Pang, Q. Xu, *J. Am. Chem. Soc.* **2018**, *140*, 15393-15401; b) S. Dang, Q. L. Zhu, Q. Xu, *Nat. Rev. Mater.* **2017**, *3*, 1-14; c) H. L. Wang, Q. L. Zhu, R. Q. Zou, Q. Xu, *Chem* **2017**, *2*, 52-80; d) Z. Liang, R. Zhao, T. Qiu, R. Zou, Q. Xu, *EnergyChem* **2019**, 100001; e) D. Li, H. Q. Xu, L. Jiao, H. L. Jiang, *EnergyChem* **2019**, 100005; f) W. Chaikittisilp, K. Ariga, Y. Yamauchi, *J. Mater. Chem. A* **2013**, *1*, 14-19.

[12] a) S. Zhong, Q. Xu, *Bull. Chem. Soc. Jpn.* **2018**, *91*, 1606-1617; b) F. Wang, J. Xu, X. Shao, X. Su, Y. Huang, T. Zhang, *ChemSusChem* **2016**, *9*, 246-251; c) L. He, F. Weniger, H. Neumann, M. Beller, *Angew. Chem., Int. Ed.* **2016**, *55*, 12582-12594; d) Y. Z. Chen, G. Cai, Y. Wang, Q. Xu, S. H. Yu, H. L. Jiang, *Green Chem.* **2016**, *18*, 1212-1217; e) Q. Y. Bi, J. D. Lin, Y. M. Liu, H. Y. He, F. Q. Huang, Y. Cao, *Angew. Chem. Int. Ed*. **2016**, *55*, 11849-11853.

[13] S. Zhong, C. X. Zhan, D. P. Cao, *Carbon* **2015**, *85*, 51-59.

[14] W. J. Jiang, L. Gu, L. Li, Y. Zhang, X. Zhang, L. J. Zhang, J. Q. Wang, J. S. Hu, Z. Wei, L. J. Wan, *J. Am. Chem. Soc.* **2016**, *138*, 3570-3578.

[15] S. Zhong, N. Tsumori, M. Kitta, Q. Xu, *Nano Res.* **2019***,* 1-5.

[16] J. H. Kim, Y. J. Sa, S. H. Joo, *ACS Appl. Mater. Interfaces* **2017**, *9*, 9567-9575.

[17] P. Pachfule, D. Shinde, M. Majumder, Q. Xu, *Nat. Chem.* **2016**, *8*, 718.

Chapter 5

Conclusion

Functional carbon materials have been widely explored in energy-related areas, such as electrodes for supercapacitor and supports to immobilize metal NPs for hydrogen generation. The target of this dissertation is to synthesize the functional carbons with excellent features applied as excellent electrodes and supports to immoblize Pd NPs. Firstly, hierarchilly porous carbon with a high surface area was prepared derived from MOF/chitosan composites, which was used as electrodes in supercapacitor in sulfuric acid electrolyte. Secondly, boron-oxygen (B-O)- and N- functionalized carbon nanospheres was synthesized through coannealing the mixture of boric acid, melamine, and XC-72R, to which ultrafine Pd NPs was immoblized for efficient hydrogen generation from formic acid. Finally, Fe_3C/Fe- and N- decorated porous carbon with hierarchical micro-/mesopores was fabricated from pyrolysis of ZIF-8 and extra iron source, which was then used as support to immoblize ultrafine Pd NPs for rapid hydrogen generation from formic acid. The research outcomes in this dissertation are conclued as follows.

(i) Hierarchically Porous Carbons Derived from Metal-Organic Framework/Chitosan Composites for High-Performance Supercapacitors

We have developed a facile and general method to fabricate the hierarchically porous carbons (ranging from micro- to macropores) from the pyrolysis of MOF-5/chitosan composites at 900 ^{o}C for the first time, where chitosan is considered as pore structure-directing agent. With the optimization of conditions, the resultant carbon of NPC-2

exhibited the high specific surface area of 2375 m^2 g^{-1} and high pore volumes of 2.49 cm^3 g^{-1}, compared to the pristine carbon of NPC without the CS additive. As electrodes for EDLCs, hierarchically porous carbon NPC-2 demonstrated the best capacitive behaviour with a specific capacitance of 199.9 F g^{-1} in 1 M H_2SO_4 electrolyte, excellent rate capability of 75.6% from 0.05 A g^{-1} to 4 A g^{-1}, and superior cycling performance in a symmetric cell. We ascribed the excellent supercapacitor properties of NPC-2 to its high specific surface area, large pore volume, and hierarchical pore structures especially with abundant mesopores.

(ii) Immobilizing Palladium Nanoparticles on Boron-Oxygen-Functionalized Carbon Nanospheres towards Efficient Hydrogen Generation from Formic Acid

B-O-functionalized carbon nanospheres (OB-C1) were successfully synthesized by a facile one-step coanneling method with boric acid as a B source. Highly uniform Pd NPs supported on OB-C1 have been obtained through a traditional wet chemical impregnation and reduction method. B-O species have a strong interaction with the Pd NPs and are favorable to anchor Pd with a good dispersity and small sizes, providing a significantly improved activity over Pd/OB-C1 for FA dehydrogenation. Surprisingly, much amounts of the B-O species were incorporated into the carbon framework by adding melamine into the precursor mixture of XC-72R and boric acid, providing the highly B-O-functionalized carbon nanospheres (OB-C-N1). Given the ultrafine Pd particle size (~ 1.4 nm) and extensive B-O and N functionalities, the resultant Pd/OB-C-N1 demonstrates remarkable catalytic activity with 100% selectivity of H_2 towards CO-free generation for FA dehydrogenation. Notably, it also reveals excellent cycling stability during the FA decomposition. The current work promotes further exploration for precise design of novel nanocatalysts with carbon supports effectively functionalized

by boron within the carbon framework, which are promising to be ideal candidates for practical application in fuel cells.

(iii) Immobilizing Ultrafine Palladium Nanoparticles on Fe_3C/Fe- and N-functionalized Porous Carbon towards Fast Hydrogen Generation from Formic Acid

a Fe_3C/Fe- and N-functionalized porous carbon with hierarchical porous structure was synthesized from the pyrolysis of a mixture of ZIF-8 and iron source, to which highly dispersed ultrafine Pd NPs (~ 1.4 nm) was successfully immobilized by a wet reduction method. Fe-based particles (Fe_3C and Fe) are tightly enfolded by N-doped carbon layers. Thanks to the ultrafine Pd NPs and considerable defects and active sites caused by Fe_3C-Fe and N species in the Fe_3C-Fe@NC-2 support , the resultant Pd/Fe_3C-Fe@NC-2 catalyst completely catalyzed FA into CO-free hydrogen, affording a fairly high TOF value of 7361 h^{-1} at 323 K for FA decomposition in FA-SF system. Good durability of the catalyst is also observed, making it a promising catalyst for practical use. The Fe-based nanocomposites are still well preserved even after cycling without loss in content. This efficient and convenient functionalization approach of carbon supports will open a new window for the fabrication of ultrafine metal NP catalyst for hydrogen generation from hydrogen carriers.

In summary, this dissertation mainly focuses on the preparation of functional carbon materials as supercapacitor electrodes and supports for Pd NPs for hydrogen generation from formic acid. We hope that the functionalization strategies of carbon materials described in this dissertation could encourage more researchers to explore more potential carbon-based candidates in the practical applications of energy storage and catalysis.

List of publications

Journal Publications

1. Metal Nanoparticle-Catalyzed Hydrogen Generation from Liquid Chemical Hydrides

   Shan Zhong, and Qiang Xu*

   Bulletin of the Chemical Society of Japan, **2018**, 91, 1606-1617.

2. Hierarchically Porous Carbons Derived from Metal-Organic Framework/Chitosan Composites for High-Performance Supercapacitors

   Shan Zhong, Mitsunori Kitta, and Qiang Xu*

   Chemistry - An Asian Journal, **2019**, 14, 3583-3589.

3. Immobilizing Palladium Nanoparticles on Boron-Oxygen-Functionalized Carbon Nanospheres towards Efficient Hydrogen Generation from Formic Acid

   Shan Zhong, Nobuko Tsumori, Mitsunori Kitta, and Qiang Xu*

   Nano Research, **2019**, 12, 2966-2970.

4. Immobilizing Ultrafine Palladium Nanoparticles on Fe_3C/Fe- and N-functionalized Porous Carbon towards Fast Hydrogen Generation from Formic Acid

   Shan Zhong, Xinchun Yang, Nobuko Tsumori, Noboru Taguchi, and Qiang Xu*

   In preparation.

Doctor Thesis, Kobe University
“Study of Functional Carbon Materials for Energy Applications”, 103 pages
Submitted on January, 23, 2020
The date of publication is printed in cover of repository version published in Kobe University Repository Kernel.